Title
Computational Modeling of Cardiac Electromechanics

Author
Krishnamoorthi, Shankarjee

Publication Date
2013

Peer reviewed|Thesis/dissertation

University of California

Los Angeles

Computational Modeling of Cardiac Electromechanics

A dissertation submitted in partial satisfaction

of the requirements for the degree

Doctor of Philosophy in Mechanical Engineering

by

Shankarjee Krishnamoorthi

2013

Abstract of the Dissertation

Computational Modeling of Cardiac Electromechanics

by

Shankarjee Krishnamoorthi

Doctor of Philosophy in Mechanical Engineering

University of California, Los Angeles, 2013

Professor William S Klug, Chair

Cardiac arrhythmias are a leading cause of death worldwide. Notably, the electrophysiologiy and microstructural requirements for a fatal ventricular arrhythmia remain incompletely understood, thereby the treatment remains largely empirical. Standard antiarrhythmic drug therapy has failed to reduce, and in some instances has increased, the incidence of Sudden Cardiac Death (SCD). Hence, a more complete understanding of the mechanisms that foment a fatal arrhythmia is needed and computational models offer an excellent way to test hypotheses about various changes to cellular electrophysiology and myocardial microstructure in a manner not easily achieved in experiments. The understanding of associated deformation is also a longstanding research field; to some extent it provides the paradigm of a complex system, as it incorporates several mathematical issues such as geometric and material nonlinearity, complex geometrical and material data, fluid-structure interaction, that are already challenging by themselves without even mentioning the social relevance of the problem.

This thesis is concerned with the development of a unified formulation of cardiac electromechanics. The computational requirements for physiologically and numerically accurate computational analysis of the coupled equations of cardiac electrophysiology and finite-deformation contractile mechanics are carefully ex-

amined. The validation criterion which needs to be satisfied by any generic model are laid out.

The voltage evolution in the heart is obtained by solving the reaction diffusion monodomain equations. The convergence properties of finite-element procedures, employing various combinations of different shape functions, quadrature methods, and operator splitting strategies are studied which place the most stringent limitations on mesh resolution. Computational speedup is achieved preferential by row-sum lumping of the capacitance and mass matrices. However, selective lumping of these matrices can have noticeable effects on the convergence.

Finite element model of a rabbit ventricle is developed using Diffusion Tensor(DT) - MRI images. His-Bundle is included in the model to provide the correct activation sequence. Different geometries of the conduction system are analyzed comparing the obtained activation pattern and six lead electrocardiogram (ECG). The ventricular model is further validated by reproducing scroll wave break up.

Cardiac excitation coupling is modeled using an active deformation formulation based on Calcium dynamics. Analysis of the formulation of the active part of the deformation gradient and its dependence on Calcium concentration is studied. Effects of material models and inclusion of fiber anisotropy are also studied. Using a simplified ellipsoid model with assumed fiber orientation consistent with commonly used values in literature we successfully reproduce the twisting action and 60% volume reduction which is typically observed in experiments.

The dissertation of Shankarjee Krishnamoorthi is approved.

Christopher S Lynch

Jiun-Shyan (JS) Chen

Daniel B Ennis

Alan Garfinkel

William S Klug, Committee Chair

University of California, Los Angeles

2013

To my mother ...

who—among so many other things

sacrificed everything just for my happiness.

My wife ...

Thanks for everything.

Table of Contents

List of Figures

List of Tables

Acknowledgments

कर्मणयेवाधिकारस्ते मा फलेषु कदाचन।
मा कर्मफलहेतुर्भूर्मा ते सङ्गोऽस्त्वकर्मणि।

You have the right to perform your actions, but you are not entitled to the fruits of the actions. Do not let the fruit be the purpose of your actions, and therefore you wont be attached to not doing your duty. - Shri Bhagavad Gita (2.47)

A few years ago, I would have never thought that I could earn the highest attainable degree and write a thesis. For that, I would like to thank God for guiding me through all the adversities in my life.

On a different note, this work would not have been possible without the guidance and supervision of my advisor, Professor William Klug whom I met five years ago while working and started to work with four years, ago only to realize how lucky I was to be in such good hands. His constant support and encouragement have been not only been a source of inspiration but also a driving force in the course of this work.

I want to thank Professor Alan Garfinkel and Professor Daniel Ennis for introducing me to this fascinating world of cardiology and patiently teaching me the basics of cardiac electrophysiology. The weekly meetings were something I would always look forward to. I want to thanks Professor Christopher Lynch and Professor Jiun-Shyan (JS) Chen for agreeing to serve on my thesis committee.

Many people apart from my advisor have contributed to my advancement throughout my graduate studies. First and utmost Dr Luigi Perotti, thanks for all the discussions we had ranging from life to mechanics. His thoroughness in any subject and availability answer any question however trivial are remarkable. Secondly thanks to Mr Peter Borgstorm for all the help in cell modeling and physiology. I would also like to thank my former lab mates Dr Mainak Sarkar,

Dr Mo Bai, Dr Ankush Aggarwal and my current lab mate Mr Aditya Ponnaluri for all the good time spent at the lab. I will cherish our times at UCLA. Mo and Aditya, thanks to you two for all the fun at tennis courts, Roger style backhand and Rafa style forehand discussions.

I would like to thank my brother Mr Raghuraman who is always concerned more about me than himself and readily available with a laundry list of suggestions. I also thank my in-laws Mr Venkatramanan and Mrs Seethalakshmi who were very supportive of my decision to pursue this degree after getting married. Thanks for all the motivation.

My parents Mr Krishnamoorthi and Mrs Geetha without whom I will not be what I am right now. Looking back without my mother's care and attention, I would probably be still stuck in 5th grade trying to clear my exams. Finally my wonderful wife Harini without whom this would have still been a dream. She stood by me all along, supported and encouraged me, took responsibility on her shoulder when warranted but still managed to have a wonderful smile on her face all the time.

Vita

1996 – 2000	B.Tech (Mechanical Engineering), Indian Institute of Technology, Madras
2000 – 2002	M.S. (Mechanical Engineering). University of Illinois, Urbana-Champaign
2002 – 2008	Senior Project Engineer, Caterpillar Inc, Champaign, IL
2008 – 2010	Member Technical Staff, nanoPrecision Products, Camarillo, CA
2010 – present	Teaching fellow, Department of Mechanical and Aerospace Engineering, UCLA

CHAPTER 1

Introduction

Our knowledge about the heart dates back more than two millenia. Already in the days of Aristotle (350 BCE) the importance of the heart was recognized, and it was, in fact, considered to be the most important organ in the body. Other vital organs, such as the brain and lungs, were thought to exist merely to cool the blood. Over two thousand years later, the heart maintains its position as one of the most important, and also most studied, organs in the human body.

The primary function of the heart is to impart energy to blood in order to generate and sustain an arterial blood pressure necessary to provide adequate perfusion of organs. The heart achieves this by contracting its muscular walls around a closed chamber to generate sufficient pressure to propel blood from the cardiac chamber (e.g., left ventricle), through the aortic valve and into the aorta. Figure 1.1 shows the flow of blood in a regular heart. The pumping function of the heart is the result of a rhythmic cycle of contraction and relaxation of about 10^{10} muscle cells, a process that is controlled by a complex pattern of electrical activation. For a normal human being this complex rhythmic contraction cycle occurs approximately 2.5 billion times over the life span.

The heart is divided into four chambers. The chambers on the top are called the atrium and the bottom ones are called the ventricle. Further the atrium and ventricles are classified as right atrium, right ventricle, left atrium, and left ventricle. The right and left sides of the heart are separated by a muscular wall called the septum. This prevents blood without oxygen from mixing with blood

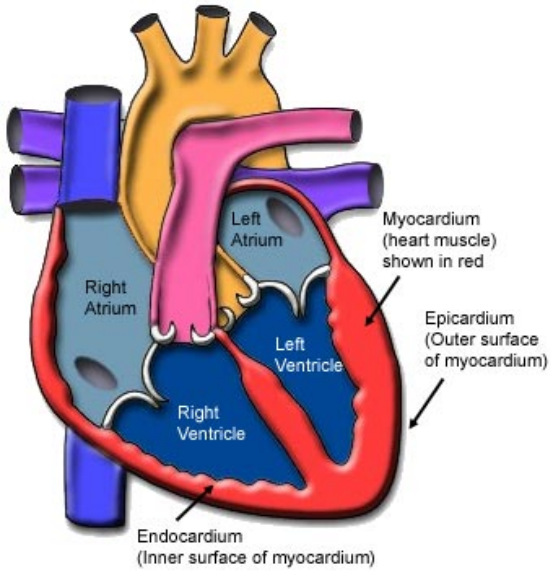

Figure 1.1: Cross sectional view of the heart. [Texas Heart Institute]

that has oxygen. The heart also has valves that separate the atrium and ventricle and connect to major blood vessels. Blood flows from the body into the right atrium. The blood on the right side of the heart has been used by the body and has little oxygen left in it (is deoxygenated or oxygen-poor). The oxygen-poor blood flows from the right atrium through the tricuspid valve to the right ventricle. From the right ventricle, blood is pumped through the pulmonary valve into the blood vessel that goes to the lungs. This blood then picks up oxygen. Oxygen-rich blood flows from the lungs through blood vessels back to the heart's left atrium. From the left atrium, blood goes through the mitral valve and into the left ventricle. The left ventricle pumps blood through the aortic valve to a major blood vessel called the aorta and out to the body. The blood delivers oxygen to the body, then returns through veins to the right atrium and repeats the blood flow cycle. Since the left ventricle pumps the blood to the entire human body it has the highest wall thickness compared to the other chambers.

1.1 Cardiac Electrical Conduction

For the heart to function normally there is a specialized tissue that produces and sends electrical impulses to the heart muscle. It is these impulses that essentially lead to the contraction of the heart. The heart's electrical conduction consists of three important components as shown in Figure 1.2

S-A node (sinoatrial node) known as the heart's natural pacemaker, the S-A node has special cells that create the electricity that makes the heart beat.

A-V node (atrioventricular node). The A-V node is the bridge between the atria and ventricles. Electrical signals pass from the atria down to the ventricles through the A-V node.

His-Purkinje system. The His-Purkinje system carries the electrical signals throughout the ventricles to make them contract. The parts of the His-Purkinje system include, His Bundle (the start of the system) , Right bundle branch, Left bundle branch and Purkinje fibers (the end of the system).

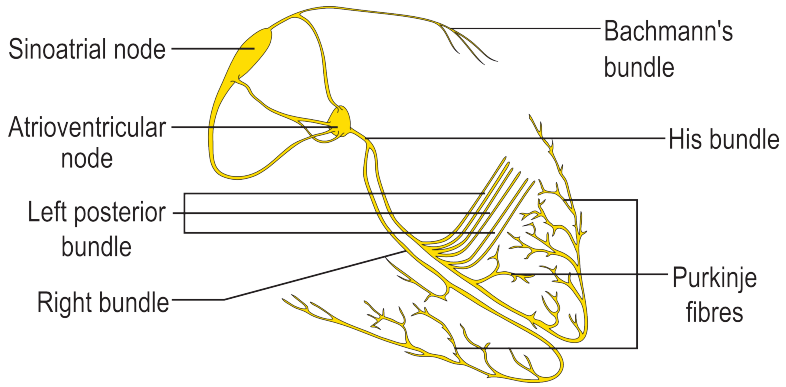

Figure 1.2: Schematic representation of entire conduction system in the heart. [www.wikipedia.org]

Initial electrical impulse is generated at the SA node which travels first to the atrium via the Bachmann's bundle. This causes electrical activation of the atrium

followed by the mechanical deformation. In the meanwhile the electrical stimulus reaches the AV node. The stimulus from the AV node travels to the ventricles through the His-Purkinje conduction system. This results in electrical activity in the ventricles which again is followed by the mechanical deformation. The ventricles and the atria are electrically insulated. Hence electrical activity from the atria does not propagate to the ventricle except through AV node. This conduction system plays a key role in ensuring normal heart function. The activation pattern of the tissue dictates the mechanical deformation. Hence a synchronous activation of the ventricle is quintessential in obtaining a synchronous deformation in the ventricular region.

1.2 Cardiac health issues

When the heart beats, the electrical impulses that cause it to contract follow a precise pathway through the heart. Any interruption in these impulses can cause an arrhythmia. Doctors typically classify arrhythmias not only by where they originate (atria or ventricles) but also by the speed of heart rate they cause: In the case of humans [www.mayoclinic.com],

1. Tachycardia: This refers to a fast heartbeat a resting heart rate greater than 100 beats a minute.

2. Bradycardia: This refers to a slow heartbeat a resting heart rate less than 60 beats a minute.

Further arrhythmia based on its location is further classified as,

Tachycardias in the atria:

1. Atrial fibrillation. This fast and chaotic beating of the atrial chambers is a common arrhythmia,

2. Atrial flutter. Atrial flutter is similar to atrial fibrillation. Both can occur, coming and going in an alternating fashion. The heartbeats in atrial flutter are more-organized and more-rhythmic electrical impulses than in atrial fibrillation.

3. Supraventricular tachycardia (SVT). SVT is a broad term that includes many forms of arrhythmia originating above the ventricles (supraventricular). SVTs usually cause a burst of rapid heartbeats that begins and ends suddenly and can last from seconds to hours. These bursts often start when the electrical impulse from a heartbeat begins to circle repeatedly through an extra pathway.

4. Wolff-Parkinson-White syndrome. People with this condition have an extra electrical pathway between the atria and the ventricles. This pathway may allow electrical signals to pass between the atria and the ventricles without passing through the atrioventricular node, leading to short circuits and rapid heartbeats.

Tachycardias in the ventricles:

1. Ventricular tachycardia (VT). This fast, regular beating of the heart is caused by abnormal electrical impulses that start in the ventricles. Often these are due to a problem with the electrical impulse traveling around a scar from a previous heart attack. VT can cause the ventricles to contract more than 200 beats a minute.

2. Ventricular fibrillation. In ventricular fibrillation, rapid, chaotic electrical impulses cause your ventricles to quiver uselessly instead of pumping blood. Without an effective heartbeat, the blood pressure plummets, cutting off blood supply to the vital organs including brain. Most people lose consciousness within seconds and require immediate medical assistance, including chest compressions, defibrillation and cardiopul-

monary resuscitation (CPR). Ventricular fibrillation is frequently triggered by a heart attack.

3. Long QT syndrome. Long QT syndrome (LQTS) is a heart disorder that carries an increased risk of fast, chaotic heartbeats. The rapid heartbeats, caused by changes in the electrical system of the heart, may lead to fainting, which can be life-threatening. In some cases, the heart's rhythm may be so erratic that it can cause sudden death.

Bradycardia a slow heartbeat:With a slow heart rate the heart isn't pumping enough blood and may be caused by one the of several bradycardias, including:

1. Sick sinus. The sinus node, which is responsible for setting the pace of your heart, isn't sending impulses properly, and hence the heart rate may be too slow, or it may speed up and slow down intermittently.

2. Conduction block. A block of your heart's electrical pathways can occur in or near the atrioventricular node, which lies on the pathway between atria and ventricles. A block can also occur along other pathways to each ventricle. Depending on the location and type of block, the impulses between the upper and lower halves of the heart may be slowed or blocked. If the signal is completely blocked, certain cells in the atrioventricular node or ventricles can make a steady, although usually slower, heartbeat. Some blocks may cause no signs or symptoms, and others may cause skipped beats or bradycardia.

Ventricular tachyarrhythmias (abnormal acceleration of ventricular rate) which potentially can lead to sudden cardiac death (SCD); are associated with common heart diseases (e.g. hypertrophic cardiomyopathy, idiopathic cardiomyopathy, ischemic cardiomyopathy, etc.) [ZW98] ; and account for 400,000 deaths per

year [ZCG01]. Treatment remains largely empirical, in part because of an incomplete understanding of the specific cellular and microstructural mechanisms that trigger the arrhythmia [Gil03]. Implantable cardioverter defibrillators (ICD) improve survival in high-risk patients, but have significant co-morbidities [YDZ05]. Antiarrhythmic drug therapy has largely failed to reduce, and in some instances has increased, the incidence of SCD [ELM91]. In fact, the greatest reduction in cardiovascular mortality (including SCD) in patients with clinically manifest heart disease has resulted from the use of beta blockers and non-antiarrhythmic drugs [RZ05]. Each year in the United States, more than 340,000 people learn that they have atrial fibrillation – the most common disorder of the heart's electrical system. They join legions of other Americans with similar types of arrhythmia. Left untreated, some types arrhythmia can cause fainting, shortness of breath, and even death. Heart failure is by far the most frequent cause of death, and the related financial and personal costs are huge.

An improved understanding of how the heart works can potentially lead to new techniques for the diagnosis and treatment of heart problems, and this serves as motivation for the enormous resources that are invested in heart-related research.

1.3 Open questions

Though there is classification of arrhythmia based on location and its behavior there is not a clear understanding of the physiological reasons which lead to this with the exception of Wolfff-Parkinson-White syndrome which clearly has an anatomical underlying factor. There is a need for understand the mechanisms that foment a fatal arrhythmia. Is arrhythmia due to (a) biochemical changes - changes in reactions in each cell (b) fiber orientation changes - change in preferred condition orientation at each cell, (c) Geometric changes or (d) is it a combination of few or all of them. A controlled environment where each of these parameters

can be varied to study its influence is of quint essential importance in understand arrhythmia.

Although the causes of heart failure (HF) may be ultimately traced to changes in signaling pathways and biochemical control factors, the only direct mechanism for HF is physical, namely a reduction in the ability of muscle contraction to pump blood. For example, researchers have shown [GAS07, SPB03, SWB05] that myocytes in heart failure exhibit changes in K currents and Ca^{2+} leak currents, which alter the action potential response and Ca transient, which in turn alter the timing and strength of contraction in failing heart tissue. While such effects are known, they are difficult to understand quantitatively in an experimental context because of the many other changes occurring simultaneously in HF, including stiffening due to tissue remodeling, wall dilation, hypertrophy, etc.

Modeling and simulation are the only way to isolate and assess the mechanisms systematically. They provide a "rational basis" for the design of therapies, as the search for causes of HF requires a mechanistic understanding of how the heart functions. Among the numerical methods employed to approximate the analytically intractable electrophysiology equations, the finite element method (FEM) [e.g., [LGT03, VRT09, BBP08]] has become commonly favored, primarily because it allows to capture the curved geometry of the heart in a straightforward way. Also, because FEM is the method of choice for solid mechanics, it has been noted that the framework provides a straightforward way to develop coupled simulations of electrophysiology and contractile mechanics of the heart [GK10].

1.4 Summary

The objective of this thesis is to develop and validate an unified computational framework which can be used to simulate typical physiological events and understand the effect of the contribution factors. A validated and verified numerical EP

model is essential in obtaining the right mechanical motion. The cardiac modeling community has had great success in studying the electrophysiology, however with the exception of the work by Niederer et al [NKB11] no formal verification analysis has been done. A verified numerical model needs to reproduce physiologically correct wave speed and chaotic scroll wave behavior. With modelers all over jumping on the "patient specific modeling" bandwagon there is a need to stipulate the validation criterion for any generic cardiac model. Also the modeling community typically has modeled the contractile mechanics of the heart separately from EP. However, in reality, the heart electrical and mechanical systems form an intimately networked feedback system. Thus the traditional, uncoupled approach to cardiac modeling is incapable of providing a fully coherent quantitative description of HF. Hence there is a burning necessity of laying out the verification and validation criterion for modeling coupled cardiac electromechanics.

Chapter 2 sets out the physiological background and mathematical models used to describe the voltage evolution, the ionic models which model the reaction part of the governing equation. A brief description of the "operator splitting" technique is then laid out. This technique lets using different time steps to solve the slow diffusion equation and the fast ionic current equations. It also provides a brief overview of cardiac excitation coupling. Chapter 3 compares different integration schemes which can be used with operator splitting. Finite element approximations are used to convert the non linear equations to discretized linear ordinary differential equations. Borrowing lumping strategy from structural analysis leads to different lumping schemes. These different schemes are compared against the benchmark problem proposed by Niederer et al [NKB11]. A convergence study on wave speed is performed to pick the schemes which gives maximum accuracy at least computational cost. Chapter 4 lays out the different validation criterion which needs to be satisfied by a computational model so that it can be used to further physiological studies. For the sake of validation a rabbit ventric-

ular model is used. A 6 lead electrocardiogram is generated from this model and scroll waves are reproduced in the model. Chapter 5 sets out the mathematical equations required to couple mechanics with electrophysiology. Proof of concept numerical simulations are performed on 2D and 3D model. A simplified ellipsoid representative of the heart is used to study the conditions required to reproduce the correct mechanical deformation. Finally Chapter 6 summarizes the outcomes from the thesis and lists the potential future modeling tasks which can help in the understanding cardiac arrhythmia.

CHAPTER 2

Cardiac electromechanics

2.1 Electrophysiology Modeling

The electrophysiological behavior in myocardial tissue can be modeled by means of differential equations, often as a combination of ordinary and partial differential equations (ODEs and PDEs). Ionic currents at the myocardial cell level are described by a model consisting of ODEs. These ionic currents are coupled via a model consisting of PDEs to describe the flow of electricity across the heart. A PDE model, such as the monodomain model, coupled with an ionic model can be used to simulate the electrical activity in the heart. The combination of nonlinear ODE's in the ionic model coupled with the complex geometry of the heart makes it impossible to solve the equation analytically.

2.2 Action Potential

In physiology, an action potential(AP) is the event in which the electrical membrane potential of a cell rapidly rises and falls, following a consistent trajectory. Action potentials are generated by special types of voltage-gated ion channels embedded in a cell's plasma membrane [BL07]. These channels are shut when the membrane potential is near the resting potential of the cell, but they rapidly begin to open if the membrane potential increases to a precisely defined threshold value. When the channels open (by detecting the depolarization in transmembrane voltage, they allow an inward flow of sodium ions, which changes the electrochemical

gradient, which in turn produces a further rise in the membrane potential. This then causes more channels to open, producing a greater electric current, and so on. The process proceeds explosively until all of the available ion channels are open, resulting in a large upswing in the membrane potential. The rapid influx of sodium ions causes the polarity of the plasma membrane to reverse, and the ion channels then rapidly inactivate. As the sodium channels close, sodium ions can no longer enter the cell, and they are actively transported out of the plasma membrane. Potassium channels are then activated, and there is an outward current of potassium ions, returning the electrochemical gradient to the resting state. After an action potential has occurred, there is a transient negative shift, called the "after hyperpolarization" or refractory period, due to additional potassium currents. This is the mechanism that prevents an action potential from traveling back the way it just came. For an isolated the cell AP is shown in Figure 2.1.

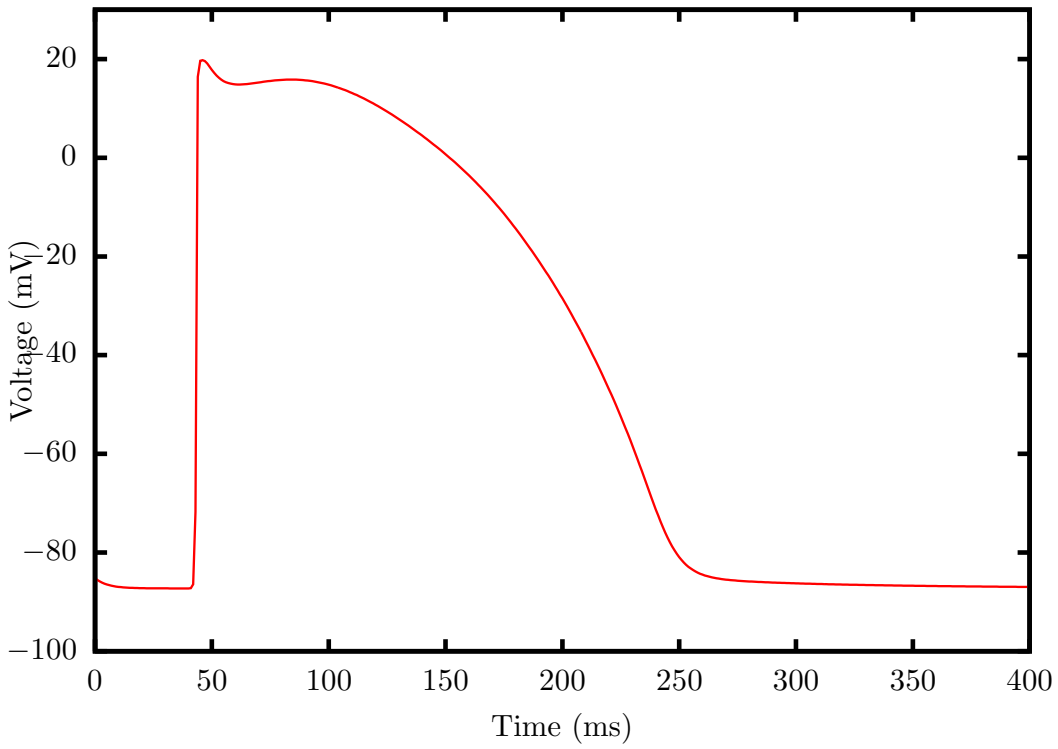

Figure 2.1: Action Potential of a single UCLA cell

2.3 Governing Equations

The bidomain model is a set of mathematical equations that govern the electrical properties of cardiac tissue. It was developed in the late 1970s, and is now used extensively in numerical simulations of the electrical behavior of the heart. The bidomain model is a two or three-dimensional cable model. It is a continuum model, in the sense that it predicts the electrical behavior averaged over many cells. The model accounts for the different electrical conductivities of the intracellular and extracellular spaces. When the extracellular voltage is dropped from the bidomain equation it yields the monodomain equation. Since the primary intent of this thesis is to study wave propagation it is sufficient enough to use the monodomain equations.

Let $\Omega \in \mathbb{R}$ denote the region occupied by the cardiac tissue. In the monodomain equations [KKS09] the transmembrane Voltage V is governed by

$$\chi \left(C\frac{\partial V}{\partial t} + I_{\text{ion}}(\boldsymbol{u}, V) \right) - \nabla \cdot (\sigma \nabla V) = I_{\text{stim}} \tag{2.1a}$$

$$\frac{\partial \boldsymbol{u}}{\partial t} = \boldsymbol{f}(\boldsymbol{u}, V) \tag{2.1b}$$

where σ is the conductivity tensor, C is the capacitance across the membrane, χ is the surface area to volume ratio and I_{stim} is the stimulus current. $\boldsymbol{u}$ are set of cell-level variables whose dynamic behavior is governed by the ODEs given by $\boldsymbol{f}$ and they couple back to the PDE through the ionic current I_{ion}. The single-cell ionic current is commonly modeled using the Hodgkin-Huxley framework [KKS09], describing the electrical activation potential of an excitable cell according to the solution of a set of nonlinear ODEs. The identities of the ionic variables describing the gating of specific channels, as well as the choice of specific functional forms for $\boldsymbol{f}(\boldsymbol{u}, V)$, are determined empirically according to careful experimental measurements of channel properties using patch-clamp techniques. For the sake of computational efficiency, the ionic response is sometimes modeled using simplistic phenomenological models like the two-variable Fitz-Hugh Nagumo model

which exhibit the general characteristics of an excitable cell but fail to reproduce the physiologically important features such as the sharp increase in voltage during the depolarization phase. There also exist more realistic models such as Luo Rudy II[LR94] and the UCLA model [MSS08] which are preferred from a computational and physiologically accurate simulations.

2.3.1 Operator Splitting Technique

The simplest strategy for adapting to the temporal multiscale character of the problem is operator splitting, which separates the slow diffusion process from the fast ionic process [LGT03, QG99, SWO12]. As first applied to the monodomain EP problem by Qu and Garfinkel [QG99], operator splitting techniques provide a straightforward way of dealing with multiple temporal scales. Broadly, the idea is to isolate the rapid local changes in voltage associated with cellular action potentials from the slow nonlocal process of diffusion. More specifically, by isolating the local ionic currents from nonlocal diffusion, significant computational speed-ups can be attained by adaptive control of time integration, using short time steps during the fast depolarization phase ($dV/dt \gtrsim 100$ mV/ms) and larger time steps during the slow depolarization phase ($dV/dt \sim 1$mV/ms). Because the fastest time-scales of the problem are associated with the action potential, both adaptive time-stepping and more sophisticated local implicit schemes specific to the cardiac ODEs [SLT01] can be used on a point-by-point basis to greatly reduce computational cost.

If we employ Strang splitting, as proposed by [QG99], which is second-order accurate (provided that the discrete time-integration methods for in each operator is also second-order accurate), then the monodomain PDEs of eqn. (2.1) are rewritten as

$$\chi C_{\mathrm{m}} \frac{\partial V}{\partial t} = \Gamma_1(V) + \Gamma_2(V; \boldsymbol{u}), \tag{2.2a}$$

where (linear and nonlinear) operators Γ_1 and Γ_2 represent the diffusion

$$\Gamma_1(V) = \nabla \cdot (\sigma \nabla V), \tag{2.2b}$$

and ionic current

$$\Gamma_2(V; \boldsymbol{u}) = -\mathcal{I}_{\mathrm{m}}(V; \boldsymbol{u}) \tag{2.2c}$$

processes. The basic idea of the Qu-Garfinkel operator splitting scheme is to alternate between integrating in time the diffusion and ionic operators. The structure of the scheme is sketched in Algorithm 1.

Algorithm 1 Qu-Garfinkel Operator Split [QG99].

Global time loop

for step $n = 1 \ldots n_{\max}$ **do**

i) $V = V_n$.

ii) Integrate Diffusion PDE for *half* time-step $\Delta t/2$:

$$\chi C_{\mathrm{m}} \frac{\partial V}{\partial t} = \nabla \cdot (\sigma \nabla V) \quad \rightarrow \quad V_{n+\frac{1}{2}}. \tag{2.3a}$$

iiI) Integrate Ionic ODE's for *full* time-step Δt:

$$\left.\begin{array}{rcl} & & V = V_{n+\frac{1}{2}} \\ \chi C_{\mathrm{m}} \frac{dV}{dt} & = & -\mathcal{I}_{\mathrm{m}}(V; \boldsymbol{u}) \\ \frac{d\boldsymbol{u}}{dt} & = & \boldsymbol{f}(V; \boldsymbol{u}) \end{array}\right\} \quad \rightarrow \quad V^*_{n+\frac{1}{2}}. \tag{2.3b}$$

iv) Integrate Diffusion PDE for *half* time-step $\Delta t/2$:

$$\begin{array}{c} V = V^*_{n+\frac{1}{2}} \\ \chi C_{\mathrm{m}} \frac{\partial V}{\partial t} = \nabla \cdot (\sigma \nabla V) \end{array} \quad \rightarrow \quad V_{n+1}. \tag{2.3c}$$

v) Step forward in time: $n \leftarrow n + 1$.

end for

2.4 Electrocardiogram

An electrocardiogram (ECG) is a routine clinical test that records the hearts electrical activity on the surface of the body. A typical ECG shows how fast the heart is beating; if the rhythm is steady or irregular; and the strength and timing of electrical signals as they pass through each part of the heart. ECG results are used to detect and study many health problems such as cardiac arrhythmias, heart attack, heart failure to name a few. The wave of repolarization manifests itself in the T wave of the ECG; therefore, irregularities in height and morphology of the T wave can be used as diagnostics of cardiac illness. Based on clinical observations of ECG, for a normal heart we expect, no fractionations, no slurring, smooth and fast upstroke for QRS, physiologically correct QRS width and the right QRS progression from the bipolar leads V1-V6. Several modelers have used ECG as a tool to validate the numerical model [BCF10, PDV09, BFG07, HK12]. However the ECG plots numerically recomputed show unphysiological characteristics. A schematic representation of the ECG is shown in Figure 2.2.

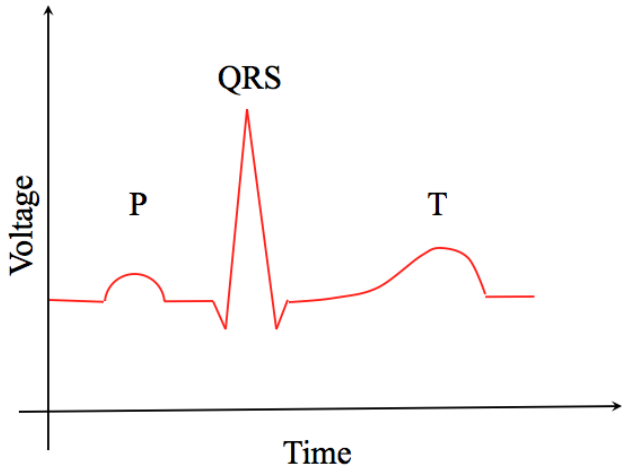

Figure 2.2: Schematic representation of the ECG

There is a close relationship between the electrical activity and the normal functioning of the heart. Hence measuring the electrical activity serves as an

efficient tool to measure hearts functionality. With each heartbeat, an electrical signal spreads from the top of the heart to the bottom. The process repeats with each new heartbeat. The hearts electrical signals set the rhythm of the heartbeat. A typical ECG consists of a P wave (atrial depolarization), QRS complex (RV and LV depolarization) and a T wave (RV and LV repolarization). The PR interval reflects the time required for the electrical impulse to travel from the sinus node through the AV node and into the ventricles and the ST internal denotes the time when the ventricles are depolarized.

2.5 Mechanics Modeling

As seen in the earlier section the electrical activity of the heart is followed by sequence of mechanical motions which results in heart pumping out blood. The right atrium receives blood from the body through the two caval veins, the superior caval vein receiving blood from the head, arms and thorax and the inferior caval vein receiving blood from the lower part of the body. The right ventricle delivers blood to the lungs through the pulmonary trunk. The blood from the lungs returns to the left atrium through the four pulmonary veins. The blood is ejected from the left ventricle to the aorta which transports blood to the systemic circulation.

Systole is the term used to describe the phase of contraction of myocardium causing emptying of blood and diastole is the term that describes the filling phase. Pressure differences drive blood flow. Myocardial contraction generates increased pressure when the valves are closed. This is an isovolumetric contraction. When the valves are open myocardial contraction also causes volume decrease as blood leaves the chamber. Systole and diastole of the atria and ventricles are separated in time. The rate of the filling and emptying of the ventricles are well established measures of ventricular diastolic and systolic function,respectively. The contribution of contraction in normal subjects is 10-20 % at rest but this atrial contribution

to stroke volume increases linearly with heart rate during exercise [KHG97, CJ89]. If we define EDV as the End Diastolic Volume and ESV as End Systolic Volume we can then define ejection fraction (EF) as

$$EF = \frac{EDV - ESV}{EDV}$$

For a normal human being EF ranges from $55 - 70\%$. This poses an interesting question of how does a contraction of $10 - 20\%$ result in a EF of $55 - 70\%$.

Sir William Harvey dissected cadaver hearts and concluded that the contraction of obliquely oriented fibers induces a torsion about its long axis. These observations have been confirmed in recent experiments [BMS08, SFW08]. These basic concepts are the currently accepted mechanism of cardiac function, but they do not explain the twisting phenomena observed during emptying and fillling of the viable beating heart that are seen during cardiac operations. An important progress in understanding this problem was achieved in [Sal69]. It was shown by a geometrical argument that helical arrangement of fibers, as a matter of principle, can help to resolve this paradox. The role played by the LV torsional rotation with respect to LV ejection and filling was only recognized recently by application of speckle tacking echocardiography [GCA10, HCE05]. [GG09, NG09] in their model of show that only the change in fiber angle produces the characteristic counterclockwise single loop relationship between torsion and ejection fraction:

2.6 Cardiac Excitation Coupling

The coupling in the heart is the process whereby an electrical stimulus is converted into muscle contraction. The basic steps of Excitation Coupling (EC) coupling in ventricular myocytes are shown in Figure 2.3

Depolarization of the T-tubule by the action potential causes the opening of L-type Ca^{2+} channels (also called dihydropyridine receptors, or DHPRs) and resultant inward flow of Ca^{2+} current (I_{Ca}). The Ca^{2+} that enters the cell stimulates

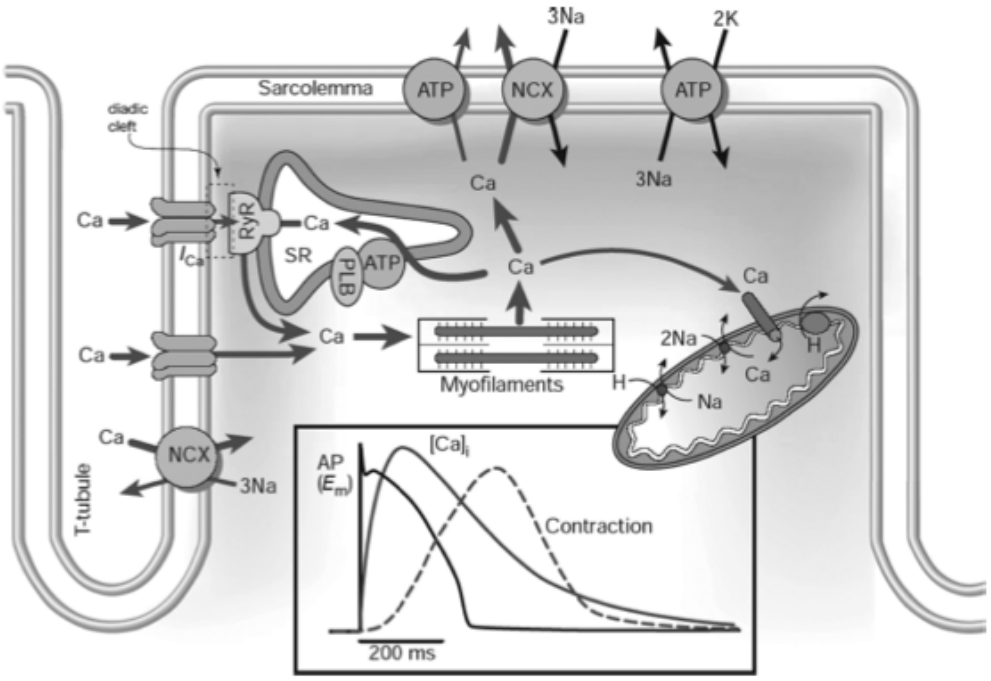

Figure 2.3: Cardiac excitation coupling mechanics [KKS09]

the release of additional Ca^{2+} from the SR via ryanodine receptors (RyR) by the process of Ca^{2+}-induced Ca^{2+} release, or CICR. This Ca^{2+} diffuses through the myoplasm and binds to the myofilaments, causing contraction, before being eventually removed from the myoplasm by ATPases, which pump the Ca^{2+} into the SR or out of the cell, or by the Na^+Ca^{2+} exchanger (NCX), which transfers Ca^{2+} to the outside of the cell [KKS09].

The graph in Figure 2.3 shows that the Calcium concentration lags behind AP and the mechanical deformation in turns lags behind the Calcium concentration. The Calcium and deformation curves are much smoother than AP and do not display sudden changes in derivative. Hence the deformation is much smoother than the voltage evolution and hence from a numerical stand point can be solved less frequently than the voltage evolution equations.

An ideal numerical model should include the dependence on deformation on

Calcium concentration. To get the correct concentration the EP equations need to be solve accurately enough in the same numerical model.

CHAPTER 3

Numerical quadrature and integration schemes

The cardiac reaction-diffusion equations are of multiscale nature, with variations occurring at both scales associated with both the tissue and individual cells, both in time and space. The simplest discretization schemes e.g., forward-Euler time-stepping with uniform mesh spacing require extreme computational expense to attain stability and accuracy. This has motivated tremendous efforts to find ways to speed up calculations. The spatial limitations on accuracy for cardiac EP simulation are determined fundamentally by the characteristic width of the pseudo wave front, a length scale that emerges from the ratio of the electrical conduction velocity to the rise time of the cardiac action potential. Recommendations for maximum element sizes range from 0.01 cm [Whi07] to 0.02 cm [LGT03, PMS11]. Convergence studies informing these guidelines generally rely on regular simulation domains and simple electrical activation patterns. The effects of discretization error for nonuniform physiological activation sequences in whole-heart simulation domains are less well studied.

For schemes using operator splitting [SLC06, TK04, QG99] because the ionic current is only needed at the nodes, all ionic state variables can be stored as nodal variables, and the ionic ODEs can be solved as uncoupled nodal equations. However, in a more general scenario where both reaction and diffusion terms are discretized by finite element interpolation, [Whi06, PBB10, ATP06, VAT02], ionic currents need to be computed at the quadrature points of the mesh. There is a question of which variables are defined at the nodes and interpolated to quadra-

ture points. The use of interpolation scheme can lead to significantly different numerical results in cardiac electrophysiology modeling in particular the conduction velocity of the electrical wave. Pathmanathan, et al. [PMS11] define all state variables (voltage, ionic concentrations, gating variables, etc.) as nodal quantities, and consider two approaches for obtaining currents at the quadrature points.

(a) Ionic Current Interpolation(ICI): Interpolate the ionic currents from the nodes inside the element and

(b) State Variable Interpolation (SVI): Interpolate the state variables of the cell model into the interior of the element and compute ionic current using these interpolated values.

SVI is the most accurate, but is associated with a high computational cost and increased storage requirements, whereas ICI is relatively inexpensive, but less accurate. So far no direct comparison has been made between these nodal-variable and internal-variable approaches.

It is noteworthy that operator splitting is the only approach that provides explicit spatial decoupling of the ionic ODEs and state variables. Hence, it is the only technique that allows for embarrassingly parallel adaptive time-stepping. However, the common drawback cited for operator splitting is the difficulty of ensuring numerical stability of the resulting scheme [BBP09]. Moreover, to achieve numerical accuracy comparable to that of the most accurate interpolating schemes (SVI, [PMS11]), operator-splitting approaches have so far required finer mesh sizes.

In this chapter we aim to understand the effects on numerical accuracy and computational efficiency of operator-splitting formulations produced by storing ionic state variables either at the nodes or at internal quadrature points, and specifically to discover whether the efficiency of adaptive operator splitting may be combined with the enhanced accuracy provided by interpolation techniques

such as SVI and ICI. Toward this first goal we introduce operator splitting as a post-discretiztion solution technique, and show how this approach produces several options for incorporation alternative interpolation techniques introduced by Pathmanathan, et al. [PMS11]. In particular, we study the effects of so called matrix lumping techniques on numerical convergence of formulations using operator splitting. We test the different formulations on a benchmark problem recently proposed by Niederer, et al. [NKB11], , and quantitatively compare the convergence rates using a 3D cable geometry. Secondly we expose some of the physiological consequences of excessive numerical discretization error. The standard tests of numerical accuracy for cardiac EP simulation in the literature tend to focus on convergence of activation times and conduction velocities in simple cable like geometries with uniform meshes. However it remains unclear what the practical impact of insufficient refinement is in physiologically realistic domains, which often require a distribution of element sizes, and always produce non- trivial activation sequences. Therefore we close the chapter by examining some physiological artifacts produced by discretization error in nonuniform meshes when simulating planar wave propagation and spiral wave break up in 2D domains.

3.1 Finite Element Discretization

Let the boundary of the domain be denoted $\partial\Omega$, with outward unit normal $\boldsymbol{n}(\boldsymbol{x}, t)$. The potential is assumed to satisfy a no-flux boundary condition on $\partial\Omega$,

$$I_{\perp} = (\sigma \nabla V) \cdot \boldsymbol{n} = \sigma_{ij} V_{,j} n_i = 0, \text{ on } \partial\Omega. \tag{3.1}$$

where

$$(\cdot)_{,j} = \frac{\partial(\cdot)}{\partial x_j}$$

denotes the spatial partial derivative, and summation is implied in the repetition of indices. To generate the weak form of the boundary value problem formed by eqns. (2.1) and (3.1), we form the weighted residual for some admissible weight

function ψ, an integrate by parts using the divergence theorem to obtain,

$$\int_\Omega \left[\chi\left(C_{\rm m}\frac{\partial V}{\partial t}+\mathcal{I}_{\rm ion}\right)-(\sigma_{ij}V_{,j})_{,i}-\mathcal{I}_{\rm stim}\right]\psi\,dv = \int_\Omega \left[\chi C_{\rm m}\frac{\partial V}{\partial t}\psi+\chi\mathcal{I}_{\rm ion}\psi+\sigma_{ij}V_{,j}\psi_{,i}-\mathcal{I}_{\rm stim}\psi\right]dv - \int_{\partial\Omega}\sigma_{ij}V_{,j}n_i\psi\,ds=0. \tag{3.2}$$

Due to the no flux boundary condition the surface integral vanishes. Furthermore, as is customary we can combine the stimulus and the ionic currents into a single current term $\mathcal{I}_{\rm m}=\mathcal{I}_{\rm stim}-\chi\mathcal{I}_{\rm ion}$, yielding the weak form as

$$\int_\Omega \left[\chi C_{\rm m}\frac{\partial V}{\partial t}\psi-\mathcal{I}_{\rm m}\psi+\sigma_{ij}V_{,j}\psi_{,i}\right]dv=0, \tag{3.3}$$

$\forall\,\psi$ admissible.

The domain is discretized into a set of subdomains (finite elements). In a standard isoparametric formalism, position within each element is parameterized by a set of curvilinear or natural coordinates $\{s^\alpha\}_{\alpha=1}^3$. The positions and voltage are interpolated among nodal values using piecewise polynomial shape functions $N_a(s^\alpha)$.

$$x_i^h = \sum_{a=1}^N x_{ia}N_a(s^\alpha) \tag{3.4}$$

$$V^h = \sum_{a=1}^N V_aN_a(s^\alpha) \tag{3.5}$$

$$\frac{\partial V^h}{\partial t} = \sum_{a=1}^N \dot{V}_aN_a(s^\alpha). \tag{3.6}$$

where x_{ia} denotes the i^{th} coordinate of the node a and V_a denotes the voltage at nodes a. The test functions are also expanded in the basis provided by these shape functions

$$\psi = \sum_{a=1}^N \psi_aN_a(s^\alpha),$$

where ψ_a are arbitrary nodal weights. Substituting these relations into the weak form of eqn. (3.3) produces

$$\sum_a \psi_a \int_\Omega \left[\chi C_{\rm m} \frac{\partial V^h}{\partial t} N_a + \sigma_{ij} V^h_{,j} N_{a,i} - \mathcal{I}_{\rm m} N_a \right] dv = 0 \tag{3.7}$$

Since ψ_a are arbitrary, their coefficients must then also be zero

$$\sum_{b=1}^{N} \left[C_{ab} \dot{V}_b + \sigma_{ab} V_b \right] - I_a = 0 \tag{3.8a}$$

or

$$\mathbf{C}\dot{\mathbf{V}} + \boldsymbol{\sigma}\mathbf{V} = \mathbf{I}. \tag{3.8b}$$

where

$$\mathbf{V} = [V_a], \tag{3.9}$$

$$\mathbf{C} = [C_{ab}], \quad C_{ab} = \int_\Omega \chi C_{\rm m} N_{\rm a} N_{\rm b} dv \tag{3.10}$$

$$\boldsymbol{\sigma} = [\sigma_{ab}], \quad \sigma_{ab} = \int_\Omega \sigma_{ij} N_{a,i} N_{b,j} dv \tag{3.11}$$

$$\mathbf{I} = [I_a], \quad I_a = \int_\Omega \mathcal{I}_{\rm m} N_a dv. \tag{3.12}$$

Here $I_{\rm a}$ is interpreted as the consistent nodal transmembrane current at node a, C_{ab} are the components of the capacitance matrix, and σ_{ab} are the components of the conductance matrix. The components of the conductance matrix require gradients of the shape functions. The spatial gradients of the shape functions are then computed by the chain rule as

$$N_{a,i} = N_{a,\alpha} J^{-1}_{\alpha i} \quad J_{i\alpha} = x^h_{i,\alpha}. \tag{3.13}$$

3.2 Numerical Quadrature and Matrix Lumping

In the semi-discrete finite element equations (3.8–3.12), spatial integration is performed over the entire domain, by global assembly of individual element integrals. In the standard form of numerical integration, evaluation of the integrand is done

at the Gauss-Legendre quadrature points inside every element. We will refer to this as Gauss integration. Let s_p^α and $\hat{w}_p$, $p = 1, \ldots, Q$ be the quadrature points and weights, such that

$$\int f(s^\alpha) d^3s \approx \sum_{p=1}^{Q} f(s_p) \hat{w}_p.$$

Also, denote $J \equiv \det[J_{i\alpha}]$, such that $dv = J d^3s$. The nodal ionic current computed by Gauss quadrature is

$$I_a = \sum_{p=1}^{Q} \left(\mathcal{I}_{\mathrm{m}} N_a \right)\big|_{s_p} w_p, \tag{3.14a}$$

and the capacitance and conductivity matrices are

$$C_{ab} = \sum_{p=1}^{Q} \left(\chi C_m N_a N_b \right)\big|_{s_p} w_p, \tag{3.14b}$$

$$\sigma_{ab} = \sum_{p=1}^{Q} \left(\sigma_{ij} N_{a,i} N_{b,j} \right)\big|_{s_p} w_p, \tag{3.14c}$$

where

$$w_p = J \hat{w}_p$$

are the effective quadrature weights for material and spatial integrals. Because the capacitance and conductivity matrices involve integrals of polynomial shape functions, Gauss quadrature of sufficiently high order provide exact results. However for the consistent nodal ionic currents, we expect results to generally depend on how the local current $\mathcal{I}_{\mathrm{m}}$ is computed at the quadrature points.

3.2.1 Internal State Variables at Gauss Points

In the case where ionic variables are defined as internal variables, stored directly at the quadrature points, as in [GK09, GK10, GWK10], then the evaluation of eqn. (3.14a) is unambiguous. Explicitly, the current at a Gauss point s^p is computed using the internal variables $\boldsymbol{u}_p$ stored at that Gauss point, and voltage

interpolated at Gauss point as per eqn. (3.5),

$$I_a^{\text{Gauss}} = \sum_{p=1}^{Q} \mathcal{I}_{\text{m}}(V^h(s_p), \boldsymbol{u}_p) N(s^p) w_p.$$

Because the interpolated voltage depends on surrounding nodal values via eqn. (3.5), it is clear that in this approach integration of the local internal ODEs is coupled to that of the global PDEs. Specifically, this makes it difficult to construct time-stepping schemes for the internal variables with time steps independent of that of the global nodal voltages.

3.2.2 Nodal State Variables

The alternative is to define ionic state variables as nodal variables, $\boldsymbol{u}_a$. To evaluate current at Gauss points, Pathmanathan, et al. [PMS11] classified the approaches in the previous literature by the following two categories.

State Variable Interpolation. The SVI approach is to interpolate the state variables to the Gauss points

$$\boldsymbol{u}^h(s^p) = \sum_{a=1}^{N} \boldsymbol{u}_a N_a(s^p)$$

and then to evaluate the ionic current using interpolated state variables and voltage as

$$I_a^{\text{SVI}} = \sum_{p=1}^{Q} \mathcal{I}_{\text{m}}(V^h(s^p), \boldsymbol{u}^h(s^p)) N_a(s^p) w_p$$

A downside to this is that it requires (at least temporary) storage of both nodal and Gauss-point values of the state variable array $\boldsymbol{u}$, which can have as many as 40 or more components for advanced cell models [MSS08]. The temporary storage of internal variables however isn't a big issued compared to the computational cost associated with interpolating the internal variables.

Ionic Current Interpolation. One alternative to SVI is the ICI approach, which computes current densities from the nodal state variables,

$$\mathcal{I}_a = \mathcal{I}_{\rm m}(V_a, \boldsymbol{u}_a)$$

and interpolates these to the Gauss points,

$$\mathcal{I}_{\rm m}^h = \sum_{a=1}^{N} \mathcal{I}_a N_a(s^p),$$

$$I_a^{\rm ICI} = \sum_{p=1}^{Q} \mathcal{I}_{\rm m}^h(s^p) N_a(s^p) w_p = \sum_{b=1}^{N} M_{ab} \mathcal{I}_b, \tag{3.15}$$

or

$$\mathbf{I} = \mathbf{M}\boldsymbol{\mathcal{I}} \tag{3.16}$$

where

$$M_{ab} = \int_\Omega N_a N_b dv \approx \sum_{p=1}^{Q} \left(N_a N_b\right)\big|_{s^p} w_p \tag{3.17}$$

are referred to as the components of the "mass matrix"

$$\mathbf{M} = [M_{ab}],$$

and

$$\boldsymbol{\mathcal{I}} = [\mathcal{I}_a]$$

is the vector of nodal current densities.

3.2.3 Nodal Quadrature

When state variables are stored along with voltages at the finite element nodes, an alternative approach to the SVI and ICI interpolation methods is to compute the nodal ionic currents by *nodal quadrature*. This approach places quadrature points at the nodes, with quadrature weight v_a representing the volume associated with node a. By the Kronecker-delta property of the shape functions, $N_a(\boldsymbol{x}_b) = \delta_{ab}$, the nodally integrated currents become

$$I_a^{\rm Nodal} = \sum_{b=1}^{N} \left(\mathcal{I}_{\rm m} N_a\right)\big|_{\boldsymbol{x}_b} v_a = \mathcal{I}_a v_a, \quad \text{(no sum on } a\text{)} \tag{3.18}$$

where, $I_a = \mathcal{I}_{\mathrm{m}}(V_a, \boldsymbol{u}_a)$ are currents computed from nodal state variables. Nodal quadrature is most closely related to ICI, in that both methods compute the consistent nodal currents I_a as linear combinations of the currents evaluated based on nodal state variables. In fact, the nodal quadrature result can be considered as a special case of the ICI result, in which the mass matrix is diagonal, $M_{ab} = \delta_{ab} v_a$ (no sum). Indeed, this is precisely what one obtains by performing a row-sum lumping approximation of the "full" or consistent mass matrix,

$$M^L_{ab} = \delta_{ab} \sum_{c=1}^{N} M_{ac} = \delta_{ab} \int_\Omega N_a \sum_{c=1}^{N} N_c dv = \delta_{ab} v_a,$$

where $v_a = \int_\Omega N_a dv$ can be interpreted as the volume of node a. As considered by Pathmanathan, et al. [PBN12], the ICI approach can be combined with lumping for either the mass matrix, the capacitance matrix ($C_{ab} = \chi C_m M_{ab}$), or both, with varying effects on accuracy. In particular, lumping of the capacitance matrix is especially convenient when explicit time-stepping schemes are used to increment the nodal voltage solution, as it avoids the need to solve a linear system. This is particularly attractive when combined with operator splitting, as we discuss below.

Notice that Algorithm 1 sketches the split in terms of undiscretized differential operators. If implemented in this traditional way, the diffusion updates in eqns. (2.3a,c) will need to be discretized in space with finite elements, leading to semi-discrete equations of the form,

$$\mathbf{C}\dot{\mathbf{V}} + \boldsymbol{\sigma}\mathbf{V} = \mathbf{0}. \tag{3.19}$$

On the other hand, in such an implementation the operator split naturally separates the ionic equations into *spatially decoupled, local, ordinary differential equations.* In other words, because no spatial gradients appear in the ionic updates in eqn. (2.3b), those equations do not need to be cast into a weak form and discretized with finite element shape functions — spatial discretization then trivially

entails applying these equations at the finite element nodes, i.e.,

$$\chi C_{\mathrm{m}} \dot{V}_a = \mathcal{I}_{\mathrm{m}}(V_a; \boldsymbol{u}_a) \tag{3.20a}$$

$$\frac{d\boldsymbol{u}_a}{dt} = \boldsymbol{f}(V_a; \boldsymbol{u}_a), \tag{3.20b}$$

where they can be discretized in time and solved directly.

Post-discretization Splitting. However, in practice we have a choice of whether to perform the split before or after performing the finite element discretization leading to the semi-discrete finite element equations (3.8). For the diffusion terms in the equations, the distinction is without a difference — both choices lead to the same linear system of ODEs in eqn. (3.19). For the ionic terms in the problem, however, if prior to performing the operator split we first apply the spatial finite-element discretization to the weak form of the governing equations, the ionic part of the split is represented by equations of the form

$$\mathbf{C}\dot{\mathbf{V}} = \mathbf{I}(\mathbf{V}, \mathbf{u}) \tag{3.21a}$$

$$\frac{d\boldsymbol{u}}{dt} = \boldsymbol{f}(V; \boldsymbol{u}). \tag{3.21b}$$

In this case, the vector of nodal currents $\mathbf{I}$ can be computed by Gauss quadrature with state variables stored at quadrature points, or by either SVI or ICI with state variables stored at the nodes, as described in the previous section. The ICI approach, moreover, allows for multiple variants, by selective lumping of $\mathbf{C}$ and/or $\mathbf{M}$. Pathmanathan, et al. [PBN12] considered two choices for matrix lumping without operator splitting: in what was termed *full lumping*, the capacitance and mass matrices are both lumped, whereas in *half lumping* only the capacitance matrix is lumped. However, as we discuss below, operator splitting of the ICI-formulated equations effectively expands the number of options, allowing for selective lumping of *three* matrices: a capacitance in the diffusion part of the split, and a capacitance and mass in the ionic part. As we will demonstrate, inconsistent lumping of the capacitance in the two parts of the split can yield

surprising improvements in numerical accuracy over the standard *full* and *half lumped* un-split approaches.

3.2.4 Matrix Lumping with ICI

Introducing the ICI current definition (3.16), the operator-split FE equations (3.19) and (3.21a) take the form

$$\mathbf{C}\dot{\mathbf{V}} + \boldsymbol{\sigma}\mathbf{V} = \mathbf{0} \tag{3.22a}$$

$$\mathbf{C}\dot{\mathbf{V}} - \mathbf{M}\mathcal{I} = \mathbf{0}. \tag{3.22b}$$

We consider six distinct variants of the operator splitting algorithm combined with ICI. These variants correspond to selective lumping of any of three matrices: $\mathbf{C}$ in the diffusion update (3.23), and $\mathbf{C}$ and $\mathbf{M}$ in the ionic update (3.21). While selective lumping of these three matrices generates $2^3 = 8$ total options, we show that certain combinations are equivalent, making for a total of six distinct variants. For the sake of conciseness, we will refer to the variants using a compact, three-character labeling convention described in Table 3.1.

Diffusion updates. For the diffusion step in the operator split, the choice to be made is whether or not to use the lumped approximation to the capacitance matrix. As is the case in structural dynamics, the main motivation for the lumping approximation is to render the capacitance a diagonal matrix, so that its inversion becomes trivial. This is mainly desired when explicit time-stepping strategies are use. If, for the sake of stability or accuracy (or both), *implicit* time-stepping is performed, requiring the solution of a non-trivial linear system, then a diagonal capacitance may have little impact on execution time. It is unclear *a priori* whether a full or lumped capacitance will lead to greater accuracy.

Table 3.1: Summary of the eight variants of Ionic Current Interpolation combined with operator splitting.

	Label	Diffusion Part	Ionic Part	
		$\mathbf{C}$	$\mathbf{C}$	$\mathbf{M}$
1.	**L-LL**	full	full	full
2.	$\equiv$ **C-LL**	full	lumped	lumped
3.	**L-CC**	lumped	full	full
4.	$\equiv$ **L-LL**	lumped	lumped	lumped
5.	**C-LC**	full	lumped	full
6.	**L-LC**	lumped	lumped	full
7.	**C-CL**	full	full	lumped
8.	**L-CL**	lumped	full	lumped

Ionic updates. For the ionic step, any combination of the capacitance and mass matrices may be lumped. The four cases are as follows:

LL. With both of the matrices lumped, the ionic update equation becomes

$$\mathbf{M}^L(\chi C_{\mathrm{m}}\dot{\mathbf{V}} - \boldsymbol{\mathcal{I}}) = \mathbf{0} \quad \text{or} \quad (\chi C_{\mathrm{m}}\dot{V}_a - \mathcal{I}_a)v_a = 0.$$

Because $v_a \neq 0$, the ionic equations reduce to the uncoupled form

$$\chi C_{\mathrm{m}}\dot{\mathbf{V}} - \boldsymbol{\mathcal{I}} = \mathbf{0} \quad \text{or} \quad \chi C_{\mathrm{m}}\dot{V}_a - \mathcal{I}_a = 0.$$

Clearly the fully lumped ionic solve is equivalent to nodal integration, which is tantamount to solving the strong form of the operator split equations (3.20) directly at the nodes. This is the widely used choice [SLC06] owing to two key computational benefits. First, because the capacitance matrices are diagonal, explicit time stepping for the voltage is made very efficient in both the diffusion and ionic solves. Secondly, because the ionic step is purely

local (i.e., involving only quantities at single nodes) it allows for "embarrassingly parallel," uncoupled time-stepping of the nodal equations, without any communication among processors in a distributed computing environment. This makes it possible to implement asynchronous adaptive time-stepping schemes, with integration of each node's ionic equations advancing from t_n to $t_{n+1} = t_n + \Delta t$ through a sequence of *sub-time steps*, τ_k, $k = 1, \ldots, K$, $\tau_K - \tau_1 = \Delta t$, with $\Delta\tau = \tau_{k+1} - \tau_k$ adaptively determined, for instance by the rate of change of nodal voltage [QG99].

Full lumping in the ionic part of the split can be combined with either of two options for the diffusion part, a full capacitance (**C-LL**) or lumped capacitance (**L-LL**). The latter choice, in which all matrices in both parts are lumped, corresponds to what Pathmanathan, et al. [PBN12] term *full lumping*. This is the standard choice used in codes that employ explicit time-stepping for the voltage. In the partially lumped (**C-LL**) option, the full capacitance in the diffusion part makes it necessary to use implicit schemes for voltage updates. However, because capacitance lumping contributes error to the solution[PBN12], we anticipate that this error might be mitigated by using the full capacitance in the diffusion part, while retaining a lumped capacitance in the ionic update in order to enjoy the advantages of asynchronous adaptive time stepping.

CC. The capacitance and mass in the ionic part are both full. The ionic update equation then becomes

$$\mathbf{M}(\chi C_{\mathrm{m}}\dot{\mathbf{V}} - \boldsymbol{\mathcal{I}}) = \mathbf{0}.$$

But again since $\mathbf{M} \neq 0$ the ionic equations uncouple to

$$\chi C_{\mathrm{m}}\dot{\mathbf{V}} - \boldsymbol{\mathcal{I}} = \mathbf{0}.$$

Thus this scheme turns out to be equivalent to $\mathbf{C}^L\mathbf{M}^L$. We see then that two of the eight lumping combinations are redundant: **L-LL**≡**C-LL** and

L-CC≡L-LL. This seemingly trivial result has surprising and important implications. It means that when operator splitting is employed, full lumping of the ionic part will yield solutions every bit as accurate as no lumping at all. This is in stark contrast to the situation without operator splitting [PBN12], where *full lumping* produces significant error. The apparent inconsistency suggests that perhaps the source of the error incurred by lumping is tied to the diffusion terms in the governing equations. We return to this point subsequently in the discussion of numerical studies below.

LC. Lumping of the capacitance but not the mass matrix is akin to the *half lumping* approach described Pathmanathan, et al. [PBN12]. In this case the ionic part becomes

$$\chi C_{\mathrm{m}} \mathbf{M}^L \dot{\mathbf{V}} = \mathbf{M}\boldsymbol{\mathcal{I}}$$

The ionic solve is no longer interpretable as purely local, node-by-node integration of ionic ODEs. The nodal ionic equations are not uncoupled as in the above cases. A particularly important consequence of the coupling generated by a full mass matrix is that during the ionic solve, the complete set of nodal ODEs, including the state variables,

$$\chi C_{\mathrm{m}} \mathbf{M}^L \dot{\mathbf{V}} = \mathbf{M}\boldsymbol{\mathcal{I}}, \quad \dot{\boldsymbol{u}}_a = \boldsymbol{f}(V_a; \boldsymbol{u}_a),$$

must be integrated *synchronously*. That is, asynchronous adaptive time stepping strategies, such as that of [QG99], cannot be employed when the ionic mass matrix is full. Thus the nodal equations (3.19) and (3.21) must be integrated simultaneously at a single fixed time step. This, in large part, defeats the main purpose of operator splitting, to algorithmically decouple the numerically stiff ODEs from the (non-stiff) parabolic PDEs. On the other hand, one remaining advantage to this approach is that it enables explicit time-stepping of the voltage, especially when combined with lumping in the diffusion part (**L-LC**), which is essentially a split version of the *half*

lumping scheme in [PBN12]. This being the case, we expect accuracy to be improved relative to the fully lumped case (**L-LL**).

CL. This combination represents a sort of *inverted half lumping*. The ionic equations become

$$\chi C_{\mathrm{m}} \mathbf{M} \dot{\mathbf{V}} = \mathbf{M}^L \boldsymbol{\mathcal{I}}.$$

The full capacitance now prevents both explicit time stepping of the voltage and asynchronous adaptive time stepping of the state variables. Thus we expect less computational efficiency from the two schemes stemming from this choice, **C-CL** and **L-CL**.

Therefore, we have six distinct variants of the ICI scheme, denoted by character codes as summarized in Table 3.1. In the following section, we assess the accuracy and convergence properties of these six schemes through a series of benchmark numerical studies.

3.3 Benchmark Studies

Here we present the results of numerical benchmark studies comparing the assortment of computational formulations considered in Section **??**.

3.3.1 Preferential matrix lumping schemes

To assess the performance of the six distinct matrix lumping options in the split ICI formulation, we make use of the benchmark posed by Niederer, et al. [NKB11]. As shown in Fig. 3.1 a rectangular block of dimension $2.0 \times 0.7 \times 0.3$ cm defines the domain, with monodomain EP modeled by the Ten Tusscher Epicardial model [TP06]. Following [NKB11] we set the Surface area to volume ratio as $\chi = 1400$ cm^{-1} and the membrane capacitance as $C_{\mathrm{m}} = 1\mu\mathrm{F}/\mathrm{cm}^2$. Conduction is defined to be transversly isotropic, with the fast-conducting fiber direction set along the

2.0 cm edge of the box. The conductivity σ was chosen as 0.1334mS/cm along the fastest direction (X axis) and along the other two axis σ was 0.0176mS/cm. A stimulus current of $50,000\mu$A/cc applied for 2 ms to corner 1 of the block over a set of nodes contained in a 0.15cm^3 cube. A sample mesh with element size 0.02cm is shown in Figure 3.1(b).

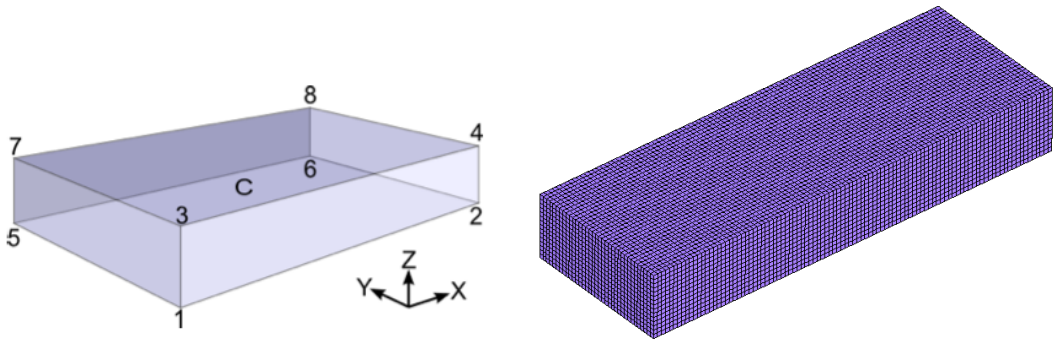

Figure 3.1: Rectangular domain from benchmark problem posed by Niederer, et al. [NKB11]. (a) Schematic showing voltage sampling points. (b) Example mesh of trilinear hexahedral elements with uniform edge length of 0.02 cm.

We use operator splitting to solve the diffusion and ionic parts of the ICI-formulated EP equations separately, as developed in Section **??**. The diffusion steps i) and iii) of Algorithm 1 are solved implicitly using Crank-Nicolson scheme. For instance, the step i) update takes the form

$$\mathbf{V}_{n+\frac{1}{2}} = \left(\mathbf{C} + \frac{\Delta t}{4}\boldsymbol{\sigma}\right)^{-1}\left(\mathbf{C} - \frac{\Delta t}{4}\boldsymbol{\sigma}\right)\mathbf{V_n}. \tag{3.23}$$

The ionic integration in step ii) is solved using the semi-implicit method introduced by Whiteley [Whi06], wherein the new state variables $\boldsymbol{u}_{n+1}$ are solved implicitly using the previous value of the voltage $V_{n+\frac{1}{2}}$, followed by an explicit voltage update. We break the full time step Δt into a number of ionic *sub-steps*, $\{\tau_0 = t_n, \ldots, \tau_k = \tau_{k-1} + \Delta\tau, \ldots, \tau_K = t_{n+1}\}$. The semi-implicit scheme solves allows relatively larger ionic sub-steps $\Delta\tau$ than explicit schemes. The implicit solution for the diffusion part is computed by the Conjugate Gradient method with

a Jacobi preconditioner as implemented in the Trilinos software package [HBH05]. Trilinear 8-noded hexahedral elements were integrated with 2^{nd} order (full) Gauss Quadrature.

The benchmark problem was solved using each of the six distinct operator-split matrix-lumping schemes summarized in Table 3.1. In each solution, the times were recorded when the voltage reached 0 mV at each of the locations indicated in figure 3.1(a). These results for the four best-performing schemes are listed in Table 3.2.

Results for the **L-CL** and **C-CL** schemes are not listed because solutions diverged for time steps greater than $\Delta t = 10^{-5}$ms. Activation time along a line connecting points P1 to P8 for the four best-performing schemes are shown in Figure 3.2

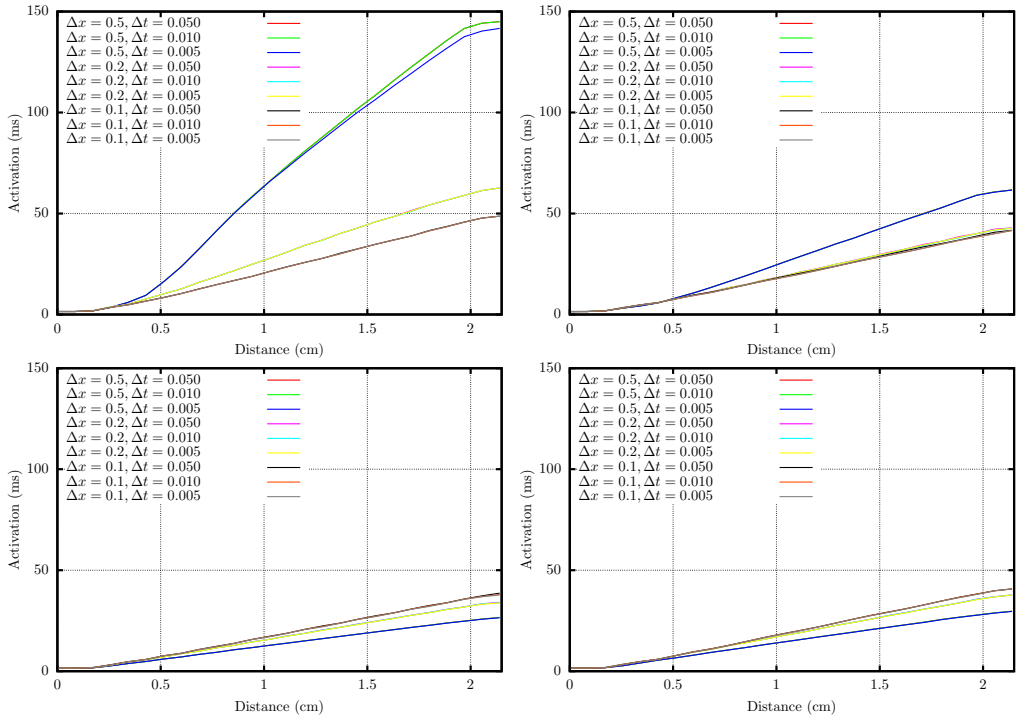

Figure 3.2: Activation time along line connecting P1 to P8 for schemes **L-LL, C-LL, C-LC** and **L-LC** for all different mesh and time step sizes.

The results in Figure 3.2 show very little sensitivity of the activation times

Table 3.2: Results from solution of Niederer Benchmark Problem [NKB11], using **L-LL**, **C-LL**, **C-LC**, and **L-LC** variants of the ICI formulation with operator splitting.

$\Delta x, \Delta t$	**P1**	**P2**	**P3**	**P4**	**P5**	**P6**	**P7**	**P8**	**C**
L-LL									
0.1, 0.005	1.46	32.68	9.56	34.69	30.68	47.62	33.49	48.68	22.67
0.1, 0.01	1.46	32.69	9.56	34.69	30.68	47.62	33.49	48.68	22.67
0.1, 0.05	1.46	32.70	9.57	34.72	30.68	47.63	33.54	48.69	22.72
0.2, 0.005	1.46	35.86	12.57	40.69	41.65	59.66	45.63	62.67	29.75
0.2, 0.01	1.46	35.87	12.57	40.69	41.65	59.66	45.23	62.67	29.75
0.2, 0.05	1.46	35.98	12.58	40.69	41.65	59.66	45.63	62.67	29.75
0.5, 0.005	1.46	60.30	29.61	69.95	124.34	139.62	127.63	141.62	69.49
0.5, 0.01	1.46	60.31	29.61	69.96	124.37	139.62	127.63	141.62	69.51
0.5, 0.05	1.46	59.56	29.64	69.65	125.66	141.08	129.59	142.75	66.69
C-LL									
0.1, 0.005	1.46	30.77	7.72	32.55	25.63	40.68	26.71	41.66	18.98
0.1, 0.01	1.46	30.79	7.72	32.58	25.63	40.69	26.71	41.68	18.98
0.1, 0.05	1.46	31.69	7.72	32.70	25.68	40.69	26.76	41.69	19.66
0.2, 0.005	1.46	30.69	8.71	31.70	28.68	41.97	30.68	42.77	19.90
0.2, 0.01	1.46	30.70	8.71	31.70	28.68	41.99	30.68	42.78	19.99
0.2, 0.05	1.46	30.71	8.71	31.75	28.68	42.63	30.68	43.57	19.99
0.5, 0.005	1.46	32.66	11.64	33.83	48.60	60.99	50.62	62.13	26.79
0.5, 0.01	1.46	32.65	11.64	33.82	48.59	60.88	50.61	61.95	26.77
0.5, 0.05	1.46	32.66	11.64	33.84	48.56	60.78	50.61	61.85	26.77

$\Delta x, \Delta t$	**P1**	**P2**	**P3**	**P4**	**P5**	**P6**	**P7**	**P8**	**C**
C-LC									
0.1, 0.005	1.46	29.91	6.75	30.74	21.91	37.57	23.59	37.73	17.83
0.1, 0.01	1.46	29.91	6.75	30.74	22.91	37.57	23.59	37.73	17.83
0.1, 0.05	1.46	30.66	6.76	31.44	22.08	37.69	23.67	37.99	17.87
0.2, 0.005	1.46	27.78	6.68	28.71	19.86	33.71	20.74	33.74	16.69
0.2, 0.01	1.46	27.78	6.68	28.71	19.86	33.69	20.75	33.74	16.69
0.2, 0.05	1.46	28.67	6.68	28.74	19.94	33.72	20.75	34.05	16.74
0.5, 0.005	1.46	23.82	4.70	24.45	17.16	26.00	17.57	26.47	13.41
0.5, 0.01	1.46	23.82	4.70	24.44	17.16	25.98	17.57	26.46	13.41
0.5, 0.05	1.46	23.83	4.70	24.47	17.16	26.02	17.54	26.48	13.42
L-LC									
0.1, 0.005	1.46	31.31	7.69	32.62	24.65	39.74	25.69	40.70	18.98
0.1, 0.01	1.46	31.31	7.69	32.62	24.65	39.74	25.69	40.71	18.98
0.1, 0.05	1.46	31.63	7.69	32.68	24.66	40.69	25.69	40.70	19.13
0.2, 0.005	1.46	30.64	7.51	30.94	22.78	37.43	23.72	37.72	18.58
0.2, 0.01	1.46	30.64	7.51	30.92	22.78	37.35	23.72	37.72	18.58
0.2, 0.05	1.46	30.68	7.51	31.54	22.79	37.35	23.72	37.72	18.58
0.5, 0.005	1.46	27.55	5.48	27.65	20.06	29.57	20.52	29.65	14.83
0.5, 0.01	1.46	27.56	5.48	27.65	19.98	29.56	20.49	29.65	14.83
0.5, 0.05	1.46	27.56	5.48	27.65	19.98	29.56	20.49	29.65	14.83

to time step for $\Delta t \leq 0.05$ at all mesh sizes. However, results are sensitive to the mesh size. Roughly the data appears to follow two trends. First, for schemes with a lumped mass matrix, **L-LL** and **C-LL**, activation times tend to decrease as Δx decreases. Second, schemes with full mass matrices, **C-LC** and **L-LC**, yield activation times that tend to increase as Δx decreases. Judging by these trends it would appear that the **C-LL** and **L-LC** schemes are likely the most accurate. These two variants converge from opposite directions, and have values that agree within a few percent for the finest meshes. Moreover these two variants give the least mesh sensitivity, with smaller discrepancies in activation times from the coarsest to finest meshes.

One way to interpret the convergence trends is to recognize the use of a full mass matrix in the ionic half-steps as equivalent to Laplacian smoothing of the ionic currents. A simple example demonstrates that this is the case. Let us consider a 1-D cable of two-noded linear Lagrange elements. The mass matrix for each element is given by

$$\mathbf{M}_e = \frac{1}{6}\begin{bmatrix} 2 & 1 \\ 1 & 2 \end{bmatrix} \tag{3.24}$$

The consistent nodal ionic currents are computed from nodal current densities as $\mathbf{I} = \mathbf{M}\boldsymbol{\mathcal{I}}$. After global assembly, this gives

$$\begin{pmatrix} \vdots \\ \mathsf{I}_{n-1} \\ \mathsf{I}_n \\ \mathsf{I}_{n+1} \\ \vdots \end{pmatrix} = \frac{1}{6}\begin{bmatrix} \ddots & \ddots & \ddots & \cdot & \cdot \\ \ddots & 4 & 1 & 0 & \cdot \\ \ddots & 1 & 4 & 1 & \ddots \\ \cdot & 0 & 1 & 4 & \ddots \\ \cdot & \cdot & \ddots & \ddots & \ddots \end{bmatrix} \begin{pmatrix} \vdots \\ \mathcal{I}_{n-1} \\ \mathcal{I}_n \\ \mathcal{I}_{n+1} \\ \vdots \end{pmatrix} \tag{3.25}$$

The global mass matrix can be decomposed as follows

$$\mathbf{M} = \frac{1}{6}\begin{bmatrix} \ddots & \ddots & \ddots & \cdot & \cdot \\ \ddots & 4 & 1 & 0 & \cdot \\ \ddots & 1 & 4 & 1 & \ddots \\ \cdot & 0 & 1 & 4 & \ddots \\ \cdot & \cdot & \ddots & \ddots & \ddots \end{bmatrix} = \begin{bmatrix} \ddots & \ddots & \ddots & \cdot & \cdot \\ \ddots & 1 & 0 & 0 & \cdot \\ \ddots & 0 & 1 & 0 & \ddots \\ \cdot & 0 & 0 & 1 & \ddots \\ \cdot & \cdot & \ddots & \ddots & \ddots \end{bmatrix} + \frac{1}{6}\begin{bmatrix} \ddots & \ddots & \ddots & \cdot & \cdot \\ \ddots & -2 & 1 & 0 & \cdot \\ \ddots & 1 & -2 & 1 & \ddots \\ \cdot & 0 & 1 & -2 & \ddots \\ \cdot & \cdot & \ddots & \ddots & \ddots \end{bmatrix}$$

or

$$\mathbf{M} = \mathbf{1} + \beta\boldsymbol{\mathcal{L}}$$

where $\mathbf{1}$ is the identity matrix, $\beta = \Delta x^2/6$, and

$$\boldsymbol{\mathcal{L}} = \frac{1}{\Delta x^2}\begin{bmatrix} \ddots & \ddots & \ddots & \cdot & \cdot \\ \ddots & -2 & 1 & 0 & \cdot \\ \ddots & 1 & -2 & 1 & \ddots \\ \cdot & 0 & 1 & -2 & \ddots \\ \cdot & \cdot & \ddots & \ddots & \ddots \end{bmatrix}$$

is the discretization of the Laplacian operator $\boldsymbol{\mathcal{L}}\boldsymbol{\mathcal{I}} \approx \nabla^2\mathcal{I}$. Accordingly the operation $\mathbf{I} = \mathbf{M}\boldsymbol{\mathcal{I}}$ represents a Laplacian smoothing of the nodal currents. The ionic integration step in the operator split is equivalent to a discretization of the *PDE*

$$\frac{\partial V}{\partial t} = \mathcal{I}(V) + \beta\nabla^2\mathcal{I}(V).$$

In other words, the numerical smoothing provided by the full mass matrix is interpreted as producing some algorithmic diffusion of the ionic currents. It follows that this artificial diffusion should augment the physical diffusion in the monodomain equations. An artificial increase in diffusion is consistent with observation conduction velocities increasing with mesh size for the full-mass **L-LC** and **C-LC** methods.

This interpretation may also help to explain why the **L-CL** and **C-CL** methods tend to diverge: in each of those cases the use of a full capacitance and a lumped

mass produces the opposite of smoothing — *sharpening*. Explicit updates of the voltage then take the form $\mathbf{V}^n = \mathbf{V}^{n-1} + \Delta t \mathbf{C}^{-1}\mathbf{M}^L\boldsymbol{\mathcal{I}}$. Because the full capacitance has the same structure as the mass, it is also effectively a smoothing operator. Therefore $\mathbf{C}^{-1}$ acts as a *sharpening* operator, i.e., having the opposite effect of smoothing the nodal currents, presumably destabilizing the numerical solution.

Similar to activation plots shown in Niederer et al [NKB11] to show the impact of changing spatial resolution on activation wave, and propagation along and across the preferential fiber direction, we evaluated activation times in the plane shown first row in Figure 3.3. Schemes **C-LC**, **C-LL** and **L-LC** show minimal variation compared to **L-LL**. To further quantify it mathematically we perform a stability analysis of $\mathbf{-CL}$ and $\mathbf{-LC}$ schemes.

3.3.2 Stability Analysis

From a stability standpoint we need

$$U_m^n - \tilde{U}_m^n \equiv Z_m^n$$

where for a given grid U_m^n represents the theoretical solution at the given grid location n, m, $\tilde{U}_m^n$ represents the numerical solution at the same location and Z_m^n represents the error. We need to find the condition under which the error remains bounded as $n, m \to \infty$. One of the schemes used to examining this notion of stability is the matrix method[MG80]. This is applicable to initial value problems can be used there. If the differential equations can be represented to the form

$$\mathbf{AU^{n+1}} = \mathbf{BU^n}$$

we rewrite this typically as

$$\mathbf{U^{n+1}} = \mathbf{CU^n}, \quad \mathbf{C} = \mathbf{A}^{-1}\mathbf{B}$$

For stability we need

1. The spectral radius condition

$$\rho(C) \leq 1$$

which is necessary for stability and

2. the norm condition

$$||C|| \leq 1$$

which is sufficient for stability.

3.3.2.1 LC lumping scheme

Here we solve

$$C_m \mathbf{M^L} \dot{\mathbf{V}} + \mathbf{M}\mathcal{I} = 0$$

So the matrix $\mathbf{C} = \mathbf{M}(\mathbf{M^L})^{-1}$ is the one we want to analyze from stability stand point. Since $\mathbf{M^L}$ is a diagonal matrix we can take the inverse by inverting the diagonals. We consider the case of assembly of bar element with element size (200μm which is what is used in the analysis) and compute the eigenvalues of $\mathbf{C}$. The maximum modulus eigenvalue for this matrix is $0.000399 < 1$. Also the 2 norm or the Frobenius norm for this matrix is $0.005656 < 1$. Hence we have the necessary and sufficient conditions for stability satisfied.

3.3.2.2 CL lumping scheme

Here we solve

$$C_m \mathbf{M} \dot{\mathbf{V}} + \mathbf{M^L}\mathcal{I} = 0$$

So the matrix $\mathbf{C} = \mathbf{M}^{-1}\mathbf{M^L}$ is the one we want to analyze from stability stand point. This is nothing but the inverse of $\mathbf{C}$ in the earlier case. The maximum modulus eigenvalue for this would be the inverse of the minimum modulus eigenvalue from the earlier case. Hence we get $7499.76 > 1$. This does not satisfy the

necessary condition for stability and hence warrants the need for a very small time step.

For the schemes **L-LL** and **C-LL** activation time curves have a common morphology, with the activation wave increasing in velocity as the meshes were refined (Figure 3.4). However schemes **C-LC** and **L-LC** exhibit the opposite, the activation wave decreasing in velocity with meshes refined. The change in velocity is less pronounced in **C-LL**, **C-LC** and **L-LC** compared to **L-LL**.

3.3.3 Wave speed convergence

The results from the benchmark problem from [NKB11] allow for straightforward comparison of the ICI operator-split variants with each other and with other published solvers. To more systematically study the convergence of our implementations, we have also used them to solve for unidirectional wave propagation in a simple 3-D cable. In particular we compare the two putatively most accurate schemes **C-LL** and **L-LC**, with the fully lumped **L-LL** scheme most common in the literature and **C-LC**. A 3D cable of length 2 cm was used to study the effect of mesh size on these formulations. One end of the cable was stimulated for 5 ms by 50000 μA/cc. The activation times at several different locations in the cable (when $V = 0$mV) were recorded, and the conduction velocity (v^h) was computed by linear regression. The conduction velocity for a mesh size of 10μm was chosen as the converged velocity (v^*). Figure 3.5 shows the comparison between the usual full lumped formulation and the proposed formulation with preferential lumping. The plot confirms that the **C-LL** and **L-LC** converge more quickly than the standard fully-lumped formulation **L-LL**. The time steps chosen were $\Delta t = 0.1$ms and $\Delta\tau = 0.01$ms. The other key feature to take away from this plot is that beyond a mesh size of 200μm the wave speed is questionable even with the most accurate schemes. This is of importance while using automatic meshers to generate a mesh in a typical 3-D cardiac analysis. While the average element size might be less

than 200 μm, any elements of size greater than 200μm may produce spurious local differences in conduction velocity.

3.3.4 CPU efficiency

The choice about which formulation to employ hinges not only on accuracy, but also on the computational efficiency. To compare CPU times, we tested the two most accurate schemes **C-LL** and **L-LC** on uniaxial propagation in a 2-D bar 6×2 cm, meshed with a uniform element size of 200 μm. Nodes lying with 0.2cm of the left end of the bar were applied a stimulus current of 50000μA/cc for 5 ms. Nodes lying with 0.2cm of the left end of the bar were applied a stimulus current of 50000μA/cc for 5 ms. Conduction velocity was computed based on the activation times at at $x = 0.5$cm and $x = 2.0$cm. For the **L-LC** scheme, the global assembly of the ionic current vectors need to be performed in each sub-step of the ionic integration step $\Delta\tau$. Therefore this method was performed using uniform ionic sub-time steps. For the **C-LL** scheme, on the other hand, a lumped mass matrix renders the nodal ionic updates completely decoupled, enabling asynchronous adaptive time stepping as noted above. The ionic sub-time-step $\Delta\tau$ is adapted for each node independently based on the the value of dV/dt, following Qu and Garfinkel [QG99].

Table 3.5 shows the computed conduction velocities along with the CPU times required for 5 ms of simulation using several different time steps. The data show that conduction velocity tends to increase as time steps are reduced. Accuracy appears to be slightly better for **C-LL**, with slightly higher ($\approx 4\%$) conduction velocities than **L-LC**. CPU times for the two methods differ by negligible amounts. Algorithmically, there are two main differences between the methods: (i) **L-LC** requires a global assembly operation in each ionic sub-step whereas **C-LL** does not; and (ii) **C-LL** requires the solution of a linear system in each implicit diffusion sub-step, whereas **L-LC** does not. With the linear solution computed with

Table 3.5: Comparison in CPU time between **L-LC** and **C-LL** schemes. Ionic substeps are uniform, except for the last row, where $\Delta\tau$ is adapted asynchronously for each node independently following [QG99]. * uses adaptive time-stepping

Method	Δt (ms)	$\Delta\tau$ (ms)	Conduction Velocity (m/s)	CPU time (s)
L-LC	0.1	0.1	0.522	16.69
	0.1	0.05	0.532	27.72
	0.1	0.01	0.555	123.76
C-LL	0.1	0.1	0.536	17.06
	0.1	0.05	0.549	27.64
	0.1	0.01	0.561	131.75
	0.1	0.01–0.1*	0.543	18.113

a preconditioned conjugate gradient solver, both of these operations turn out to be order N in the number of nodes. Therefore it may not be surprising that computational costs roughly cancel out. The only significant difference in performance between the two methods comes from employing asynchronous adaptive time-stepping for the ionic solve in **C-LL**: the final row of Table 3.5 shows that setting $\Delta\tau$ adaptively between 0.1 and 0.01 ms yields a CPU time roughly equal to that of a fixed $\Delta\tau = 0.01$ ms simulation, but with accuracy closer to that of a fixed $\Delta\tau = 0.1$ ms simulation.

3.4 Effect of mesh size on wave speed

To get a sense for the mesh-dependence of our operator split schemes in a more complex setting, we here simulate, the effect of non uniform mesh on wave velocity. One of the key findings from the convergence studies above is that for element sizes above 100–200 μm the conduction velocity attained from most of the schemes is

highly sensitive to mesh size. While for uniform meshes such as used in the above studies this mesh dependence produces noticeable quantitative errors, it can lead to even qualitative differences when applied to nonuniform meshes, as are commonly generated with automatic meshing software [TCG11, VAP10, PKA09]. To illustrate this, here we consider unidirectional EP propagation in a 2D block 6cm $\times$2cm, meshed with a non-uniform quadrilateral mesh, and integrated with the **L-LC** scheme. Bilinear quadrilateral elements were used with 2^{nd} order gauss quadrature. The geometry was divided into three regions. Two difference cases were considered. In the first case the first rectangular region starting from $(0, 0)$ to $(2, 2)$ was meshed with 100μm elements. The second rectangular region starting from $(2, 1)$ to $(6, 2)$ was meshed with element size 200μm and the third rectangular region from $(2, 1)$ to $(6, 0)$ was meshed with 100μm elements. The transition in element size between region 1 to 2, 1 to 3 and 2 to 3 creates a non-uniform mesh in regions 2 and 3. The minimum edge size was 67μm, the average was 119μm and the maximum was 256μm. In the second case the edge region with 100μm elements was meshed with 200μm elements and the region with 200μm region was meshed with 400μm elements. The minimum edge size was 130μm, the average was 238μm and the maximum was 516μm. The mesh was meshed in this fashion to show the effect of wave speed on mesh size.

The nodes in the left end within an region of 0.15cm were stimulated for 4ms with a stimulus current of $50,000\mu$A/cc. Schematic representation of the mesh settings and voltage snapshots at various time intervals are shown in Figure 3.6. At the end of 37ms the wave front is still in the uniform mesh region and remains straight and perpendicular to the lateral boundaries. After this the wave enters the non-uniform mesh region. At 49ms we can see the wavefront bending in the coarser nonuniform mesh. The wavespeed in the finer mesh region is faster than the wave speed in the coarse mesh region. At 69ms it bends even more and is more pronounced at 100ms. The wave bending is not that pronounced in the finer

nonuniform mesh. By subdividing the geometry and meshing different regions with varied element sizes, we mimic the automated segmentation and meshing procedures that have become common in cardiac modeling [TCG11, VAP10, PKA09]. The ratio of largest to smallest element edge in the present example is less than 5, and completely within the common range for automated hexahedral and tetrahedral meshing software. The distortion of the wavefront produced by the larger elements illustrates that the potential for artifactual results is determined more by the largest element size than by the average. Based on the convergence studies in the previous sections, we expect that meshes with elements larger than 200 μm are likely to produce artifactually fast conduction. When large elements are isolated to certain regions, as in the present example, they may cause wavefronts to distort and even change direction.

3.5 Spiral break

While simplified bar/slab geometries with uniaxial conduction are appropriate for systematic convergence studies, more physiologically relevant simulations commonly involve complex geometries and non-uniform conduction. Spiral waves were created using a "S1-S2" protocol. The initial stimulus (S1) was applied uniformly along the left edge of a 6-cm square block for 4ms with a stimulus current of $50,000\mu A/cc$. The second stimulus (S2) was activated after a delay of 265ms subsequent to S1, over a 1-cm radius circular disc offset from the center of the block by 1cm along the Y axis, for 3 ms, also at $50,000\mu A/cc$. The S1-S2 delay time was adjusted by trial and error to produces a spiral wave. Figure 3.7 shows the sequential activation of S1 and S2 stimuli in the block. The model was meshed with fully-integrated bilinear quadrilateral elements. The ionic currents were defined using the Luo-Rudy-II ionic model [LR94]. Five different cases were considered to study the effect of mesh size of producing physiologically acceptable

spiral waves (Table 3.8), uniform mesh with 100μm sized elements, uniform mesh 200μm sized elements, uniform mesh 400μm sized elements, nonuniform mesh with two edges set to 150μm and other two set to 200μm sizes elements (Edge sizes: minimum 112μm, average 173μm and maximum 248μm), and nonuniform mesh with two edges set to 200μm and other two set to 400μm sized elements (Edge sizes: minimum 138μm, average 279μm and maximum 496μm). The uniform 100μm, 200μm and the nonuniform $150-200$μm show a good agreement in the voltage evolution. However the results from 400μm mesh even at T= 19ms shows a non smooth wavefront. The wavefront exhibits the presence of corners which is physiologically not acceptable. Also the wave front is not smooth and is jaggedly. The non smooth wavefront also exhibits in the nonuniform $250-400$μm mesh, but not as pronounced as in the 400μm mesh. The presence of non smooth wavefront can be observed all the time steps for 400μm mesh in Figure 3.8. This is attributed to the large element edge size.

The nonuniform $250-400$μm mesh while evolving from T= 155ms to T= 185ms shows a different break up pattern. All the other meshes show two spiral waves, however even in the presence of excitable media the spiral arm in the bottom gets extinguished. This again can be attributed to large element edge size

3.6 Inferences

Based on the studies we infer that with "mass lumping" we get the decoupling of nodal equations governing time evolution of voltage, thereby allowing for trivial local time-stepping updates, which are much more CPU-efficient than the solution of coupled linear systems with global (but sparse and banded) matrices. Adding to the observations of others [PMS11] , we have shown that this efficiency can sometimes come at a cost of reduced accuracy and can produce a wide range of convergence behaviors. Two schemes in particular, **L-LC** and **C-LL** – exhibit

excellent accuracy in addition to (or despite) increases in efficiency relative to a fully consistent implementation.

In the **L-LC** scheme, the lumped approximation of capacitance is used in both the diffusion and ionic parts of the operator split, and the consistent ionic mass matrix is used in the ionic update. The lumping of all capacitance matrices in this scheme, which is akin to what Pathmanathan, et al. [PMS11] label "half lumping, allows for explicit time updates to the voltage to be computed trivially, without the need for solving any global linear system. The multiplication of nodal current densities by a consistent mass matrix can be interpreted as producing an additional (artificial) diffusion of ionic currents, which has the effect of speeding up wavefronts, causing the conduction velocity to converge from above as meshes are refined. Despite the speedups afforded with explicit voltage updates, the consistent mass matrix formulation prevents asynchronous, adaptive time-stepping of the ionic part of the operator split, one of the key sources of efficiency afforded by operator splitting. However, the **L-LC** scheme does allow for global sub-stepping in the ionic solution step. In other words, some efficiency can be gained by doing diffusion updates (Δt) less frequently than ionic updates ($\Delta\tau < \Delta t$) while still maintaining comparable accuracy.

In contrast, the **C-LL** scheme employs a consistent capacitance in the diffusion part of the operator split, and lumped approximations of both the capacitance and mass matrices in the ionic part. Use of the consistent capacitance in the diffusion part can be rationalized a posteriori in light of two considerations. First, with ionic sub-stepping ($\Delta\tau < \Delta t$) employed, the diffusion part is solved less frequently; thus any reduction in efficiency in a diffusion time step is less consequential than in an ionic time step. But second and more important, because explicit time-stepping of the diffusion part places excessive requirements on the time step t, it is generally more efficient, and comparably accurate to use implicit time-stepping for the diffusion updates. Thus, lumping of the capacitance

has minimal impact on efficiency of the solution of the linear system for an implicit (e.g., a Crank- Nicholson) diffusion update. In light of this logic, it seems more productive to search for ways of speeding up the ionic part of the operator split. The lumped approximation of both the capacitance and mass matrices in the **C-LL** scheme does this optimally, by completely decoupling the nodal equations into local ODEs. Remarkably, this single modification to the standard fully lumped approximation of the operator split equations, using a consistent capacitance matrix only in the diffusion update, allows us to have our cake and eat it too. That is, it yields a scheme with accuracy rivaling fully consistent and fully coupled implementations (e.g., ICI and SVI in [PMS11]), but capable of enjoying the tremendous computational speed-ups afforded by asynchronous adaptive time-stepping of the decoupled nodal ionic equations [SWO12].

We find that results are generally satisfactory for the **L-LC** and **C-LL** schemes when element sizes are less than about 200μm. Other lumping combinations require meshes of at least twice the element density for acceptable accuracy. We demonstrated that particular attention to mesh sensitivity must be given when computing with nonuniform meshes, as are the common result of automated segmentation and mesh generation software. For nonuniform meshes it is generally the size of the largest elements (and not the smallest or average) that controls the accuracy of the solution and the presence or absence of spurious artifacts. We encountered two key implications of these observations for physiological simulation studies. Local gradients in mesh density, when allowing element sizes to rise above $h \approx 200\mu$m, can cause artifactual changes in the curvature of wavefronts. As demonstrated in the context of re-entry and spiral wave breakup, such errors can lead to predictions that are qualitatively incorrect, e.g., spurious "corner formation in wave fronts, or even the extinguishing of waves that should continue to propagate. These results underscore the importance of simulating with sufficiently refined meshes.

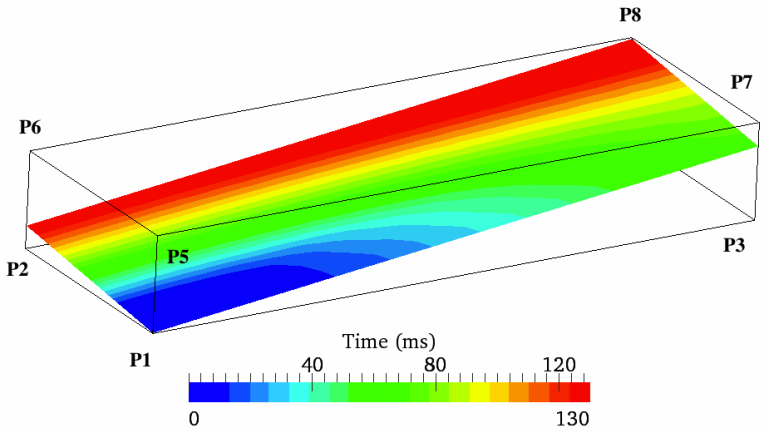

Scheme	$\Delta x = 0.5$mm and $\Delta t = 0.005$ms	$\Delta x = 0.1$mm and $\Delta t = 0.005$ms

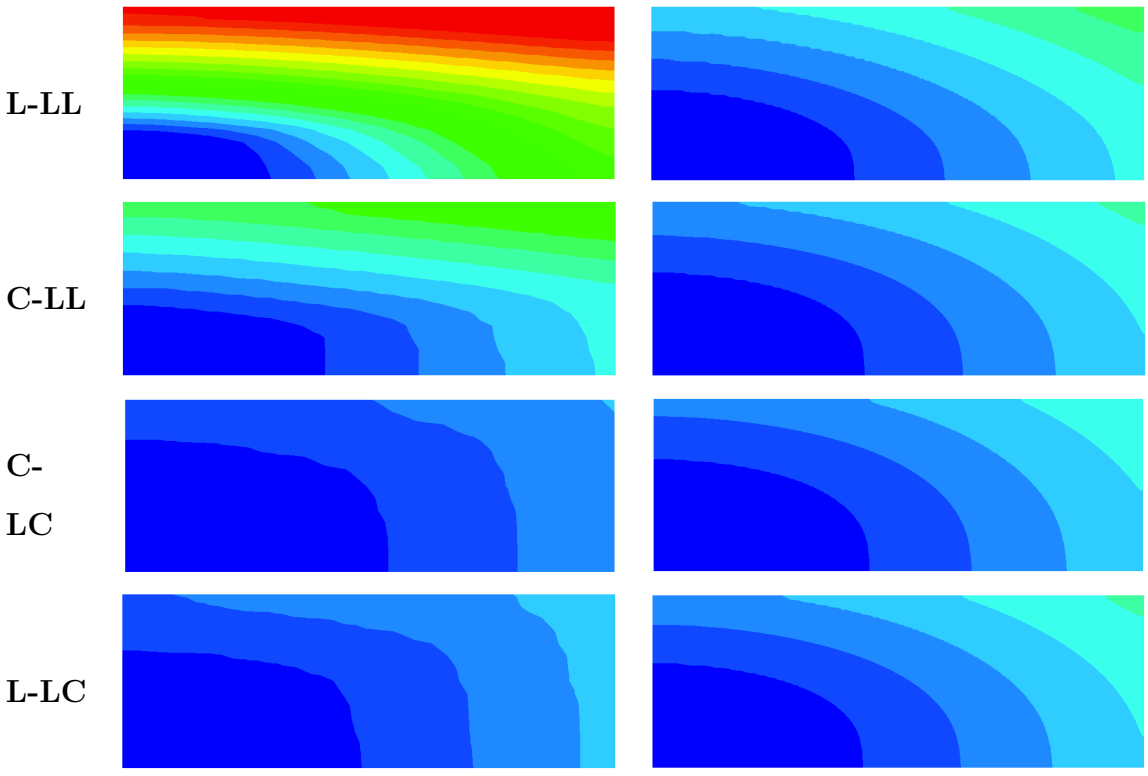

Figure 3.3: For a slice plane connecting points P1 and P8 the activation times comparison between four different schemes show minimal difference in results between different mesh sizes for **C-LC** and **L-LC**.

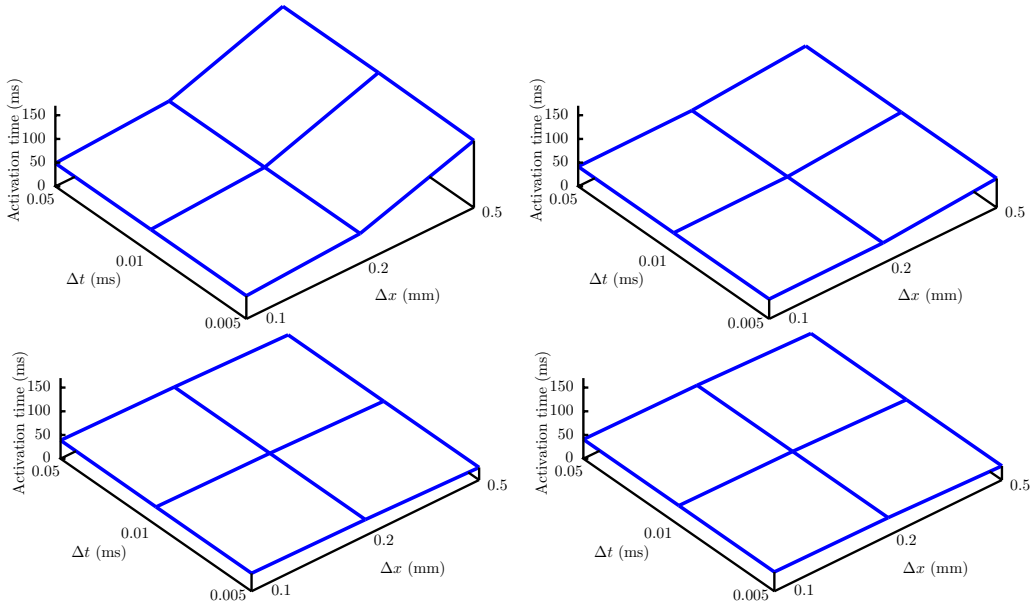

Figure 3.4: Activation time at point P8 depicted in Figure 3.3 for every combination of spatial and temporal refinement. The cases shown correspond to **L-LL**, **C-LL**, **C-LC** and **L-LC**

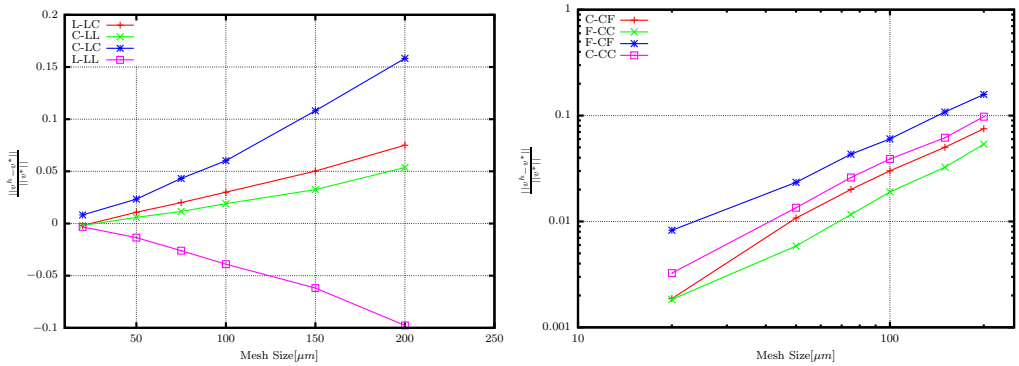

Figure 3.5: Convergence rate of different formulations. The plot on the right is plotted using log–log scale. All schemes show similar to convergence rates, however **L-LL** converges from the bottom while the other schemes from top and **C-LC** does not approach the converged value v^*.

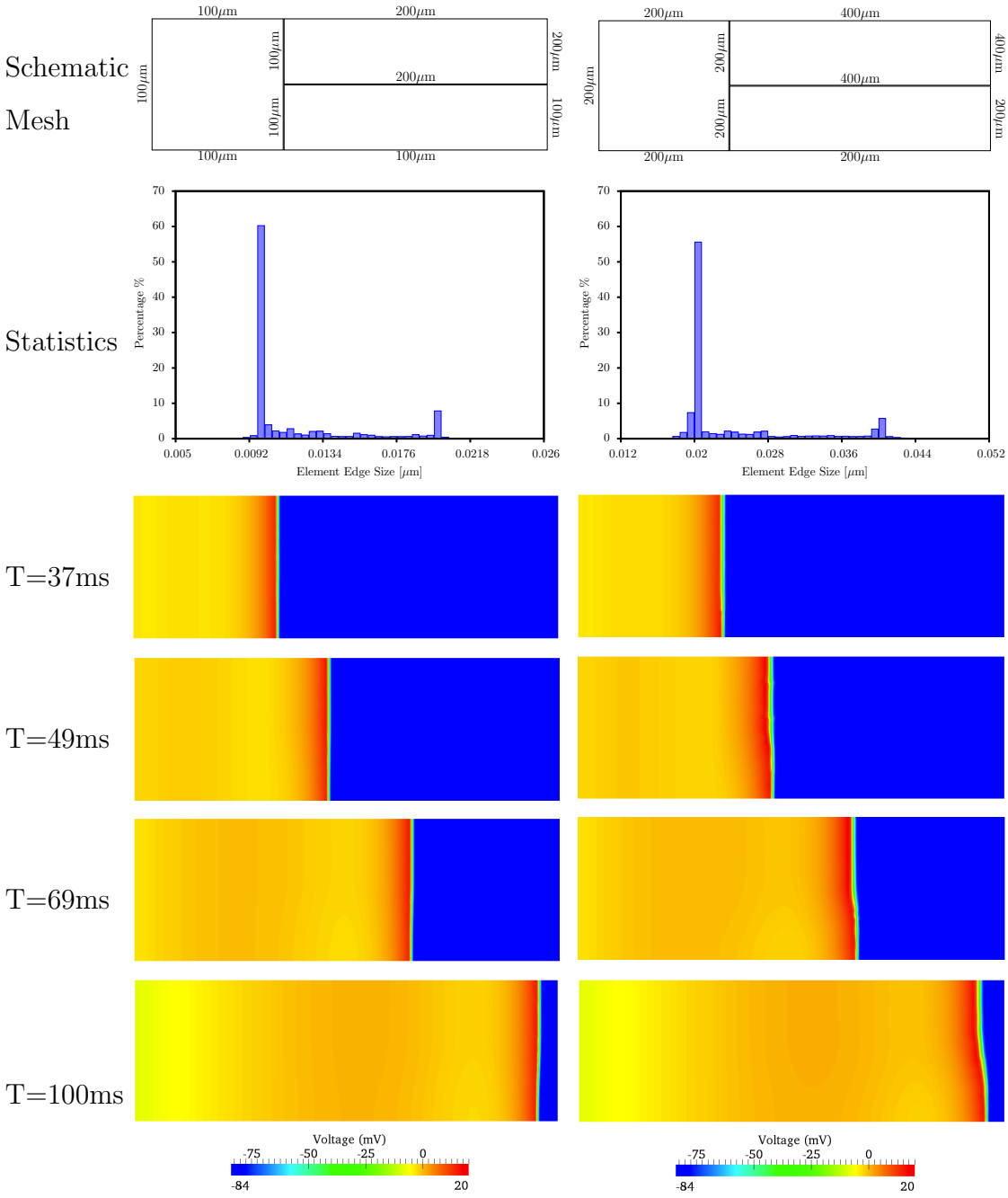

Figure 3.6: Figure Comparison of voltage between two non uniform meshes; finer one with 67μm $\leq \Delta x \leq$ 256μm and coarser one with 130μm $\leq \Delta x \leq$ 515μm. The finer nonuniform mesh shows minimal variation in the wavefront compared to the coarser nonuniform mesh.

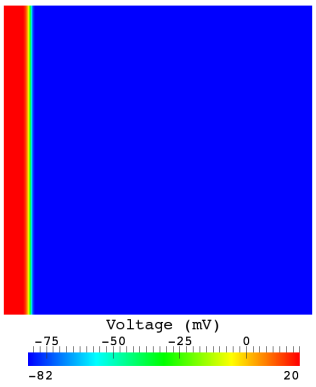

(a) S1 stimulus

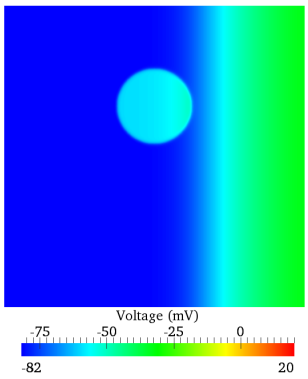

(b) S2 stimulus

Figure 3.7: S1 and S2 stimulus locations on the block

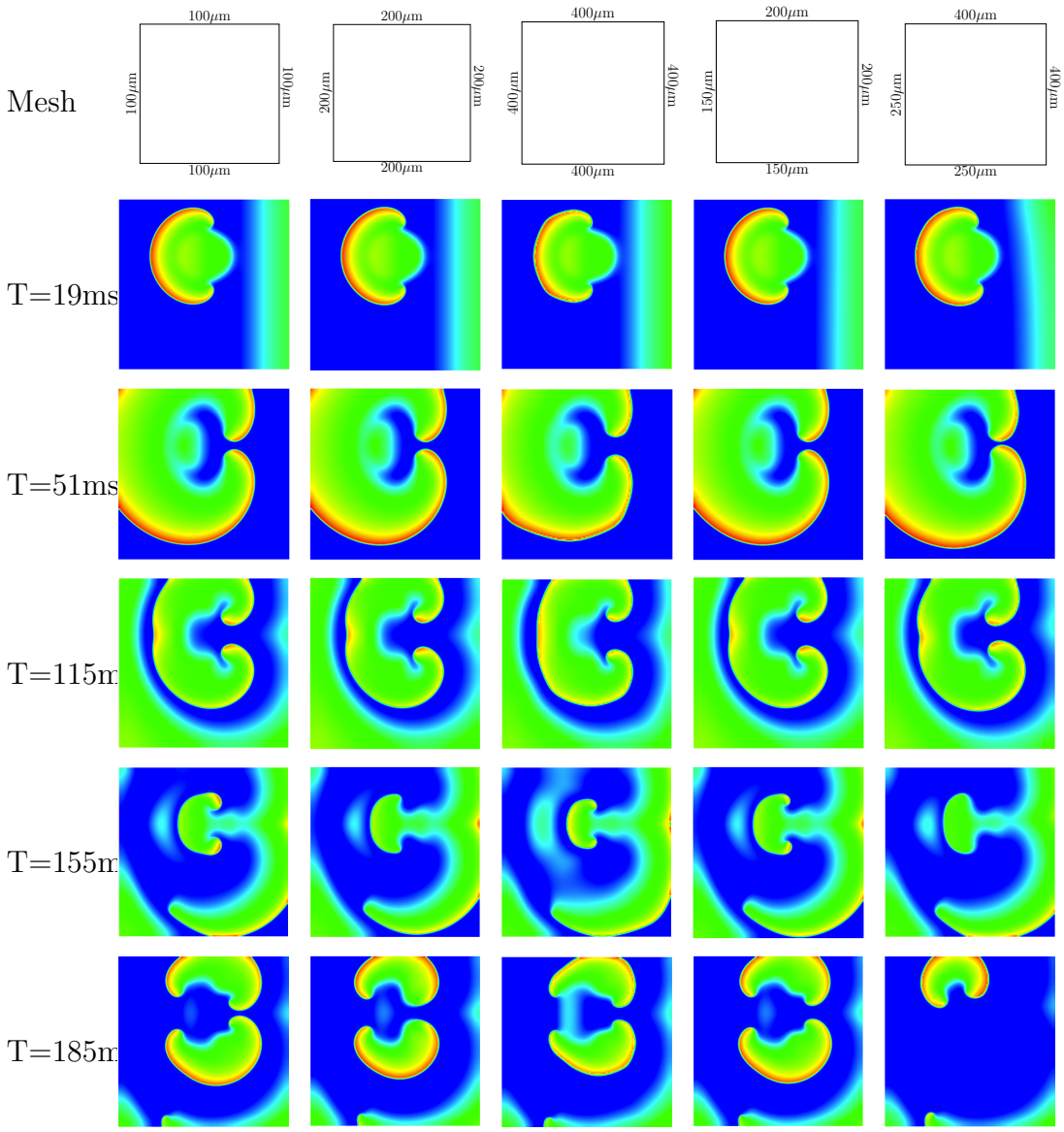

Figure 3.8: Comparison of spiral wave breakup between five different meshes. Time shown denotes the time since the application of S2 stimulus. The finer nonuniform mesh shows minimal variation in the wavefront compared to the coarser nonuniform mesh. The uniform 400μm (Column 4)and the nonuniform mesh 138μm $\leq \Delta x \leq$ 496μm (Column 6) shows physiologically unacceptable results.

CHAPTER 4

Whole heart cardiac electrophysiology– simulation methods and validation criteria

While simplified bar/slab geometries with uniaxial conduction are appropriate for systematic convergence studies, more physiologically relevant simulations commonly involve complex geometries and non-uniform conduction. Several modelers have approached the problem of modeling voltage evolution and the current state of art is in patient specific modeling[VAT12, SPC08, SCC12]. With the trend towards a patient specific model there is need for stipulating a set of validation criterion which needs to be satisfied by any generic model both from a numerical and physiological standpoint before it can be fine tuned to be patient generic.

In this chapter we describe a unified 3D reconstruction and geometric modeling framework that integrates the various image and geometry processing methods that are needed to model cardiac conduction. We first describe extraction of geometry from DT-MRI. Secondly we provide a brief description of the tensor interpolation schemes used to transfer the experimental diffusion tensor data onto the numerical model. We discuss modeling of the Purkinje conduction system and the Purkinje Muscle Junction (PMJ). Finally we describe the numerical computation of the ECG from the monodomain equations. We are especially concerned here with how *"any"* cardiac model is to be validated. We develop a series of criteria that any model of cardiac electrophysiology should meet, including specific requirements on the ECG and time-activation plots.

4.1 Rabbit Bi-Ventricular Model Construction

DT-MRI was used to acquire anatomical and microstructural images from an ex vivo, healthy, female New Zealand White rabbit heart. The heart was excised, fixed in formalin, and imaged with a 7T Bruker Biospin MRI system using a 150 mm volume coil and a 3D RARE diffusion weighted pulse sequence (24 non-collinear diffusion gradient directions, 6 null directions, TR/TE=500/30 ms, b-value=1000 s/mm^2, bandwidth=100 Hz/pixel, two-fold RARE acceleration, $0.5 \times 0.5 \times 0.75$ mm resolution).

DT-MRI provides detailed images of the cardiac anatomy and simultaneously provides quantitative microstructural information by estimating the local self-diffusion tensor ($\mathbf{D}_{\mathrm{DT}}$) of water within each image voxel. Importantly, an eigen-system decomposition of ($\mathbf{D}_{\mathrm{DT}}$) provides direct information about the local three-dimensional myofiber orientation, which is $\mathbf{e}_1$, the primary eigenvector of $\mathbf{D}_{\mathrm{DT}}$, and the orientation of myolaminae , which is given by $\mathbf{e}_3$, the tertiary eigenvector of $\mathbf{D}_{\mathrm{DT}}$, throughout the heart [SHW98, KNI11] .

An iso-contouring technique was applied to the segmented DT-MRI to generate a volume encompassing the right and left ventricular mass. A marching cubes algorithm was used to generate a polygonal mesh from the isosurface. This mesh is was cleaned using a windowed sinc filter [TZG96]. The effect is to "relax" the mesh, making the cells better shaped and the vertices more evenly distributed. All these operations were performed using VTK [SML].

4.2 Tensor Interpolation

In DT-MRI the data are acquired at lattice points within a three-dimensional imaging volume, but computational models of electrophysiology require closely spaced nodes that do not necessarily will not generally lie at lattice points. There-

fore, tensor field interpolation is a requirement. The diffusion tensor at each computational node was trilinearly interpolated using the DT-MRI data acquired at lattice points. We used a Linear Invariant tensor interpolation method [GWK12], which linearly interpolates components of tensor shape to introduce the least microstructural bias at low computational cost. There exist, however, many methods to interpolate tensors including, but not limited to nearest neighbor, Euclidean, log-Euclidean [AFP06], geodesic-loxodrome [KEN07], and linear-invariant tensor interpolation. The advantage of geodesic-loxodrome and linear-invariant tensor interpolation is the monotonic and linear interpolation, respectively, of the orthogonal tensor invariants (magnitude of isotropy, magnitude of anisotropy, and mode of anisotropy), which are intuitively related to salient microstructural features of the tissue[16]. The other tensor interpolation methods introduce microstructural bias, especially to the shape of the interpolated tensors [GWK12]. Currently, geodesic-loxodrome and linear invariant tensor interpolation introduces the least microstructural bias for cardiac DT-MRI data. Linear invariant tensor interpolation is a faster approximation of geodesic-loxodrome tensor interpolation because it can be calculated analytically, rather than iteratively. The final smoothed surface geometry extracted from Paraview is was then matched to fiber orientations from DT-MRI as shown in Figure 4.1

In our model, only the orientation (directionality) information, the eigenvectors of the interpolated diffusion tensors, was incorporated into the current computational model, not their eigenvalues. This is because the DT-MRI is actually recording the diffusion of water molecules. While the directions of water diffusion will correspond with the directions of electrical propagation (ref here), there is no reason to think that the magnitudes of electrical current diffusion are related to the magnitudes of water diffusion. For the electrical current diffusion magnitudes, we used eigenvalues in the ratio $4 : 2 : 1$, with the magnitude scaled to reflect correct conduction velocities.

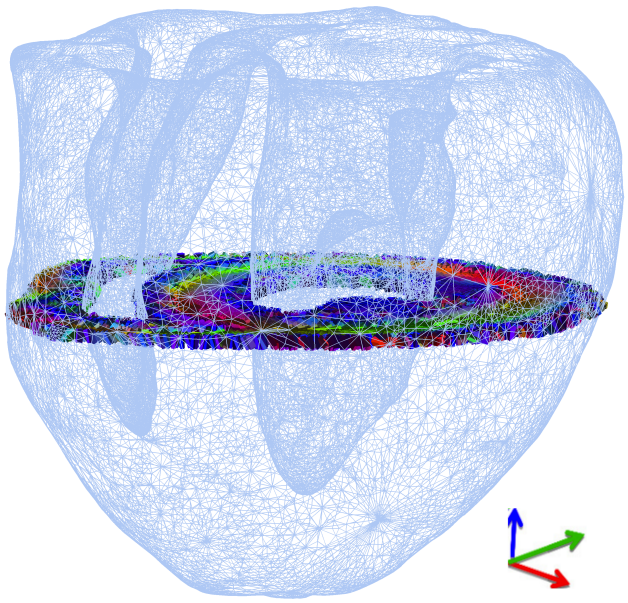

Figure 4.1: Short-axis view of the linear invariant interpolated tensor field of a slice in the rabbit ventricular model. The colors code the primary fiber direction, with red, green and blue showing the alignment of the fiber along the axes below.

4.3 Mesh Generation

Based on the earlier results on integration schemes the mesh size was chosen as 200μm. The bi-ventricular surface mesh obtained from segmentation of the DT-MRI was meshed with hexahedral elements of uniform size producing a stair stepped mesh. Hexahedral elements with bilinear interpolation where chosen over linear tetrahedral elements as voltage gradient is no more a constant in the element. The bi-ventricular model has 828532 elements and 901852 nodes. Figure 4.2 shows the meshed geometry and it also shows a magnified view of the basal-posterior ventricular wall seen.

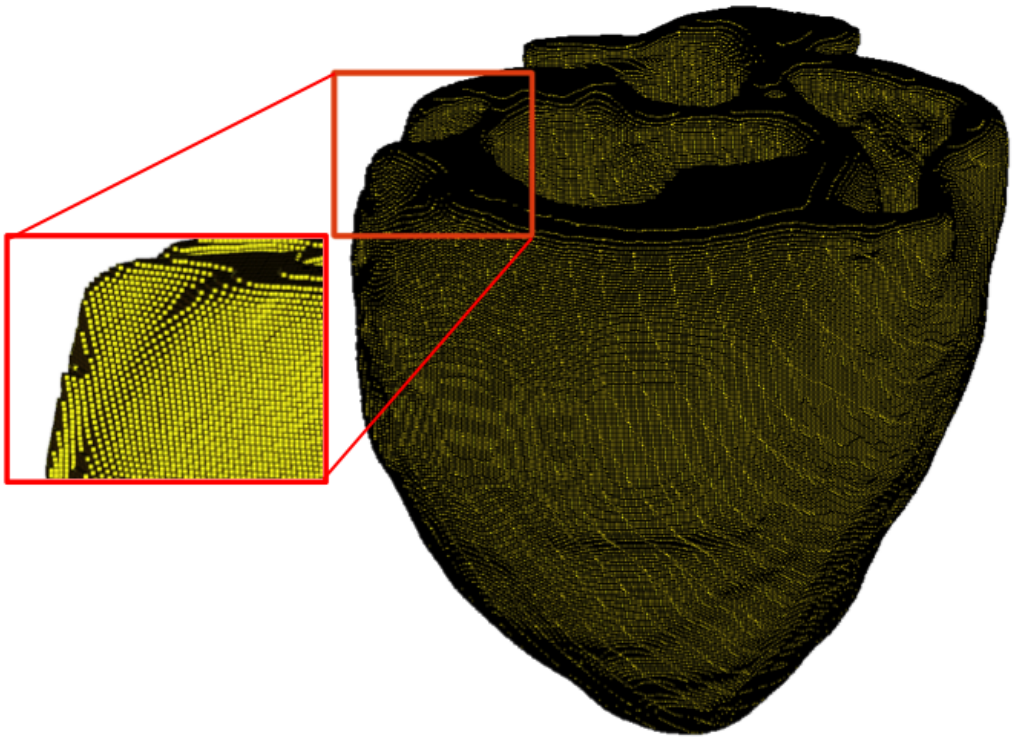

Figure 4.2: Rabbit ventricular model meshed with hexahedral elements with a zoomed in view of the basal-posterior ventricular wall.

4.4 Purkinje fiber and Purkinje muscle junction modeling

Purkinje fibers physiologically form a specialized conduction system, which lies just beneath the endocardial surface. This special conduction network is isolated from the muscle except at its endpoints where it is connected to the ventricular endocardial surface at special sites called Purkinje-Muscle Junctions (PMJ). Modeling this network and its interaction with the muscle is therefore crucial to build realistic ventricle models. The PMJ is bidirectional in the sense that it transmits current from the conduction system to the myocardium and also from the myocardium retrogradely back to the conduction system. Retrograde activation of the Purkinje system is necessary to model the hearts response to Bundle Branch Blocks (LBBB/RBBB), and is obviously necessary to model Purkinje-Muscle Reentry [ADL83, WKD89].

Ten Tusscher and Panfilov [TP08] reviewed previous Purkinje models. The reviewed HisPurkinje models differ in anatomical detail, spatial resolution and the approach used to model cardiac cellular excitation. With respect to anatomy, all models reviewed included a common His bundle and the left and right bundle branches. Also in most models the Purkinje network was not based on anatomical data but was described either as a few simple branches, or as a self-similar fractal tree or as a conductive tissue sheet containing insertions sites. To date, however, there remain challenges to incorporating accurate Purkinje networks into computational model, primarily because there are limited reports on imaging of the Purkinje network [KZR09, OKB10, COH12]. The Purkinje network was manually incorporated into our computational model as described in detail below, by assimilating the structure reported by Atkinson et al. [AIL11]. The guidelines found in [KZR09, OKB10, COH12, AIL11]provide critical input about the placement of the Purkinje fibers, however, the precise segment lengths, distribution, and PMJ density play an important role in the activation of the model and hence the com-

puted ECG. In general the conduction system has a single fiber emanating from the atrioventricular (AV) node, which then branches out. The geometry of the conduction system beyond this is not completely understood.

To model the Purkinje fibers we used 1D elements with Lagrangian interpolation. These elements exist in a 1D space, but they were modified to span a 3D space using direction cosines. For a regular 1D element the shape functions are $N_1 = 0.5(1-\xi), N_2 = 0.5(1+\xi)$, where ξ represents the isoparametric position of the point under consideration. While computing the matrices in the finite element equations we need the derivative of the shape function along global coordinate axis. To compute this we use the chain rule

$$\frac{\partial N(\xi)}{\partial X} = \frac{\partial N(\xi)}{\partial \xi}\frac{\partial \xi}{\partial X} = \frac{\partial N(\xi)}{\partial \xi}\mathbf{n}$$

where $\mathbf{n}$ is the unit vector at that location and its components are the direction cosines. Hence, the shape function derivatives are

$$\frac{\partial N(\xi)}{\partial X_i} = \frac{\partial N(\xi)}{\partial \xi}\cos(\theta_i)$$

In the 3D formulation of the 1D bar element the Jacobian is computed using the cross sectional area of the element and the length of the element. The cross section was assumed to be circular with a radius of 400μm.

To model the Purkinje muscle junction (PMJ) we proceed as follows. For a given terminal node in the purkinje cable we find all the nodes from the 3D myocardium which lie within a search radius r. From the terminal node 1D elements are constructed to each myocardium nodes which lies within the search radius. The area of each bar element was modified such that the electrical mass is the same. In other words the area of each bar element was computed as

$$A_{\mathrm{PMJ}} = \frac{\pi R^2}{N}$$

where R is the radius used to model Purkinje element and N is the number of nodes which lie in the search radius. Considering the terminal node form a pure

electrical view point from Ohm's law we have $I_{\text{in}} = I_{\text{PMJ}}$. From a physiological standpoint we need the same current to be transmitted through PMJ irrespective of the number of branches from the terminal node. Hence we need to ensure the electrical mass of the branches are same as the electrical mass of the terminal node. If $A = \pi R^2$ denotes the cross sectional area of any bar element we need

$$I_{\text{in}} A = \sum_{i=1}^{N} I^i_{\text{PMJ}} A^i_{\text{PMJ}}$$

Since the currents are the same we have $I^i_{\text{PMJ}} = I_{\text{in}}$. Assuming all the branches have the same area of cross section we get

$$I_{\text{in}} A = \sum_{i=1}^{N} I_{\text{in}} A_{\text{PMJ}} = N I_{\text{in}} A_{\text{PMJ}} \quad I_{\text{in}} \neq 0$$

$$A = N A_{\text{PMJ}} \Rightarrow A_{\text{PMJ}} = \frac{A}{N}$$

This yields the same value for area which we had assumed to start off with. While computing the shape function derivatives of the 1D element in 3D we used the direction cosines. Also the length of each connecting branch in PMJ is different. Physiologically we want all the branches to active the tissue at the same time. Hence while constructing these elements a fixed value for the length of the branches are assumed. The assumed values if 100μm. To eliminate the variance in the direction cosines all the branches are assigned the same direction cosine value. The value of direction cosines chosen is the value of the direction cosine of the 1D element connected to the terminal node. Physiologically we would expect the PMJ's to spread in the direction of the last fiber. Hence this is an acceptable assumption.

The interpolation of voltage within the constraint element is similar to the interpolation used for regular finite elements where position and voltage are interpolated among nodal values using piecewise polynomial shape functions. Hence, this constraint can be implemented as a regular element without further consideration. In our model, we used a search radius of 400μm. The shape functions

in 1D form were used to calculate the capacitance matrix and the shape function derivatives were calculated using directional cosines and were used in Equation 3.8 to compute the conductance matrix.

Activation was initiated with a stimulus of $50,000\mu A/cc$ applied at the AV node for 5ms. To model the Purkinje fiber we use the Rabbit Purkinje cell model developed by Bordas et al [BGL11]. For the Purkinje fiber we set $\mathbf{D} = 0.0032$ cm^2/ms. The first stimulus was applied at the beginning of the simulation and the second was applied after 400ms.

4.5 Ventricular Cell Modeling and APD Gradients

The duration and morphology of the T wave of the ECG is determined by the sequence of repolarization in the heart. This sequence depends largely on the action potential duration (APD) gradients present in both the transmural and apicobasal directions. These gradients arise from the heterogeneity of repolarizing currents within the heart, in particular the transient outward potassium current, Ito, and the slow component of the delayed rectifier potassium current, I_{ks}. To incorporate these characteristics in our model, we divided the ventricle into transmural regions (endocardium, midmyocardium, or "M" cell, and epicardium), as well as apicobasal regions (apex, center, and base). This resulted in nine distinct regions. To each, we assigned a different variation of the UCLA ventricular cell model by altering the maximum conductance values for the I_{to} andI_{ks}. These conductances (G_{to} and G_{ks} respectively) were defined in each region so as to produce the APD and current density gradients given in the literature. The values used are shown in Table 4.1

Transmurally, G_{to} values were varied to match the data of Fedida et al. [FG91], who found the Ito current density of endocardial cells to be 15% less than that of epicardial cells. G_{ks} values were then adjusted to attain the APD gradient found

APDs (ms)			
	Apex	Center	Base
Epi	168	177	186
M	195	205	216
Endo	189	199	209
G_{to} (mS/μF)			
	Apex	Center	Base
Epi	0.11	0.11	0.11
M	0.11	0.11	0.11
Endo	0.094	0.094	0.094
G_{ks} (mS/μF)			
	Apex	Center	Base
Epi	0.61	0.45	0.32
M	0.24	0.17	0.11
Endo	0.31	0.22	0.16

Table 4.1: APD and conductance values

by Idriss et al., [IW04] who reported the APD of endocardial cells and M cells to be 10% and 12% greater, respectively, than those of epicardial cells Mantravadi et al. reported APDs in the base to be 10% greater than in the apex [MGL07]. Because no data has shown I_{to} to vary apicobasally, we only varied G_{ks} to achieve this.

4.6 Purkinje Cell Models

The Purkinje fibers are specialized myocytes that are fast conducting, in part, as a result of a high upstroke velocity during phase 0 of the action potential. They have other distinct action potential characteristics: a prominent early rapid repolarization (phase 1), a negative plateau potential (phase 2), an increased action potential duration, and spontaneous diastolic depolarization (phase 4). They also play a role in the generation and maintenance of arrhythmias because they can support reentry, sustain ventricular fibrillation, are susceptible to arrhythmogenic early and delayed after-depolarization, are linked to torsade de pointes associated with long QT syndrome and play a role in arrhythmias after electric shock defibrillation. A comparison of the APD between the purkinje cell model and the UCLA cell model is shown in Figure 4.3

The diffusion value $\mathbf{D}$ was set as 0.0032cm/ms^2 which is different from the value specified by Bordas et al. This value was modified to obtain physiologically acceptable wave speeds $[0.8 - 2.0\text{ms}^{-1}]$.

4.7 Tensor Interpolation

To quantitatively evaluate the differences between interpolation schemes, we computed the Root Mean Squared Deviation (RMSD) between two interpolation

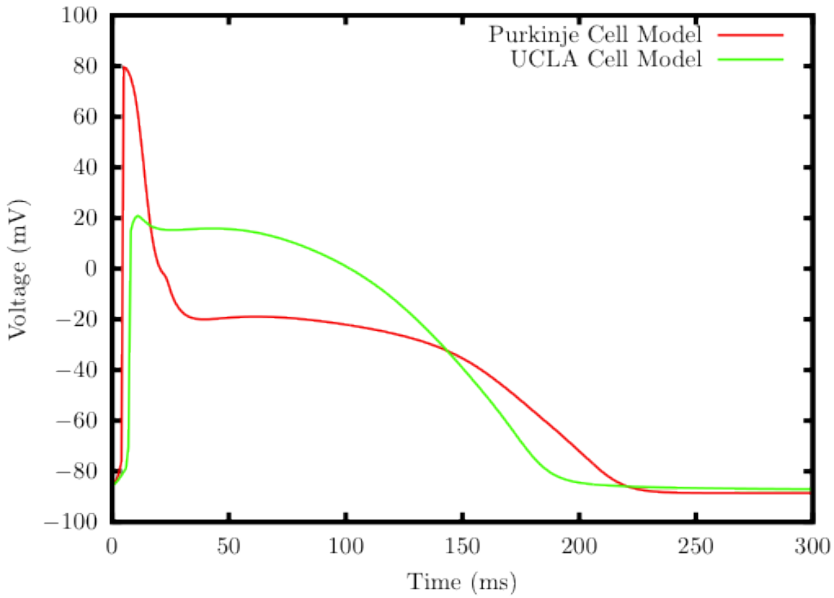

Figure 4.3: Action Potential(AP) plots of UCLA and Purkinje cell models

schemes J and K as

$$RMSD_{\text{J-K}} = \frac{\sqrt{\sum_{i=1}^{N}(V_{J,i} - V_{K,i})^2}}{N}$$

where N, is the number of nodes in the model, V_J is the voltage results from the model using interpolation scheme J and V_K is the voltage that results from the model using interpolation scheme K. The maximum difference in RMSD between Geolox and Log Euclidean was 0.032mV, Geolox and Euclidean was 0.032mV, and Geolox and Nearest Neighbor was 0.05mV. The comparison of $RMSD$ between different interpolation schemes is shown in Figure 4.4.

Also we find that there is minimal difference in activation pattern between different interpolation schemes as shown in Figure 4.5. This is because there are minimal differences in the primary eigenvector orientation between different tensor interpolation methods [GWK12]. (If other tensor attributes (fractional anisotropy, tertiary eigenvector etc.) were used in the computational model, then further evaluation would be needed.) From the minimal difference in results between in the interpolation schemes and also based on inferences from [GWK12],

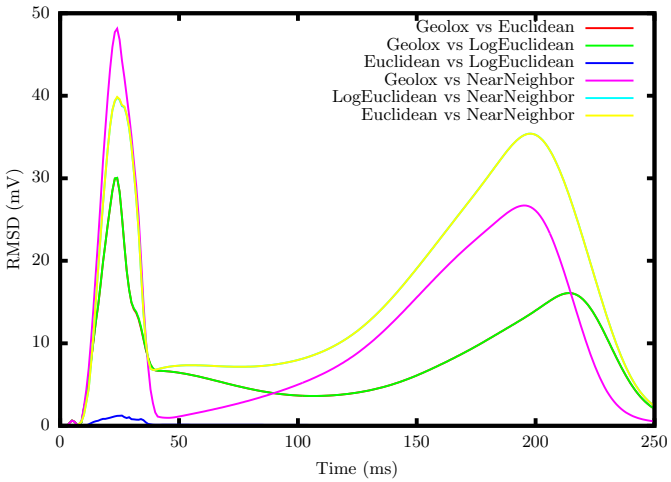

Figure 4.4: *RMSD* error comparison between different tensor interpolation schemes

Geodesic loxodrome interpolation was used for all further simulations. The resulting interpolation yielded a tensor field defined at the points of integration.

4.8 Purkinje Structure Comparison

In order to evaluate the importance of geometry, we considered three different models.

- **Low PMJ Model:** This model has 55 PMJs. The branch in the LV further branches out in the mid septal region. One branch covers the LV posterior fascicle and branches out to the LV free wall. The other branch embraces the LV anterior fascicle, however does not extend to the LV free wall. The branch in the RV, branches out close to the mid septal region and similar to the LV, one branch embraces the LV posterior fascicle reaching the RV free wall and the other branch unlike in the LV, embraces the RV anterior fascicle. There is large region of endocardial surface, which is not connected to PMJs, and hence cell-to-cell diffusion would be the main mode for voltage propagation.

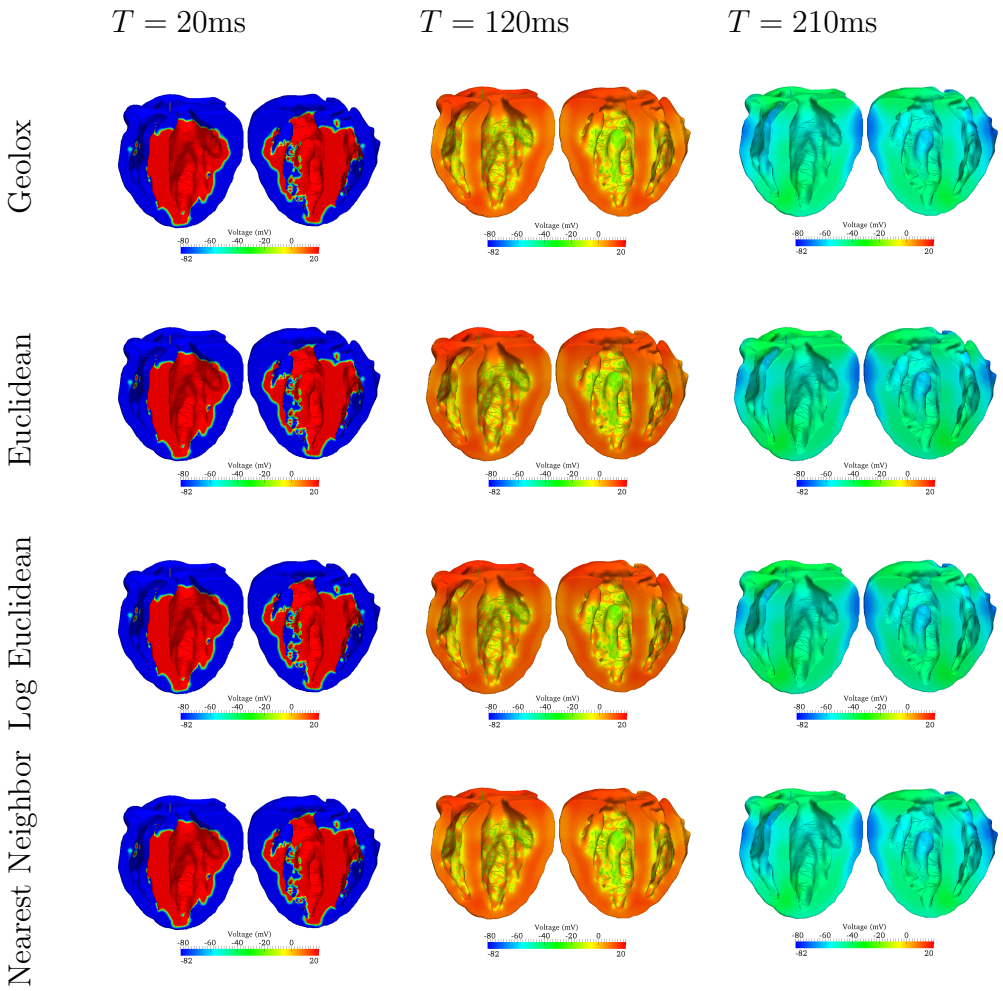

Figure 4.5: Voltage contour comparison between different interpolation schemes at different times - 20ms, 120ms and 210ms.

- **Medium PMJ Model:** This model has 155 PMJs. The branch entering the LV has more branches than in the low PMJ model. There are two branches that embrace the LV posterior fascicle running till the LV free wall and similarly two branches covering the LV anterior fascicle running till the free wall. Also there is one branch that extends towards the apex. In the RV similarly we have two branches embracing the anterior and posterior fascicle. Similar to LV there is a branch, which reaches towards the apex of RV. Here we have more PMJs on the endocardial surface compared to the

Low PMJ model, however there are still regions where cell-to-cell diffusion would be the main mode for voltage propagation.

- **High PMJ Model:** This model has 515 PMJs and was generated by adding PMJs to the Medium PMJ Model. To reduce the dependence on cell-to-cell diffusion for voltage propagation more branches were added in the LV and RV endocardial surfaces. These branches embrace the anterior and posterior fascicle similar to the branches in the medium PMJ model. Hence, the core geometry is very similar to the medium PMJ model. However the dependence on cell-to-cell diffusion is reduced further due to the high number of PMJs.

The three different models are shown in Figure 4.6. We also considered a model without a Purkinje structure, in which the heart was activated by simultaneous command activation of the endocardial surface.

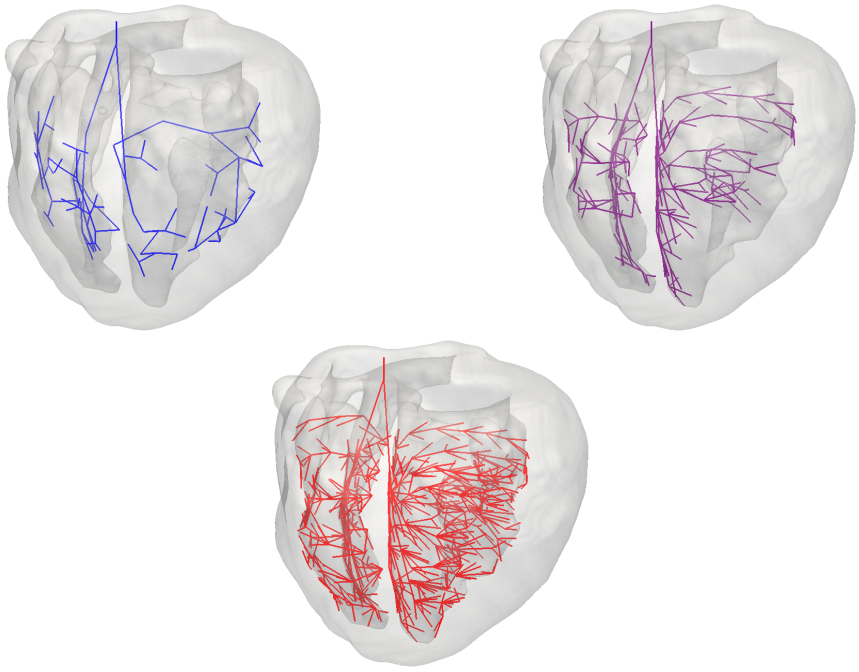

Figure 4.6: Low, Medium and High PMJ model used to evaluate the influence of Purkinje conduction system in obtaining the correct activation pattern

4.9 Activation of the Heart

The voltage evolution history for the four different models were computed. Following the pioneering work of Durrer [29], we constructed activation maps showing the progress with time of the wavefront of activation. At each node in the domain Ω, we calculated the time T (from the activation of the AV node) to cross a critical voltage $V_{\text{Threshold}}$:

$$T = \begin{cases} t_n + \frac{V_{\text{threshold}} - V^n(x)}{V^{n+1}(x) - V^n(x)} & \text{if } V^{n+1}(x) > V_{\text{Threshold}} \geq V^n(x) \\ T_{\max} & \text{otherwise} \end{cases} \tag{4.1}$$

where $V^{n+1}(x)$ denotes the nodal voltage at time step t_{n+1}, $V^n(x)$ denotes the nodal voltage at time step t_n, $\Delta t = t_{n+1} t_n$. $V_{\text{Threshold}}$ was chosen as ?30mV. This time at which the myocardium is depolarized and exceeds $V_{\text{Threshold}}$, is rendered to produce an activation map.

The cardiac activation sequence from these four models was computed and rendered as shown in Figure 4.7. We infer that the low PMJ model does not produce a synchronous activation. Most of the regions in the LV get activated much later and also we see that the basal region has not been activated even after 45 ms since the stimulus was applied to the AV node. The medium and high PMJ models show synchronous activation of the LV and RV endocardium. The septal activation also occurs earlier in the medium and high PMJ model compared to the low PMJ model. In the medium PMJ model there is still some region in the basal region which has not been activated even after 45ms. The model with instantaneous activation shows synchronous activation of LV and RV due to the inherent nature of stimulus applied. Also the entire myocardium is depolarized by 30ms.

Experimental recording from Bordas et al [BGL11], show initial activation happening in the mid-septal region and also a synchronous activation of LV and RV. The medium and high PMJ model produce results that are similar to the

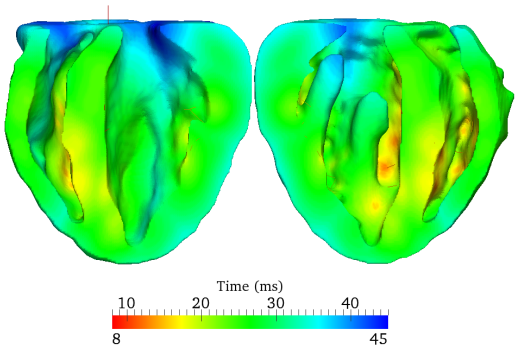

(a) Low PMJ Model

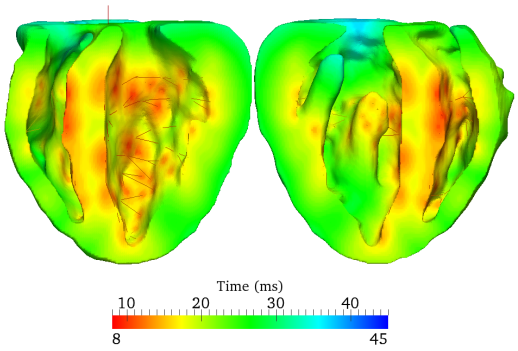

(b) Medium PMJ Model

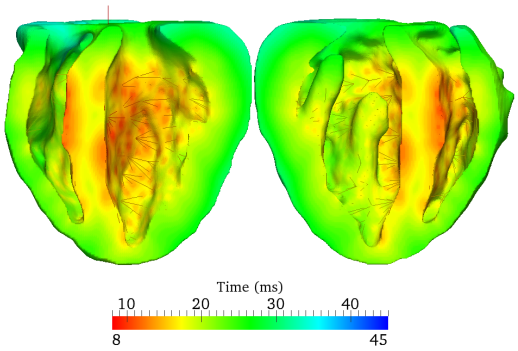

(c) High PMJ Model

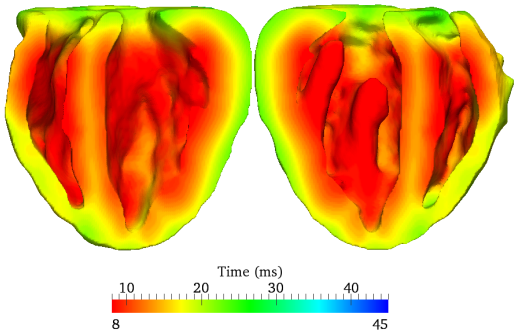

(d) Synchronous endocardium activationl

Figure 4.7: Activation sequence comparison between different models.

results reported in Bordas et al. The low PMJ model due to its dependence on cell-to-cell diffusion exhibits unacceptable activation patterns. The fourth model with instantaneous activation of LV and RV endocardial surfaces does not show early activation in the septal region.

4.10 Modeling of the ECG

From a numerical model, the ECG output can be represented as [PH97]

$$\text{ECG} = \int_{\Omega} \nabla V(\mathbf{x}, t) \cdot \left(\mathbf{D}(\mathbf{x}) \cdot \nabla \left(\frac{1}{R} \right) \right) d\Omega \tag{4.2}$$

where R denotes the distance between any point in the domain Ω to the lead position and $\mathbf{D}$ is the diffusion tensor, and $V(\mathbf{x}, t)$ is the transmembrane voltage at $\mathbf{x} \in \Omega$ at time t. All the elements defining the ventricles, Purkinje fibers and the PMJs are included in the domain Ω.

4.10.1 ECG Lead placement.

We calculated ECGs for the six precordial leads V1 to V6 and positioned in specific positions on the chest wall. The six leads were placed according to the following guidelines: V1 - right sternal border; V2 - left sternal border; V3 - midway between V2 and V4; V4 - left midclavicular line; V5 - level with V4, left anterior axillary line; and V6 - level with V4, left mid axillary line. The placement of the lead with reference to a rabbit model is shown in Figure 4.8.

4.11 Computed Electrocardiogram

Using the voltage output from the simulation and using Equation 4.2 the ECG at lead positions denoted in Figure 4.8 were evaluated. The computed ECG for the low PMJ model is shown in Figure 4.9, medium in Figure 4.10, high PMJ model

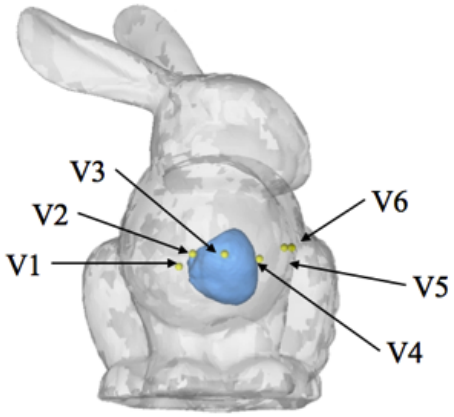

Figure 4.8: Six bipolar lead placed in the rabbit ventricular model. The model of the rabbit (Stanford Computer Graphics Laboratory) is not a part of the computational domain. It is shown in the image to orient the view of the leads.

in Figure 4.11 and instantaneous activation model in Figure 4.12

The computed ECG was evaluated for

1. QRS duration; The QRS width that corresponds the depolarization of ventricles happens fast and hence results in shorter QRS width.

2. QRS morphology; Also a typical patient ECG does not show any slurring or fractionations in the QRS segment,

3. R wave progression; In a normal ECG we expect to see a pattern of a change from the S wave being prominent to the R wave being prominent. So looking at V1 we expect a mostly downward deflecting axis and in V6 we expect an upward inflecting QRS axis. We also expect the RS complex in V1 to slowly transition from negative to positive in V6. This transition is called the R wave progression [ZK82, SVU55, ZK79] and

4. T wave morphology and progression.

From the 6 lead outputs the average width of the QRS segment for the 4 cases were computed as (a) Low PMJ 32.83ms, (b) Medium PMJ 26.83ms, (c) High PMJ

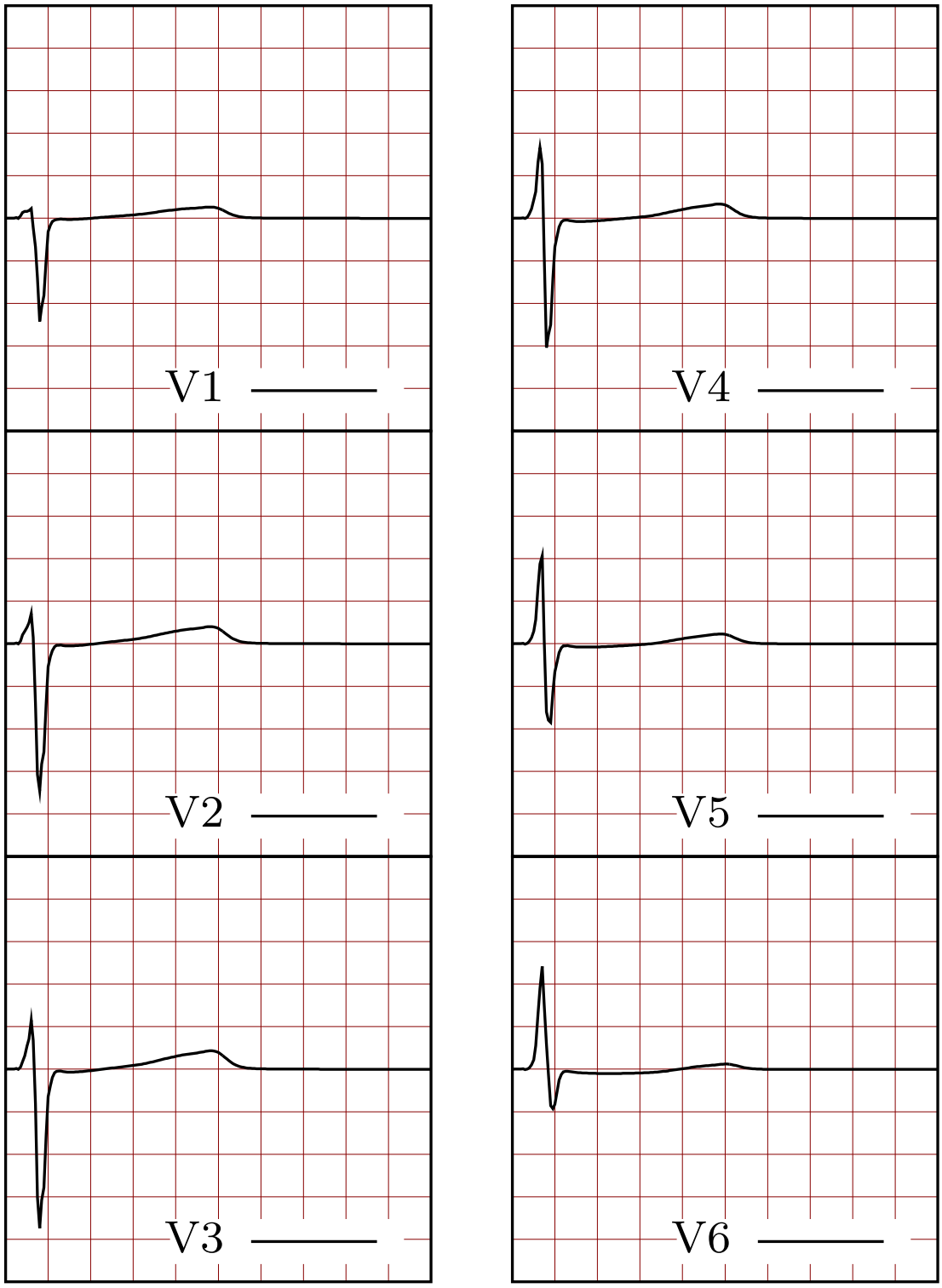

Figure 4.9: Computed 6 lead ECG from the low PMJ model. The ECG shows slurring

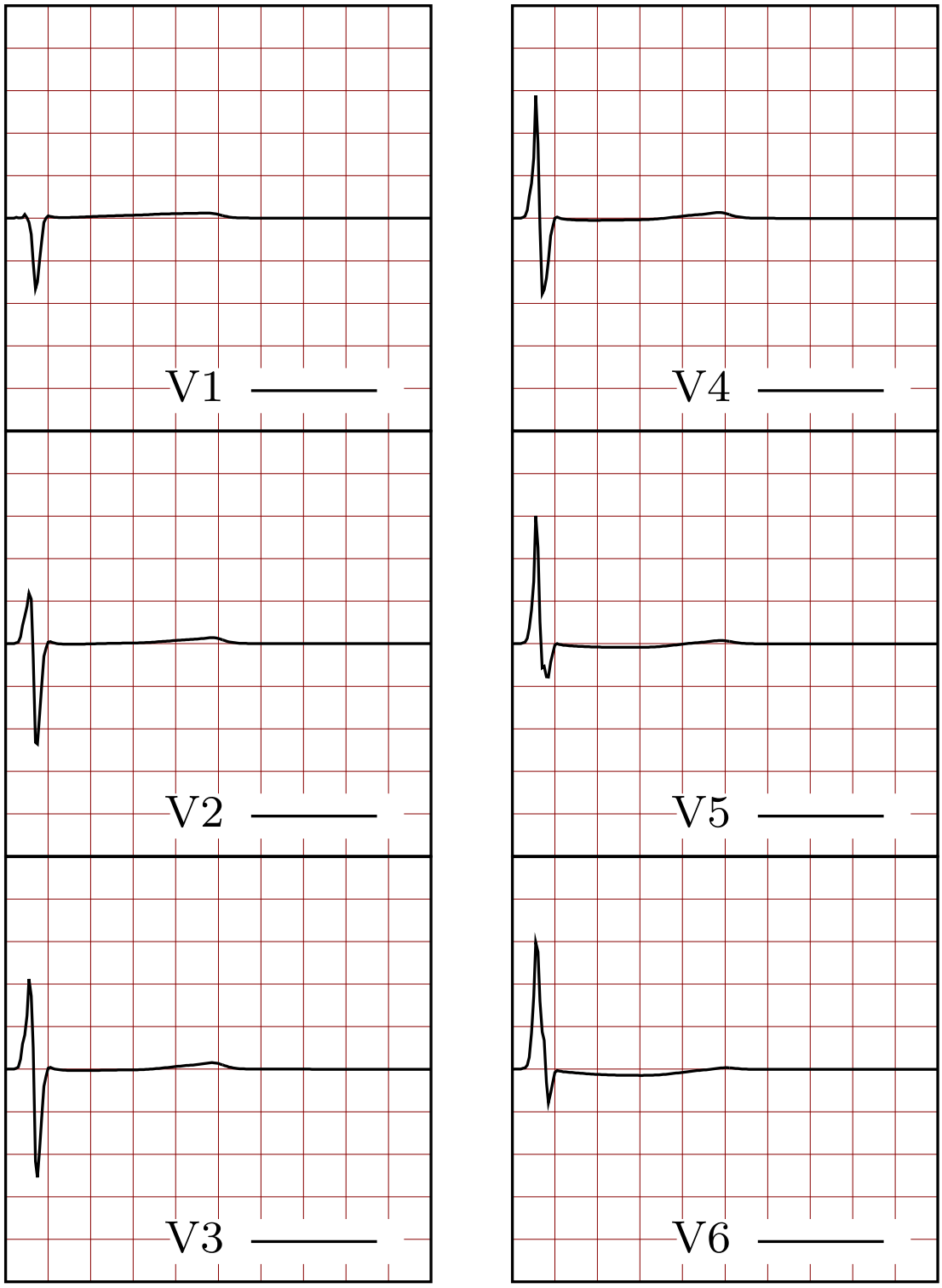

Figure 4.10: Computed 6 lead ECG from the medium PMJ model. The ECG shows fractionations

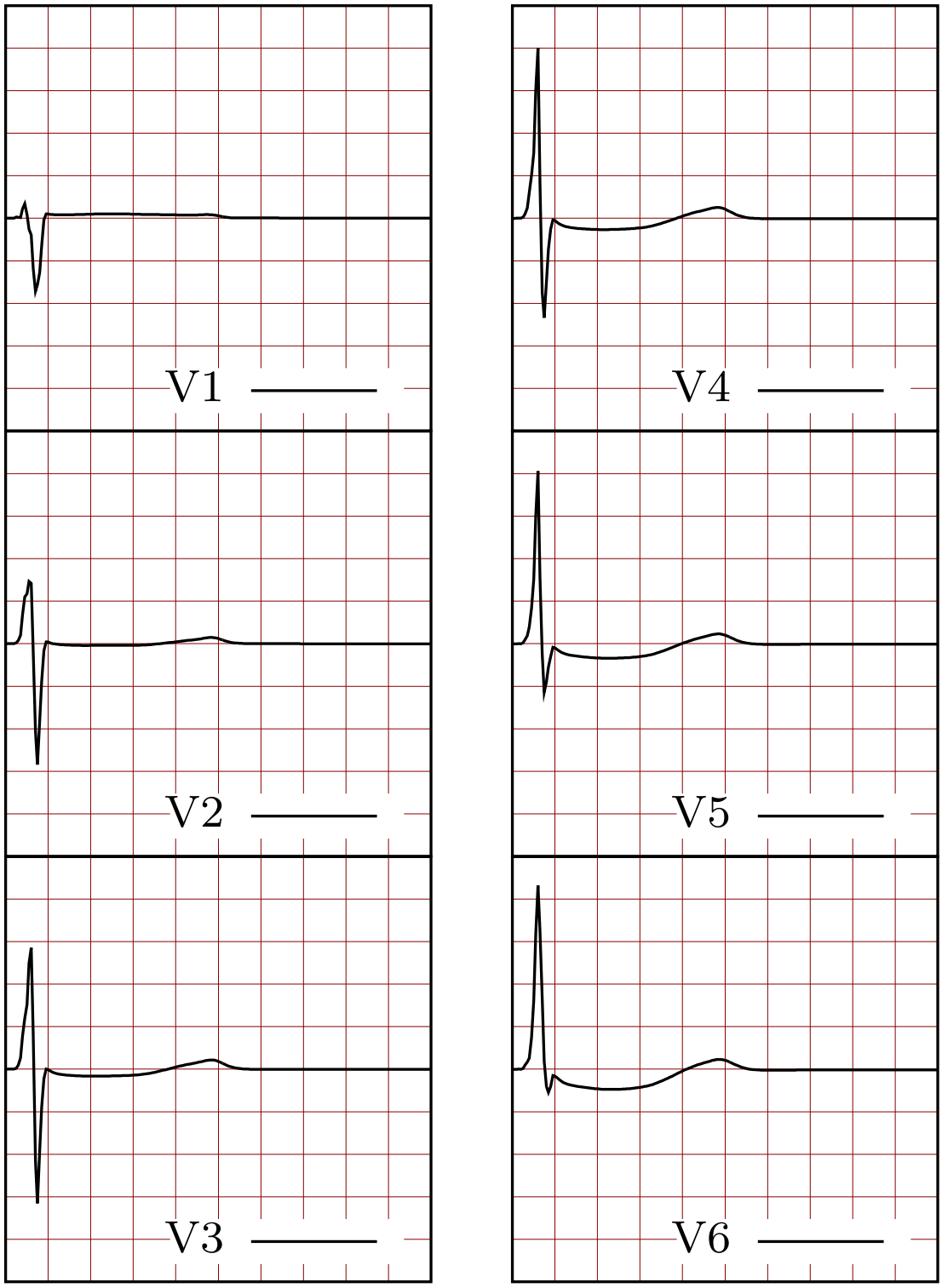

Figure 4.11: Computed 6 lead ECG from the high PMJ model. This reproduces the best ECG.

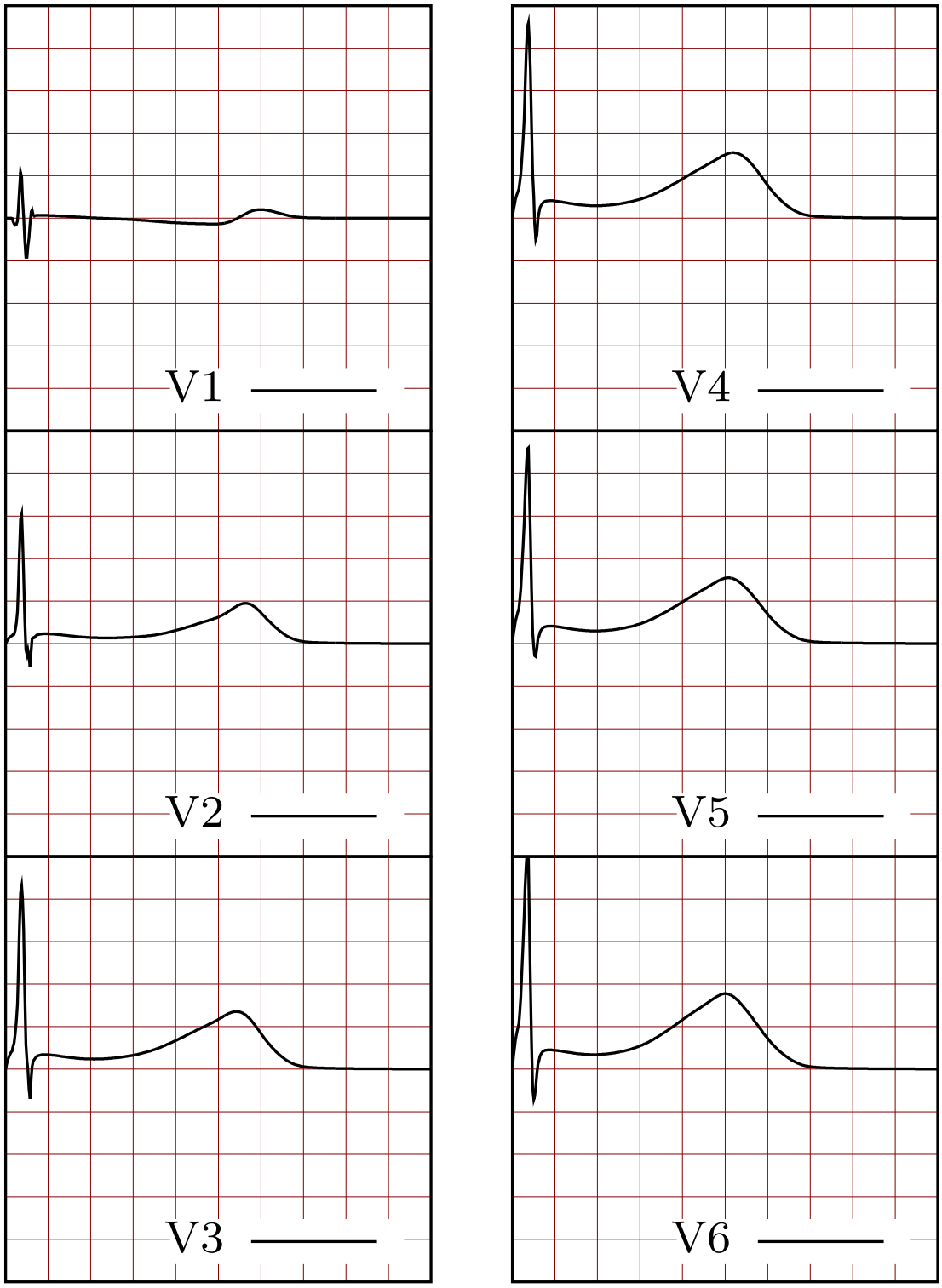

Figure 4.12: Computed 6 lead ECG from the instanenous endocardium activation model. This shows no R-wave progression

22.17ms and (d) Instantaneous activation 20.34ms. Since the low PMJ model relies on cell-to-cell conduction for voltage propagation it shows the highest QRS width. Following the same analogy the high PMJ model has the least QRS width. In the case of instantaneous activation we find the least QRS width.

The overlay of lead V5 from the low and high PMJ model is shown in Figure 4.13a and overlay of V5 for the same models is shown in Figure 4.13b

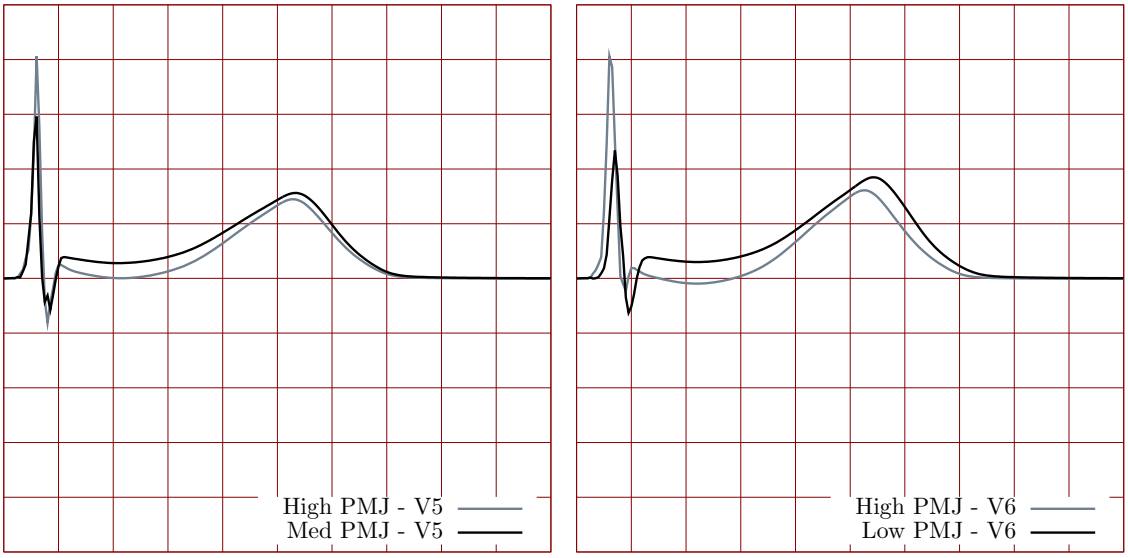

(a) Lead V5 comparison between low and high PMJ model

(b) Lead V6 comparison between low and high PMJ model

Figure 4.13: (a) Comparison of V6 lead from Low PMJ and High PMJ Model. Low PMJ shows presence of "S" wave. (b) V5 comparison between Medium and High PMJ model. Medium PMJ model shows fractionations

In the low PMJ model we find presence of S wave in V6, which, is not seen in the High PMJ model (Figure 4.13b. Also the low PMJ model shows slight slurring in QR segment for V1, RS segment for V2, V4 and V5. In the V5 lead of the medium PMJ model we see fractionations, which, is absent in the High PMJ Model (Figure 4.13a). Also medium PMJ model shows fractionations in lead V2. We see slurring in the RS segment of V4 and V6. The high PMJ model shows

the least slurring in QR segment for leads V1 and V2. We do not observe any fractionations in the model.

The R wave transition is absent in the instantaneous activation model. It gets better from the low to the high PMJ model, with the best transition seen in the high PMJ model. better in the medium and high PMJ model compared to the low PMJ model.

We also see an increased in the height of the T wave as go from the leads V1-V6. The addition of the heterogeneity in the APD via the cell model ensures the repolarization wave is opposite to the repolarization wave. Hence all the four models produce upright T waves which is consistent with lab results.

The low PMJ model and the high PMJ model produced ECG that had the right morphology, but the low PMJ model had a wider QRS. The medium PMJ model had fractionations in some leads. The low and high PMJ mode displayed some slurring. We then looked at the time activation plots. The low PMJ model relied on cell-to-cell diffusion for voltage progression. Hence this resulted in an asynchronous activation of the LV and RV regions. The medium and high PMJ model showed synchronous activation of the LV and RV. Looking at ECG alone is not enough to decide on the geometric structure of the conduction system. The geometry of the conduction system needs to be decided based on the time activation pattern also. Though the instantaneous activation model produces a good activation plot the ECG produces does not satisfy the criterion set forth. Hence to produce a validated ECG the numerical model must contain a dense enough Purkinje anatomically right conduction system.

4.12 Inferences

In this chapter the requirements for producing a validated numerical model of a finite-element solution of the reaction- diffusion equations of cardiac electrophysi-

ology are laid out. A typical numerical construction consists of three components. We define set of validation criterion that needs to be met at each level to produce physiologically acceptable results.

Imaging involves generating the computer model, which is further discretized into finite elements and used for simulation. Also the tensor field obtained from MRI slices gets interpolated to the discretized field. We compared different tensor interpolation schemes, which showed minimal difference in the voltage evolution.

While creating the finite element mesh caution needs to be exercised while using automated meshing algorithms that tend to create meshes with varying sizes. Use of larger element size leads to deterioration of wave speed and lead to numerically induced unphysiological results. As long as the mesh has largest element size less than 200μm with the preferential matrix lumping scheme we do not introduce artificial wave speed up.

To obtain the correct activation sequence we need to (i) have appropriate cell models for myocardium and cell model for purkinje conduction system, (ii) subdivide the model into regions to include action potential dispersion, (iii) large enough purkinje end terminals which encompass the endocardial surface in accordance to physiology. We report only three different cases of the 100 cases that we considered which generating the conduction system geometry. Also looking at the ECG alone is not enough to verify the conduction system geometry. The results have to be evaluated along with time activation plots to determine accuracy. The right conduction geometry is critical in providing the correct "R wave progression from leads V1 to V6. Modeling the action potential dispersion correctly produces upright T waves and along with increasing height from leads V1 to V6.

The development of the validation criteria for models simulating cardiac tissue electrophysiology is an important step towards producing patient specific modeling and the reproducibility of simulation results. This is essential to provide confidence in the utilization of cardiac models to answer fundamental clinical

questions.

CHAPTER 5

Cardiac excitation mechanics coupling

The excitation-contraction coupling takes place during heart contraction [Lab82]. As durations of action potential and contraction of the heart are of same order of magnitude, this coupling is expected to be especially important. From a physiological point of view, the mechanism excitation induces contraction is largely understood, by the intermediate of calcium released from the sarcoplasmic reticulum of cardiac cells and the actin-myosin activation leading to cell contraction. To understand this essential biological function there is a need of having realistic mathematical models which potentially allows insight into areas such as neurophysiology, locomotion and motor control. For models to be useful in such studies, they must capture sufficient detail without being overly complex.

For an invivo LV, it is well known that the contraction of obliquely oriented fibers induces a torsion about its long axis, which was first observed in open chest animal hearts by Sir William Harvey in 1628 and confirmed by instrumented experiments with dogs as recently as the 1960s [BMS08, SFW08], but also in man ([GG09, NG09]). However, the role played by the LV torsional rotation with respect to LV ejection and filling was only recognized recently by application of speckle tacking echocardiography ([GCA10, HRL09]. Based on experimental observations, the time course of ventricular torsion is well documented and proceeds more or less as follows [TMK11]. With the onset of systole (stage 1), the apex and base exhibit a slight clockwise rotation (as viewed from the apex) that largely resolves by the end of the iso-volumic contraction phase. As the heart starts to

empty (stage 2), the apex begins to turn in a counterclockwise direction while the base rotates less slowly in the opposite direction. Throughout the remainder of the ejection phase (stage 3), the twist rate remains relatively constant as the apex and base continue to turn in oppo-site directions in a wringing motion, the net ventricular twist reaching $12 - 15^o$ in most cases. During diastole most of the torsion gained during systole is lost rapidly during isovolumic relaxation (stage 4), after which the heart gradually resumes its presystolic orientation as the ventricles expand and fill (stage 5). Although both physiological reason behind mechanical motion is understood , it is still not clear which parameters affect LV torsion. This is an important question as the model chosen has severe implications on the mechanical predictions.

5.1 Constitutive modeling

Muscles are organized bundles of multi-nuclei, long cells, called myofibers, whose mechanical characteristics depend on both the intrinsic properties of those fibers and their overall architecture. Almost all biological soft tissues are anisotropic, viscoelastic, inhomogeneous, nearly incompressible and undergo large deformations in vivo, both under normal physiological conditions and during injury [WMG96]. In the first biaxial test of excised passive myocardium, Demer & Yin [DY83] observed nonlinear viscoelastic properties of resting myocardium as anisotropic and pseudo-elastic. Therefore the myocardium is frequently modeled as a finite hyper elastic material i.e., we assume the existence of strain energy function (W).

Muscle contains connective tissue and cells and is surrounded by fluid-filled extracellular space. Also both these components primarily contain water. Hence they are typically assumed as incompressible. This has been established in experiments by Vossoughi et al. (1980), who subjected tissue specimens to various levels of hydrostatic stress. They recorded the associated volumetric strains and

concluded that the myocardial tissue is essentially incompressible.

Browsing physiological literature dealing with muscles, we find there are two of the following basic descriptions:

- A muscle is a force generator – emphasis is put on dynamics, that is, on forces;
- A muscle generates motion – emphasis is on kinematics, that is, on displacements.

Hill in 1938 [Hil38] performed experiments on tetanized skeletal muscle from frog sartorius. At first, a muscle bundle, clamped at one end, is electrically stimulated and mantained at fixed length L_o (isometric conditions) by the appropriate reaction force; eventually, a maximum force F_o is reached. At this tetanized state, the reaction force is suddenly decreased to a constant value $F \leq F_o$ (isotonic conditions): it follows that the muscle contracts. Based on the observation that electrical activity causes mechanical motion two formulation schemes have been proposed to include this effect.

5.1.1 Active stress formulation

Following the lines of emphasis on "dynamics" the change in resting length is modeled by the addition of an internal compressive force i.e., when cardiac muscle fibers are stimulated, they generate contractile forces [HMT98, NH00, ULM02]. This model is aimed at interpreting some experimental tests, and focuses on the relationships between the tension developed in a cardiac muscle and its physiological state, summarized by a coarse description of crossbridge kinetics. In particular, it focuses on the following mechanical experimental observations,

1. tension-length relation in resting and activated muscles,
2. time course of tension development under isometric conditions,

3. tension recovery under length step tests,

4. isotonic shortening at constant velocity (Hill experiments as benchmark) and

5. frequency response.

A key assumption is that the overall tension T sustained by a muscle be the sum of a passive component T_p, described by an appropriate elastic energy (W) based on biaxial test results, plus an active component T_a, assumed to depend on the strain and the level of activation

$$T = T_p(\text{strain}) + T_a(\text{strain, activation})$$

Most of the effort is spent on the characterization of a response function for T_a(strain, activation), based on physiological phenomena and capable of describing the aforementioned mechanical experiments.

From a modeling stand point at the macro scale of the tissue, an active stress tensor constitutively related to the tissue's electro-physiological activity is computed. The overall stress in the tissue is then recovered by adding to the active stress a passive stress, depending on the mechanical properties of the myocardium. The form of the active stress is similar to the second Piola Kirchoff stress $\bar{\boldsymbol{\sigma}}$. Hence typically the active stress is added and we get the total stress as

$$\bar{\boldsymbol{\sigma}} = \frac{1}{2}\left(\frac{\partial W}{\partial \mathbf{E}} + \frac{\partial W}{\partial \mathbf{E}^T}\right) - p\mathbf{C}^{-1} + \mathbf{T_a}(Ca^{2+})$$

where $\mathbf{E}$ is the Green-Lagrangian Strain tensor, $\mathbf{C} = \mathbf{F^T F}$ is the right Cauchy tensor, p is a pressure term which accounts for incompressibility.

5.1.2 Active strain formulation

Instead of adding an additional force to generate contraction another approach is change the reference configuration which then by the inherent change in deforma-

tion generates the internal force [NT07]

Consider a 1D muscle fiber as shown in Figure 5.1 in three different states, the apparent state, slack state and ground state. Visible length l is the length of a fiber that is actually observed, i.e., the current length. Ground length l_o is the reference length, typically associated with the stress-free configuration in the presence of activation. The slack state length l_s is the state that would be stress free (i.e., zero external applied force) and in the absence of activation. If the muscle were unloaded and activated, it would stretch from the initial ground state to the ground state. Therefore loading can be thought of as a two-stage process: first activation transforms the slack state to the ground state, and then the loading stretches the ground state to the visible/current state.

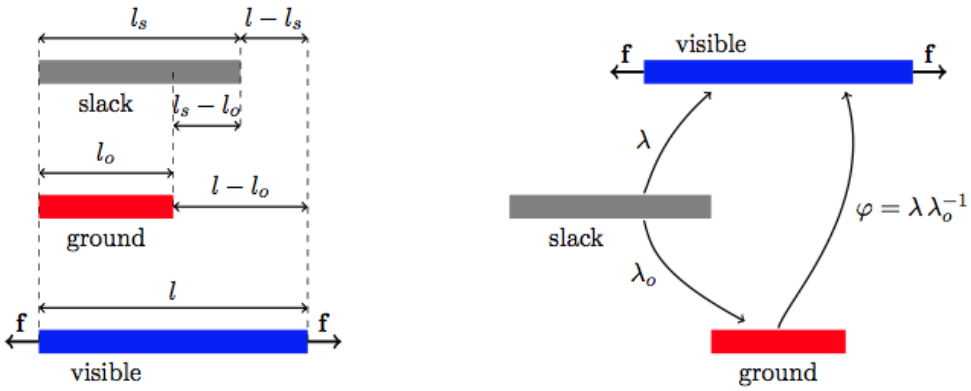

Figure 5.1: Schematic of the muscle model. The load f sustained during activation depends on the dfference between the visible and the ground length. Image at right shows the role of the three stretch measures.

We can introduce three stretch measures: two compares the ground and visible lengths with respect to the slack one; the last one compares the actual and the

ground length

$$\lambda = \frac{l}{l_s} \text{ visible stretch}$$
$$\lambda_o = \frac{l_o}{l_s} \text{ active stretch}$$
$$\phi = \frac{l}{l_o} = \frac{l}{l_s}\frac{l_s}{l_o} = \lambda\lambda_o^{-1} \text{ total stretch}$$

In the case of 3D the same analogy boils down to the multiplicative decomposition of the deformation gradient as shown in Figure 5.2. At the macroscopic scale, activation of the muscle fibres of the tissue is described by a variation in the rest length of the body elements, and that this variation is measured by a distortion field $\mathbf{F}^o$, to be known as the active deformation. Then, we call visible deformation $\mathbf{F}$ the gradient of the placement and $\mathbf{F}^e$ the elastic deformation body elements as the difference between the active and the visible deformations. In the sense of multiplicative composition we get

$$\mathbf{F}^e = \mathbf{F}\mathbf{F}^{o-1}$$

The active deformation part is typically described as a function of calcium con-

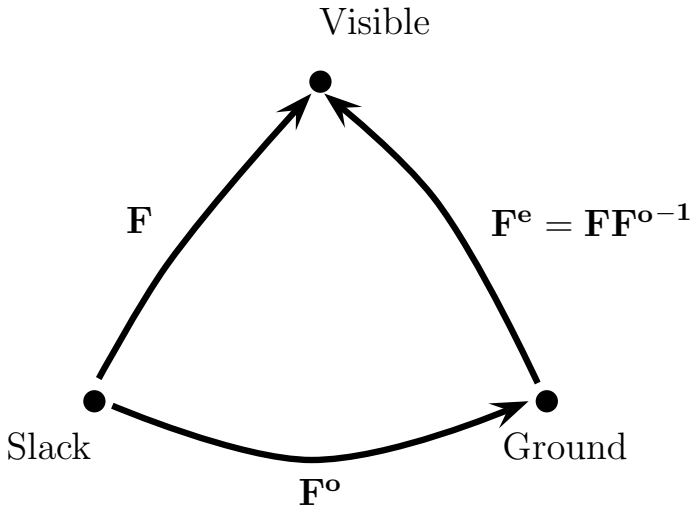

Figure 5.2: Multiplicative decomposition of deformation gradient

centration similar to the active stress counterpart as[UMM00]

$$\mathbf{F}^o = \alpha \mathbf{e}_1 \otimes \mathbf{e}_1 + \beta \mathbf{e}_2 \otimes \mathbf{e}_2 + \gamma \mathbf{e}_3 \otimes \mathbf{e}_3$$

where $\mathbf{e_i}$'s defines the isotropy plane of the muscle distribution. The parameters α, β, γ depends on the intercellular calcium concentration c. The form of $\mathbf{F}^o$ is typically chosen to model incompressibility i.e., $\det(\mathbf{F}^o) = 1$. Hence there exists one relationship between the constants α, β, γ from the incompressibility constraint. Following Pelce and Sun [PSL95] the constants are modeled using a sigmoid function as

$$\gamma = K(A - \log(\kappa \tanh(c) + c_o)) \tag{5.1}$$

where c is the calcium concentration, K, A, κ, c_o are some constants. The value of κ determines the sharpness of the sigmoid response curve. c_o defines a reference calcium concentration below which there is no contraction and once the calcium concentration increases over this there is an active contraction.

5.2 Finite Elasticity

Muscle fibers response to loading is dependent on the presence of a stimulus, as observed in Hill's experiment. Mechanically, the muscle has a non-linear, elastic response capable of large deformations with the predominant orientation of the fibers introducing a preferred material direction. When a stimulus is introduced, the sarcomeres begin to contract, altering the material response. In order to construct a model describing the three dimensional behavior of the heart we need a constitute law which describes the active and passive aspects in the behavior of the muscle fiber. Most existing models of myofibril excitation-contraction [PH97] mainly reply on the heuristic approaches and experimental testing. Modelers have used a decoupled strain-energy formulation where they separate out the active and passive part of the strain energy for a skeletal muscle. The reason behind is, the passive state has the advantage of more extensive testing and experimental

data for activated muscle are not as available due to the difficulty of conducting appropriate tests [NT07]. Often the passive and active part are assumed to have the same strain energy function.

Following this approach we assume that activation simply changes the resting state of the muscle, i.e., transforming the reference configuration from ground to slack. We assume that the elastic properties remain the same. Then the energy is simply the strain energy relative to the slack state i.e, $W(\mathbf{F}^e)$. Hence we define the total energy of the system as

$$\Pi[\mathbf{F}] = \int_v W(\mathbf{F}^e)\, dV \tag{5.2}$$

Consider the variation of the Equation 5.2

$$\delta\Pi[\mathbf{F}] = \int_V \frac{\partial W}{\partial \mathbf{F}} \delta\mathbf{F}\, dV \tag{5.3}$$

The strain energy is function of the elastic part of the deformation gradient. Using chain rule we say

$$\frac{\partial W}{\partial \mathbf{F}} = \frac{\partial W}{\partial \mathbf{F}^e}\frac{\partial \mathbf{F}^e}{\partial \mathbf{F}} \tag{5.4}$$

The term $\dfrac{\partial W}{\partial \mathbf{F}^e} = \mathbf{P}$ which is nothing but the first Piola-Kirchoff stress. We can rewrite Equation 5.4 and simplify using indicial notation

$$\frac{\partial W}{\partial F_{iJ}} = \frac{\partial W}{\partial F^e_{kL}}\frac{\partial F^e_{kL}}{\partial F_{iJ}} \tag{5.5}$$

$$= P_{kL}\frac{\partial F^e_{kL}}{\partial F_{iJ}}, \quad \mathbf{F}^e = \mathbf{F}\mathbf{F}^{o-1} \text{ or } F^e_{kL} = F_{kM}F^{o-1}_{ML} \tag{5.6}$$

$$= P_{kL}\frac{\partial F_{kM}F^{o-1}_{ML}}{\partial F_{iJ}} \tag{5.7}$$

$$= P_{kL}\delta_{ik}\delta_{MJ}F^{o-1}_{ML} = P_{iL}F^{o-1}_{JL} = \mathbf{P}\mathbf{F}^{o-T} \tag{5.8}$$

Substituting this in Equation 5.3 we get

$$\delta\Pi[\mathbf{F}] = \int_V \mathbf{P}\mathbf{F}^{o-T}\delta\mathbf{F}\, dV \tag{5.9}$$

Since the material behavior is non-linear we need to compute the incremental constitutive relation. We perturb $\mathbf{F}^e$ to $\mathbf{F}^e + d\mathbf{F}$ which causes the first Poila

Kirchoff stress to change from $\mathbf{P}$ to $\mathbf{P} + d\mathbf{P}$. The incremental first Piola Kirchoff stress is then defined as

$$dP_{iJ} = \frac{\partial P_{iJ}}{\partial F_{kL}} dF_{kL} = \frac{\partial^2 W}{\partial F_{iJ} F_{kL}} dF_{kL} = \mathbb{C}_{iJkL} dF_{kL}$$

where $\mathbb{C}$ is called the Lagrangian or Tangent Elastic Moduli. In our case we have

$$\begin{aligned} \frac{\partial^2 W}{\partial F_{iJ} F_{kL}} &= \frac{\partial}{\partial F_{kL}} \left(\frac{\partial W}{\partial F_{iJ}} \right) = \frac{\partial}{\partial F^e_{pQ}} \left(\frac{\partial W}{\partial F^e_{iL}} F^{o-1}_{JL} \right) F^{o-1}_{LQ} \\ &= \frac{\partial}{\partial F_{kL}} \left(\frac{\partial W}{\partial F^e_{iL}} \right) F^{o-1}_{JL} F^{o-1}_{LQ} = \mathbb{C}_{kQiL} F^{o-1}_{JL} F^{o-1}_{LQ} \ = \mathbb{C} \mathbf{F}^{o-T} \mathbf{F}^{o-T} \end{aligned} \quad (5.10)$$

We derive the first Piola-Kirchoff stress and Lagrangian modulus based for the material models chosen in the following sections.

5.2.1 Neo-Hookean material model

We assume the material to be a Neo-Hookean material extended to compressible rangle. Modeling a material as purely incompressible causes numerical instabilities. Hence we impose a high bulk modulus to model incompressibility. For this material model we have

$$W = \frac{1}{2} \lambda_0 \log^2 J^e - \mu_0 \log J^e + \frac{\mu_0}{2} (\operatorname{tr} \mathbf{C}^e - 3) \quad (5.11)$$

where $\mathbf{C^e}$ is the left Cauchy-Green tensor defined as $\mathbf{C^e} = \mathbf{F^{eT} F^e}$. λ_0 needs to made high to impose incompressibility. We compute $\mathbf{P}$ with this strain energy definition using indicial notation as

$$P_{iL} = \frac{\partial W}{\partial F^e_{iL}} = \lambda_0 \log J^e \frac{1}{J^e} \frac{\partial J^e}{\partial F^e_{iL}} - \frac{\mu_0}{J^e} \frac{\partial J^e}{\partial F^e_{iL}} + \frac{\mu_0}{2} \frac{\partial \operatorname{tr} \mathbf{C}^e}{\partial F^e_{iL}} \quad (5.12)$$

To simplify the expression we consider each term one at a time. We know $J^e = \epsilon_{PQR} F^e_{1P} F^e_{2Q} F^e_{3R}$. Hence

$$\begin{aligned}
\frac{\partial J^e}{\partial F_{iL}} &= \epsilon_{PQR}\delta_{1i}\delta_{PL}F^e_{2Q}F^e_{3R} + \epsilon_{PQR}F^e_{1P}\delta_{2i}\delta_{QL}F^e_{3R} + \epsilon_{PQR}F^e_{1P}F^e_{2Q}\delta_{3i}\delta_{RL} \\
&= \epsilon_{LQR}F^e_{2Q}F^e_{3R}F^e_{1L}F^{e-1}_{\ \ Li} + \epsilon_{PLR}F^e_{1P}F^e_{3R}F^e_{2L}F^{e-1}_{\ \ Li} + \epsilon_{PQL}F^e_{1P}F^e_{2Q}F^3_{3L}F^{e-1}_{\ \ Li} \\
&= (\epsilon_{LQR}F^e_{1L}F^e_{2Q}F^e_{3R} + \epsilon_{PLR}F^e_{1P}F^e_{2L}F^e_{3R} + \epsilon_{PQL}F^e_{1P}F^e_{2Q}F^e_{3L})F^{e-1}_{\ \ Li} \\
&= (\epsilon_{LQR}F^e_{1L}F^e_{2Q}F^e_{3R} + \epsilon_{PLR}F^e_{1P}F^e_{2L}F^e_{3R} - \epsilon_{PLR}F^e_{1P}F^e_{2L}F^e_{3R})F^{e-1}_{\ \ Li} = J^e F^{e-1}_{\ \ Li}
\end{aligned} \tag{5.13}$$

For the second term we have $\operatorname{tr}\mathbf{C}^e = C^e_{NN} = F^e_{pN}F^e_{pN}$. Hence

$$\frac{\partial \operatorname{tr}\mathbf{C}^e}{\partial F^e_{iL}} = 2\delta_{pi}\delta_{NL}F^e_{pN} = 2F^e_{iL} \tag{5.14}$$

Combining all terms together we get the First Piola Kirchoff stress as

$$\begin{aligned}
P_{iL} &= \lambda_0 \log J^e \frac{1}{J^e} J^e F^{e-1}_{\ \ Li} - \frac{\mu_0}{J^e} J^e F^{e-1}_{\ \ Li} + \frac{\mu_0}{2} 2F^e_{iL} \\
&= \lambda_0 \log J^e F^{e-1}_{\ \ Li} - \mu_0 F^{e-1}_{\ \ Li} + \mu_0 F^e_{iL} = (\lambda_0 \log J^e - \mu_0)F^{e-1}_{\ \ Li} + \mu_0 F^e_{iL}
\end{aligned} \tag{5.15}$$

Substituting this in Equation 5.9 we get

$$\delta\Pi[F] = \int_V \left((\lambda_0 \log J^e - \mu_0)F^{e-1}_{\ \ Li} + \mu_0 F^e_{iL}\right) F^{0\,-1}_{\ \ JL}\delta F_{iJ}\, dV$$

We now compute the Lagrangian Moduli defined as

$$\mathbb{C}_{iJmN} = \frac{\partial P_{iL}}{\partial F^e_{mN}} F^{o-1}_{\ \ JL}$$

We will first compute $\dfrac{\partial F^{e-1}_{Li}}{\partial F^{e}_{mN}}$. We use the fact that $\mathbf{F}\mathbf{F}^{-1} = \mathbf{I}$. In indicial form we have $\delta_{ji} = F^{e}_{jL}F^{e-1}_{Li}$. Taking derivative with respect to F^{e}_{mN} we get

$$\begin{aligned}
0 &= \frac{\partial F^{e}_{jL}}{\partial F^{e}_{mN}}F^{e-1}_{Li} + F^{e}_{jL}\frac{\partial F^{e-1}_{Li}}{\partial F^{e}_{mN}} \\
F^{e}_{jL}\frac{\partial F^{e-1}_{Li}}{\partial F^{e}_{mN}} &= -\delta_{jm}\delta_{LN}F^{e-1}_{Li} = -\delta_{jm}F^{e-1}_{Ni} \\
F^{e-1}_{pj}F^{e}_{jL}\frac{\partial F^{e-1}_{Li}}{\partial F^{e}_{mN}} &= -\delta_{jm}F^{e-1}_{pj}F^{e-1}_{Ni} \\
\delta_{pL}\frac{\partial F^{e-1}_{Li}}{\partial F^{e}_{mN}} &= -F^{e-1}_{pm}F^{e-1}_{Ni} \\
\frac{\partial F^{e-1}_{Li}}{\partial F^{e}_{mN}} &= -F^{e-1}_{Lm}F^{e-1}_{Ni} \qquad (5.16)
\end{aligned}$$

We proceed using this as

$$\begin{aligned}
\frac{\partial P_{iL}}{\partial F^{e}_{mN}} &= \lambda_0\left(\frac{1}{J^e}\frac{\partial J^e}{\partial F^{e}_{mN}}F^{e-1}_{Li} + \log J^e\frac{\partial F^{e-1}_{Li}}{\partial F^{e}_{mN}}\right) - \mu_0\frac{\partial F^{e-1}_{Li}}{\partial F^{e}_{mN}} + \mu_0\frac{\partial F^{e}_{iL}}{\partial F^{e}_{mN}} \\
&= \lambda_0\left(F^{e-1}_{Nm}F^{e-1}_{Li} - \log J^e F^{e-1}_{Lm}F^{e-1}_{Ni}\right) + \mu_0 F^{e-1}_{Lm}F^{e-1}_{Ni} + \mu_0\delta_{im}\delta_{LN} \qquad (5.17)
\end{aligned}$$

Hence the Lagrangian Moduli is

$$\mathbb{C}_{iJmN} = (\lambda_0(F^{e-1}_{Nm}F^{e-1}_{Li} - \log J^e F^{e-1}_{Lm}F^{e-1}_{Ni}) + \mu_0 F^{e-1}_{Lm}F^{e-1}_{Ni} + \mu_0\delta_{im}\delta_{LN})F^{o-1}_{JL} \qquad (5.18)$$

5.2.2 Holzapfel Model

Holzapfel and Ogden [HO09] proposed a hyperelastic constitutive model which includes tranverse isotropy and was also fit to experimental data. The strain energy proposed is

$$W = \frac{a}{2b}\exp[b(I_1 - 3)] + \sum_{i=f,s}\frac{a_i}{b_i}\left\{\exp[b_i(I_{4i} - 1)^2] - 1\right\} + \frac{a_{fs}}{b_{fs}}\left[\exp(b_{fs}I^2_{8fs}) - 1\right]$$

where a and b are fit from experimental data $\mathbf{f}$ denotes the fiber direction and $\mathbf{s}$ denotes the sheet direction. The invariant I_4 and I_8 are computed as

$$I_4 = \mathbf{f}\cdot\mathbf{C}^{\mathbf{e}}\mathbf{f} \quad I_8 = \mathbf{f}\cdot\mathbf{C}^{\mathbf{e}}\mathbf{s}$$

The material model assumes the material to be incompressible. We modify the material model by adding terms similar to terms present in the compressible Neo-Hookean model and write the strain energy as

$$W = \frac{1}{2}\left[\lambda_0 \log^2 J^e - \mu_0 \log J^e + \frac{a}{2b}\exp[b(I_1-3)] + \sum_{i=f,s}\frac{a_i}{2b_i}\left\{\exp[b_i(I_{4i}-1)^2]-1\right\} + \frac{a_{fs}}{2b_{fs}}\left[\exp(b_{fs}I_{8fs}^2)-1\right]\right] \tag{5.19}$$

The value of λ_0 can be thought of as a penalty constant used to impose incompressibility. The value of μ_0 can be computed by imposing the condition that the first Piola-Kirchoff stress should be 0 when the deformation gradient is identity. Using a similar approach as outlined in the earlier section with compressible Neo-Hookean material we get the first Piola-Kirchoff stress as

$$\begin{aligned} P_{iJ}^e = &\left(\frac{\lambda_0}{J^e}\log J^e - \frac{\mu_0}{J^e}\right)\frac{\partial J^e}{\partial F_{iJ}^e} + \frac{a}{2b}\exp(b(I_1-3))\frac{\partial b(I_1-3)}{\partial F_{iJ}^e} + \\ &\sum_{i=f,s}\frac{a_i}{2b_i}\left\{\exp[b_i(I_{4i}-1)^2]-1\right\}\frac{\partial(b_i(I_{4i}-1)^2]-1)}{\partial F_{iJ}^e} + \\ &\frac{a_{fs}}{2b_{fs}}\left[\exp(b_{fs}I_{8fs}^2)-1\right]\frac{\partial(b_{fs}I_{8fs}^2)}{\partial F_{iJ}^e} \end{aligned} \tag{5.20}$$

When $\mathbf{F} = \mathbf{I}$ we get $I_1 = 3$ and $J^e = 1$. Also $I_4 = \mathbf{f}\cdot\mathbf{If} = 1$ and $I_8 = \mathbf{f}\cdot\mathbf{Is} = \mathbf{f}\cdot\mathbf{s} = 0$. Hence we get

$$0 = -\mu_0\frac{\partial J^e}{\partial F_{iJ}^e} + \frac{a}{2}2F_{iJ}^e = aF_{iJ}^e - \mu_0 F^{e\,-1}_{Ji} = (a-\mu_0)F_{iJ}^e \tag{5.21}$$

Since $\mathbf{F}$ is identity we get $\mathbf{F}^{-1} = \mathbf{F}$. Hence $\mu_0 = a$. The first Piola-Kirchoff stress can be computed as

$$\begin{aligned} \mathbf{P} = &a\exp(b(I_1-3))\mathbf{F} + 2\mathbf{F}\big(a_f(I_{4f}-1)\exp(b_f(I_{4f}-1)^2)\mathbf{f}\otimes\mathbf{f} + \\ &a_s(I_{4s}-1)\exp(b_s(I_{4s}-1)^2)\mathbf{s}\otimes\mathbf{s}\big) + a_{fs}I_{8fs}\exp(b_{fs}I_{8fs}^2)\mathbf{F}(\mathbf{f}\otimes\mathbf{s}+\mathbf{s}\otimes\mathbf{f}) \\ &+ (\lambda_0\log J^e - a)\mathbf{F}^{-T} \end{aligned}$$

We define $\mathbf{Uff} = \mathbf{f}\otimes\mathbf{f}$, $\mathbf{Uss} = \mathbf{s}\otimes\mathbf{s}$, $\mathbf{Vfs} = \mathbf{f}\otimes\mathbf{s}+\mathbf{s}\otimes\mathbf{f}$, $\mathbf{FUff} = \mathbf{F}(\mathbf{f}\otimes\mathbf{f})$, $\mathbf{FUss} = \mathbf{F}(\mathbf{s}\otimes\mathbf{s})$ and $\mathbf{FVfs} = \mathbf{F}(\mathbf{f}\otimes\mathbf{s}+\mathbf{s}\otimes\mathbf{f})$. The lagrangian modulus can be

expressed as

$$
\begin{aligned}
\mathbb{C}_{iJkL} =& a\exp(b(I_1-3))\big(2bF^e_{iJ}F^e_{kL}+\delta_{ik}\delta_{JL}\big)+\\
& 2a_f\exp(b_f(I_{4f}-1)^2)\big(2\mathrm{FUff}_{iJ}\mathrm{FUff}_{kL}(1+2b_f(I_{4f}-1)^2)+(I_{4f}-1)\delta_{iK}\mathrm{Uff}_{LJ}\big)+\\
& 2a_s\exp(b_s(I_{4s}-1)^2)(2\mathrm{FUss}_{iJ}\mathrm{FUss}_{kL}(1+2b_s(I_{4s}-1)^2)+(I_{4s}-1)\delta_{ik}\mathrm{Uss}_{LJ}\big)+\\
& a_{fs}\exp(b_{fs}(I_{8fs})^2(\mathrm{FVfs}_{iJ}\mathrm{FVfs}_{kL}(1+2b_{fs}(I_{8fs})^2+I_{8fs}\delta_{iK}\mathrm{Vfs}_{LJ})+\\
& \lambda_0 F^{e-1}_{Ji}F^{e-1}_{Lk}-(\lambda_0\log J^e-a)F^{e-1}_{Jk}F^{e-1}_{Li}
\end{aligned}
$$

5.2.3 Internal force and Tangent stiffness Matrix

To compute the internal forces we will plug in the finite element approximation

$$\boldsymbol{\phi}=\sum_{a=1}^{N}\mathbf{x}_a N_a(\mathbf{X})$$

Now we can express the elastic part of $\mathbf{F}$ as

$$\mathbf{F}^e=\sum_a \mathbf{x}_a\nabla N_a(\mathbf{X})$$

where ∇ denotes derivatives with respect to the material coordinate system $\mathbf{X}$. Using this Equation 5.9 can be rewritten as

$$\delta\Pi[\mathbf{F}]=\sum_a\int_V P_{iL}N_{a,J}(\mathbf{X})F^{o-1}_{JL}\delta x_{a,i}\,dV \tag{5.22}$$

where $N_{a,J}$ denotes the derivative of the shape function along the J^{th} dimension and $x_{a,i}$ denotes the i^{th} dimension of the position. This can be further be rewritten as

$$\delta\Pi[\mathbf{F}]=\sum_a \mathbf{f}^{int}_{ia}\delta x_{ia} \tag{5.23}$$

where $\mathbf{f}^{int}$ denotes the internal forces in the body. The tangent stiffness matrix can now be computed as

$$\mathbf{K}=\frac{\partial\mathbf{f}^{int}}{\partial\mathbf{x}} \tag{5.24}$$

In indicial form we get

$$K_{iakb} = \int_V \frac{\partial P_{iL}}{\partial F_{mR}} \frac{\partial F_{mR}}{\partial x_{kb}} N_{a,J} F^{o-1}_{JL}\, dV = \int_V \mathbb{C}_{iLmR} N_{a,J} N_{b,R} F^{o-1}_{JL} \delta_{mk}\, dV$$
$$= \int_V \mathbb{C}_{iLkR} N_{a,J} N_{b,R} F^{o-1}_{JL}\, dV \tag{5.25}$$

where a, b are summation over nodes and i, k are the degrees of freedom at each node. From a computational standpoint the stiffness matrix is not stored as 4^{th} order tensor but rolled into a 2D matrix using Voigt notation. The entries in the stiffness matrix would be $(a \times \dim + i, b \times \dim + k)$. From the definition $\mathbb{C}$ we infer that $\mathbb{C}_{iJkL} = \mathbb{C}_{kLiJ}$. The stiffness matrix is also symmetric. This can be proved as

$$K_{iakb} = \int_V \mathbb{C}_{iLkR} N_{a,J} N_{b,R} F^{o-1}_{JL}\, dV = \int_V \mathbb{C}_{kRiL} N_{b,R} N_{a,J} F^{o-1}_{JL}\, dV \tag{5.26}$$
$$= \int_V \mathbb{C}_{kRiL} N_{b,J} N_{a,R} F^{o-1}_{RL}\, dV = K_{kbia} \tag{5.27}$$

5.3 Numerical Implementation

Stretch activated ion channels were not included in the ionic model. These are channels which get turned on due to the effect of mechanics. Hence the underlying assumption is the mechanical deformation does not change any cell properties. For the mechanics portion of the coupled problem we have

$$\mathbf{f^{int}}(\mathbf{u} + \boldsymbol{\Delta}\mathbf{u}, \mathbf{x}) - \mathbf{f^{ext}}(\mathbf{x}) = 0$$

The internal force vector at the nth step is computed using the Voltage at nth step from the EP solve. Using Taylor's expansion we get

$$\mathbf{f^{int}}(\mathbf{u}, \mathbf{x}) - \mathbf{f^{ext}}(\mathbf{x}) + \frac{\partial \mathbf{f^{int}}(\mathbf{u}, \mathbf{x})}{\partial u} \Delta\mathbf{u} = 0$$

which can be rewritten we

$$\mathbf{f^{int}}(\mathbf{u}, \mathbf{x}) - \mathbf{f^{ext}}(\mathbf{x}) + \mathbf{K}\Delta\mathbf{u} = 0 \quad \Rightarrow \mathbf{K}\Delta\mathbf{u} = \mathbf{f^{ext}}(\mathbf{x}) - \mathbf{f^{int}}(\mathbf{u}, \mathbf{x})$$

The algorithm for the coupled solved is as shown below.

Algorithm 2 Solving for Mechanics

$\mathbf{u} = 0$

TOLER= 10^{-5}

Compute $\mathbf{F}^o = f(\gamma)$

while ERROR > TOLER **do**

$F_{iJ} = \sum_{a=1}^{N} N^a_{,J} a x^a_i$

$\mathbf{F}^e = \mathbf{F}(\mathbf{F}^o)^{-1}$

$\mathbf{f^{residual}} = \mathbf{f^{ext}} - \mathbf{f^{int}}$

$K_{iakb} = \int_V \mathbb{C}_{iLkR} N_{a,J} N_{b,R} F^{o-1}_{JL}\, dV$

$\mathbf{\Delta u} = \mathbf{K}^{-1}\mathbf{f^{residual}}$

$\mathbf{u} = \mathbf{u} + \mathbf{\Delta u}$

ERROR = $||\mathbf{f^{ext}} - \mathbf{f^{int}}||_2$

end while

5.4 2D simulation

A 2D block of dimension 5×4cm was meshed uniformly with 200μm sized quadrilateral elements. The four corners of the block were fixed in all translational degrees of freedom. A circular stimulus over a region of 1cm was applied at the center of the block for 5ms. The material was assumed to be compressible Neo-Hookean material. Since this is a 2D analysis the form of the active part of the deformation gradient which would also be 2D was assumed as

$$\mathbf{F}^o = \gamma \mathbf{e}_1 \otimes \mathbf{e}_1 + \frac{1}{\gamma} \mathbf{e}_2 \otimes \mathbf{e}_2$$

The chosen form of the active part of the deformation gradient ensures incompressibility in the active part also. The contraction in one direction is compensated by expansion in another direction. The fibers were assumed to aligned with X axis and hence the fastest conduction direction is along X which would experience contraction and equivalent expansion would be experienced in Y direction. Figure 5.3 shows the voltage contour on the deformed shape at different time snaps

during the simulation.

5.5 3D Bar simulation

A 3D bar of dimension $0.5 \times 0.5 \times 1$cm was used as the computational domain. One face of the bar was fixed in all translation degrees of freedom. A stimulus of 50000μA/cc was applied at the same end for nodes within a distance of 0.1cm from the end along the axis of the bar. The active part of the deformation gradient which would also be 2D was assumed as

$$\mathbf{F}^o = \gamma(\mathbf{e}_1 \otimes \mathbf{e}_1 + \mathbf{e}_2 \otimes \mathbf{e}_2) + \frac{1}{\gamma^2}\mathbf{e}_3 \otimes \mathbf{e}_3$$

300ms was simulated. Compressible Neo-Hookean was chosen as the material model. X and Y define the plane of the bar and Z defines the axis of the bar. The form of the active part of the deformation gradient ensure incompressibility on the active part similar to the 2D analysis. The form chosen provides contraction in the X and Y direction which is compensated by expansion in the Z direction. The geometry can be though of as representing a fiber tissue in the heart.. Figure 5.4 shows the voltage contour on the deformed shape at different time snaps during the simulation.

The thinning in the in-plane dimension is compensated by the extension in the out of plane direction.

5.6 Rabbit ventricle model simulation

Based on experimental observation there are certain physiological requirements which need to be satisfied by the mechanics simulation. They are

1. The muscle fiber contracts by 20%,

2. In a normal healthy heart the ejection fraction should be in the range of

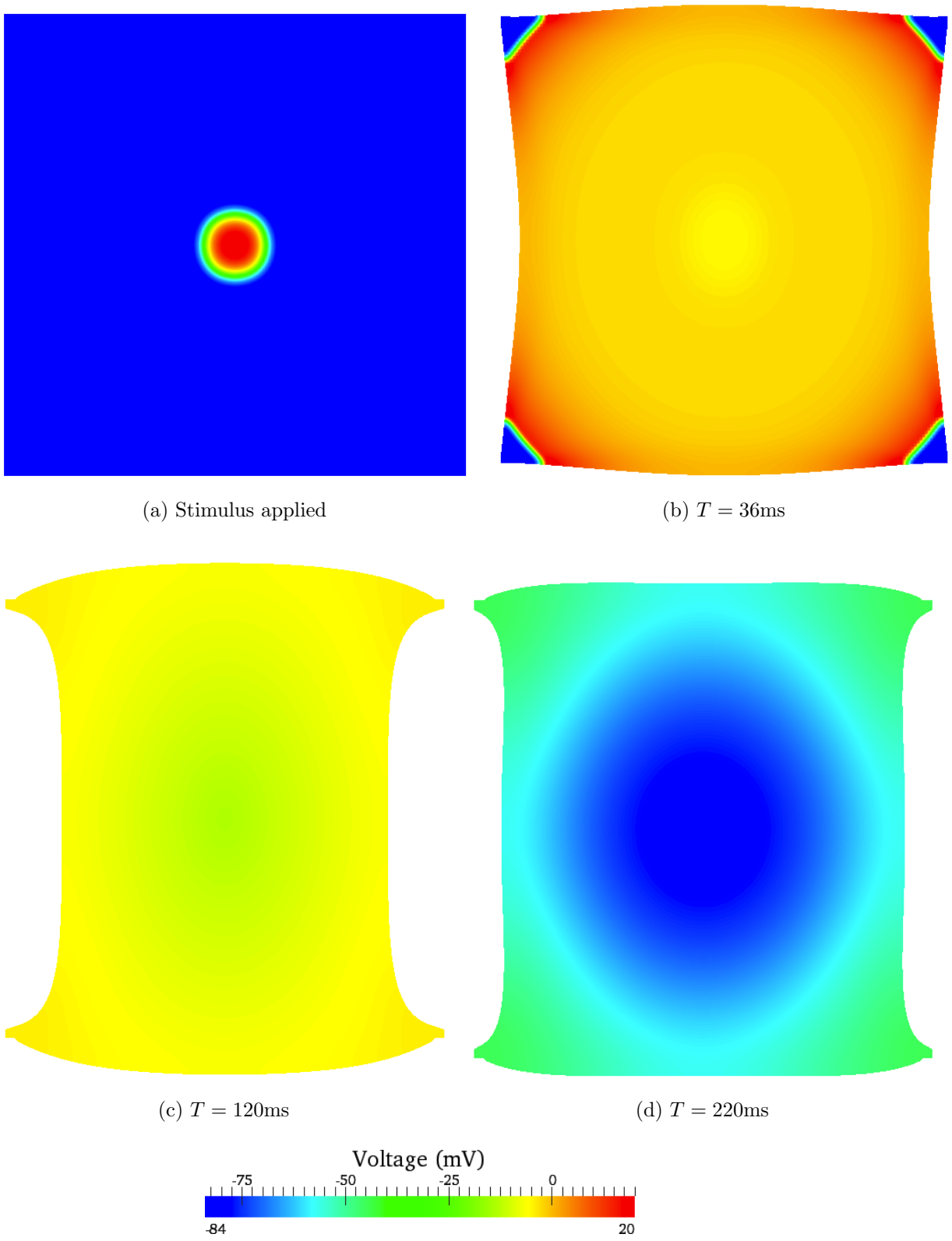

(a) Stimulus applied

(b) $T = 36$ms

(c) $T = 120$ms

(d) $T = 220$ms

(e) Voltage scale

Figure 5.3: Deformed shape of 2D block showing voltage contour plot at different time steps

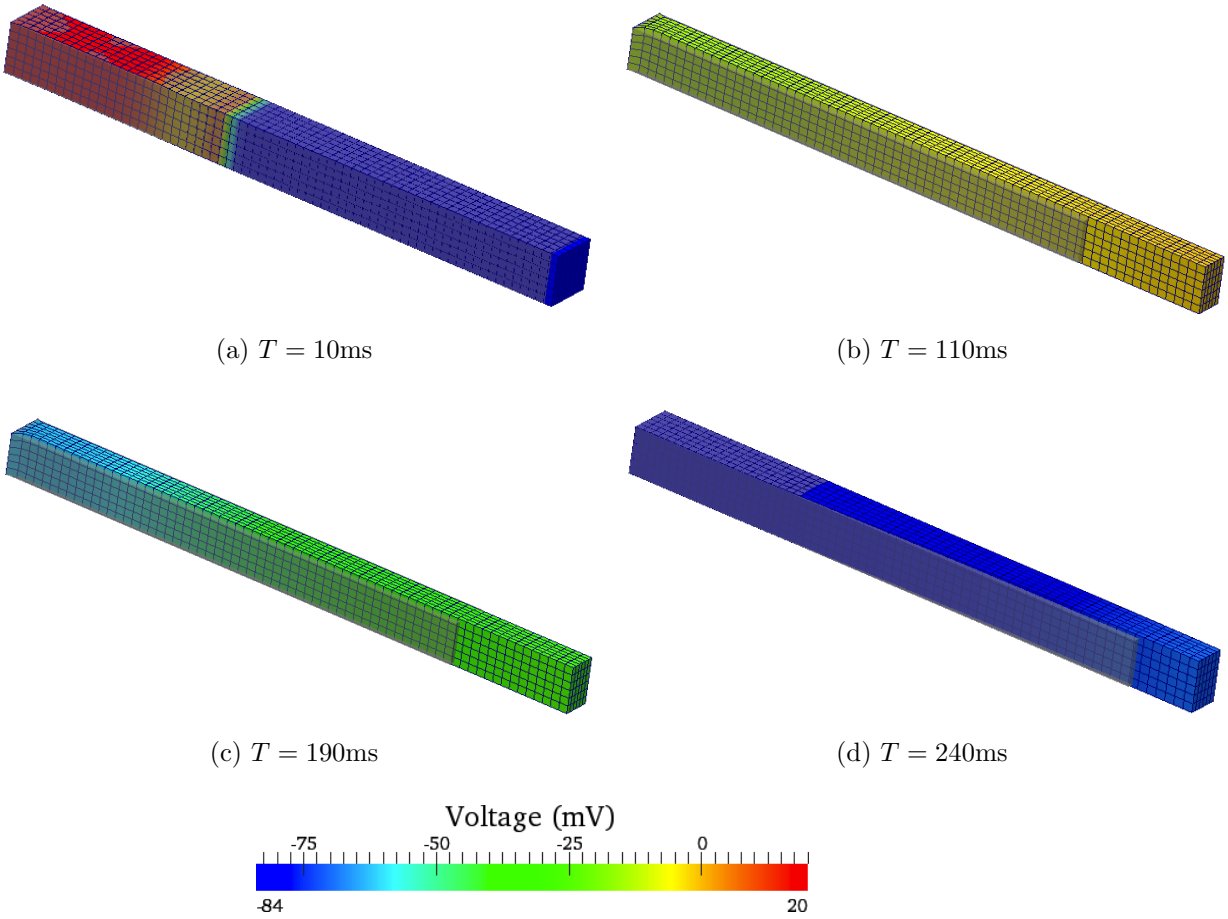

(a) $T = 10$ms

(b) $T = 110$ms

(c) $T = 190$ms

(d) $T = 240$ms

(e) Voltage scale

Figure 5.4: Deformed shape of 3D block showing voltage contour plot at different time snaps

$60 - 70\%$,

3. The epicardial surface only twists and does not move inward or outward,
4. The endocardial surface twists. Also there is a inward movement of the endocardial surface which results in wall thickening,
5. The base of the heart twists and moves down,
6. The apex of the heart only twists and
7. The resulting wall thickening is more than fiber shortening.

The form of $\mathbf{F}^o$ was chosen as

$$\mathbf{F}^o = \gamma(\mathbf{e}_1 \otimes \mathbf{e}_1 + \mathbf{e}_2 \otimes \mathbf{e}_2) + \frac{1}{\gamma^2}\mathbf{e}_3 \otimes \mathbf{e}_3$$

which is similar to what was chosen earlier. We know that several factors contribute to achieving the right ejection fraction. As a first step we wanted to see the effect of not including anisotropy and see its influcen on the ejection fraction. The form is $\mathbf{F}^o$ was chosen purely from a kinematic standpoint to produce maximum thickening. Compressible Neo-Hookean material model was chosen.An apical stimulus was applied to the model for 5ms. Figure 5.5 shows the voltage evolution on the deformed configuration. From the deformed configuration we do not observe twisting phenomenon. Along the Z direction which is aligned with the axis of the heart there is an increase in the dimension by 50%. However we do not observe the wall thickening of the twisting phenomenon which is observed in experiments. Also the calculated ejection fraction is not 60%.This simulation misses the crucial physiological observations. The results underline the importance of including fiber anisotropy in the simulations. Choosing the form of $\mathbf{F}^o$ alone is not enough to reproduce the right mechanical deformation. Hence a material model which includes fiber orientation needs to be used.

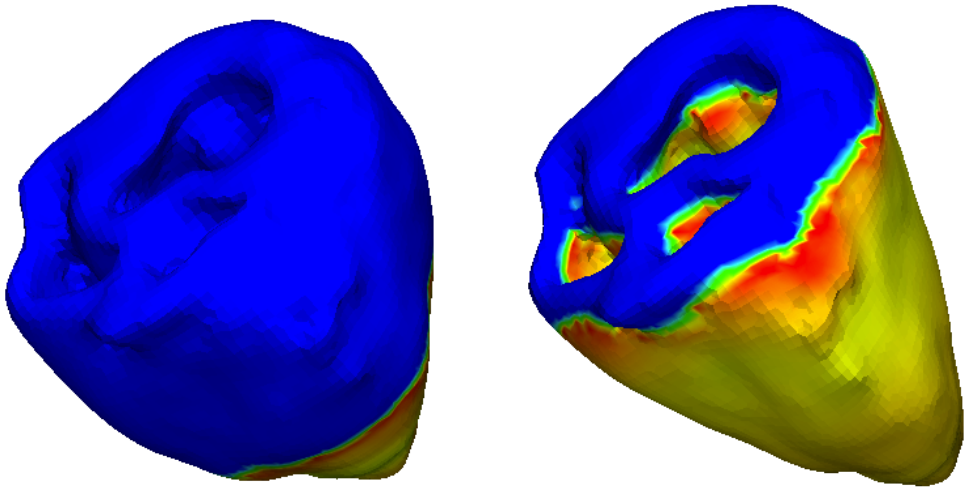

(a) $T = 22$ms

(b) $T = 50$ms

(c) $T = 114$ms

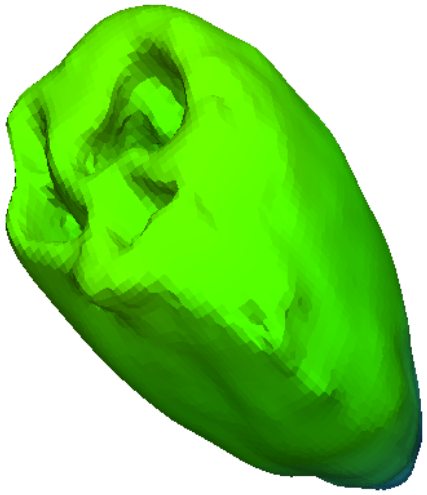

(d) $T = 200$ms

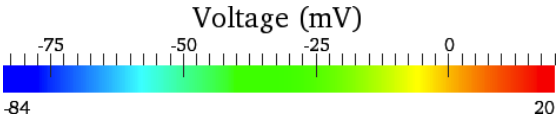

(e) Voltage scale

Figure 5.5: Ventricular model coupled electromechanics simulations.

5.7 Elliptical heart simulation

The afore mentioned numerical experiments point to the importance of the form of the active part of the deformation gradient $\mathbf{F}^o$, material model being used and the inclusion of fiber anisotropy data in simulation. We use the model proposed by Holzapfel and Ogden [HO09] on a simplified ellipsoid model. the ellipsoid represents only the left ventricular cavity. The fiber distribution is assumed to be vary from -80^o on epicardial surface to 60^o in the endocardial surface. This assumption is commonly found in many models [ENP11]. Z is the direction along the axis of the heart.The form of active part of deformation gradient is

$$\mathbf{F}^o = \gamma(\mathbf{e}_1 \otimes \mathbf{e}_1 + \mathbf{e}_2 \otimes \mathbf{e}_2) + \frac{1}{\gamma^2}\mathbf{e}_3 \otimes \mathbf{e}_3$$

An apical stimulus was applied. The boundary conditions were applied as follows. All boundary conditions were only applied in the base region. The entire basal plane was retrained to prevent any motion along the normal of the plane. This in essence would model the effect of the atria over the ventricle. In the inner most circle defining the basal plane 4 points offset by 90^o, 2 of them aligned with X axis and 2 aligned with Y axis were choses. The two aligned with X axis were restrained in Y axis and the two align withY were restrained in X axis. This in essence would eliminate the rigid body modes and let motion in the radial direction. Figure 5.6 shows the voltage evolution in the deformed heart.

This model produces a 60% ejection fraction. Looking at $I_4 = \mathbf{nF^TFn}$ which defines the stretch along the fiber direction when maximum displacement occurs as shown in Figure 5.7 it can be inferred that we do not get uniform contraction over the entire model. There are certain region where more than 20% reduction in fiber length occurs.

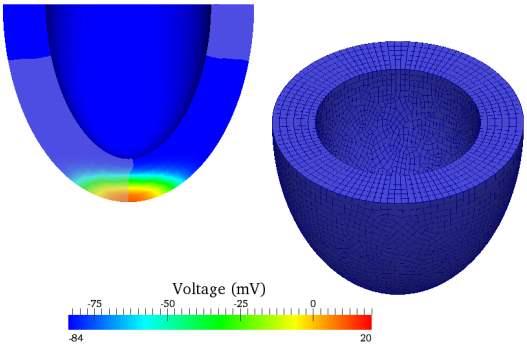

(a) $T = 5$ms

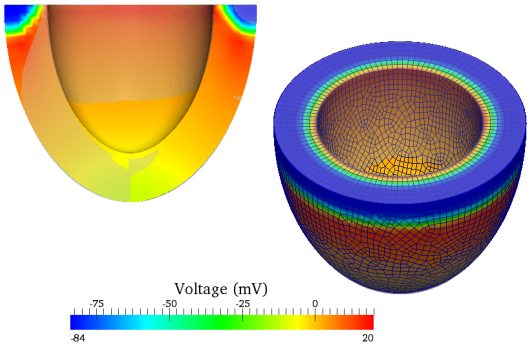

(b) $T = 17.5$ms

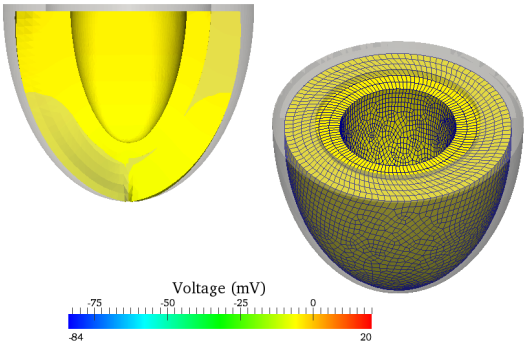

(c) $T = 100$ms

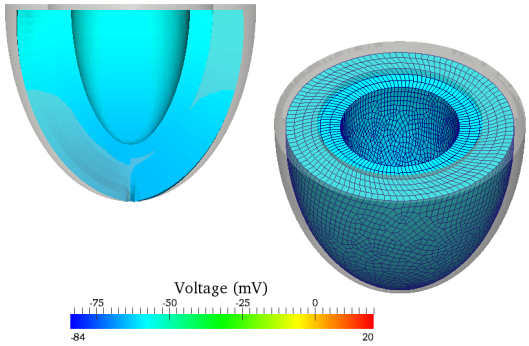

(d) $T = 212.5$ms

Figure 5.6: Deformed shape of ellipsoid heart. The deformed model is superposed on the initial geometry which is transparent. The maximum displacement occurs at $T = 100$ms.

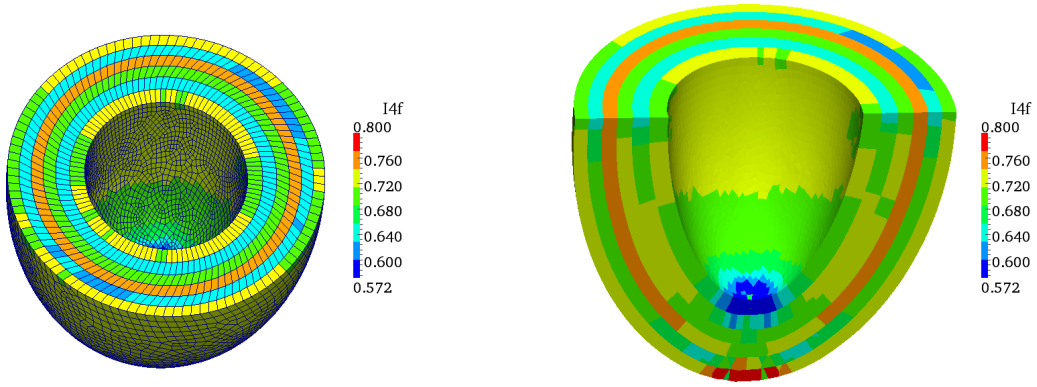

(a) (b)

Figure 5.7: Contour plot of I_4 when maximum deformation occurs in the ellipsoid model

5.8 Inferences

For a numerical model to be validated it has to satisfy the experimental observations which were laid out in the earlier sections. Several factors such as the form of the active part of the deformation gradient, geometry of the model, fiber anisotropy, material model, variation in APD have been attributed to producing the twisting action. In this chapter we modeled the mechanical deformation using an active strain approach and evaluated the effect of the form of deformation gradient and material model on producing the right mechanical motion. We infer that just choosing a form of deformation gradient which produces maximum thickening alone is not enough to give the right mechanical motion. When coupled with the orthotropic Holzapfel model the ellipsoid model reproduces a 60% EF.

While using material models available in literature caution needs to be excersied. Several passive myocardium material models have been proposed in the literature and different authors have developed methods to identify the necessary material parameters from experimental measures. However, the lack of uniqueness of the identified parameters limits their use to predict mechnical motion.

CHAPTER 6

Concluding thoughts

In this thesis we first examined the combined effects of operator splitting and spatial integration schemes on the accuracy and efficiency of finite-element solution of the reaction-diffusion equations of cardiac electrophysiology. In particular, we have made a break from the standard approach of computing "lumped" approximations to the consistent capacitance and mass matrices that appear in a variational formulation of the boundary value problem. The common argument for mass lumping is efficiency it decouples the nodal equations governing time evolution of voltage, thereby allowing for trivial local time-stepping updates, which are much more CPU-efficient than the solution of coupled linear systems with global (but sparse and banded) matrices. Adding to the observations of others, we have shown that this efficiency can sometimes come at a cost of reduced accuracy. However, our convergence studies show that the six distinct choices for selective lumping can produce a wide range of convergence behaviors. Two schemes, **L-LC** and **C-LL** – exhibit excellent accuracy.

We examined the accuracy and efficiency of these selectively-lumped operator-split formulations through a sequence of benchmark problems, ranging from simple uniaxial wavefront propagation to spiral wave breakup. We find that results are generally satisfactory for the **L-LC** and **C-LL** schemes when element sizes are less than about 200μm. From the numerical studies we show that for nonuniform meshes it is generally the size of the largest elements (and not the smallest or average) that controls the accuracy of the solution and the presence or absence

of spurious artifacts. This is of utmost importance when study physiological phenomenon such as re-entry and spiral wave break-up where the element size when not sufficiently fine enough can lead to spurious corner formation in wave fronts, or even the extinguishing of waves that should continue to propagate etc.

We have considered the requirements for producing a validated numerical model. We stipulate the validation criterion that needs to be met at each level to produce physiologically acceptable results. A successful model of cardiac EP must incorporate correct methods and validate them from primary image acquisition to the final computed EP. Proper imaging techniques needs to be used to generate the computer model and the interpolation scheme which produces minimal error should be used to transfer diffusion tensor information from the scans to the finite element model. It is crucial to include the Purkinje conduction system in the model to reproduce the right activation pattern and obtain the right ECG. Also this created structure needs to fine enough to produce synchronous activation and not a sparse structure. PMJ's need to be modeled to allow bi directional flow of current as this is relevant in model physiological conditions such as Bundle Branch Block.

To model the mechanical motion we use the active strain formulation with a passive material model. We evaluated various forms of the active part of the deformation gradient and various material models. We modeled the coupled electromechanics on a simplified ellipsoid model and successfully reproduced most of the experimental observation. However the form of $\mathbf{F}^o$ was chosen from a pure kinematic standpoint. The physiological relevance of this needs to be understood further. The effect of assuming active and passive material model to be same is also something which needs to be further studied. Also as an extension of the current work some other topics which can be further studied are listed below.

6.1 Meshfree implementation for cardiac electromechanics

Despite impressive progress in automatic meshing techniques, modeling of the complex geometry of cardiac anatomy typically requires careful, painstaking manual segmentation of MRI datasets to generate manifold, boundary conforming meshes of suitable element quality. To avoid this meshing quagmire, a meshfree framework can be developed to construct cardiac EP models directly from MRI data. Meshfree methods enjoy the boundary conforming benefits of finite elements while at the same time avoiding the challenges associated with segmentation and meshing of image data. The framework can potentially be built upon the Modified Reproducing Kernel Particle Method (RKPM) [CPW96] which provides n^{th} order accuracy with polynomial bases, and Stabilized Non-conforming Nodal Integration (SNNI) [CHP07] for efficient and accurate numerical integration.

6.2 Purkinje structure development

The process of modeling the purkinje conduction system is cumbersome and frequently an ad hoc process. The process used in the current work involved manual modification of the purkinje structure, solving the model for voltage and computing the ECG from this output. Work by Ijiri et al [IAY08] and Zimmerman et al [ZSB09] layout automated routines for purkinje generation. However the ECG's computed with these models show fractionations and also have incorrect R wave progression. The length of each conduction branch needs to be determined based the time taken for if to stimulate the ventricle. Non-Hueristic optimization algorithm such as genetic algorithms can be used to develop purkinje structures which will follow anatomy and also produce physiologically accurate ECG's.

6.3 Hyperkalemia characteristics

Hyperkalemia refers to the condition in which the concentration of the electrolyte potassium (K^+) in the blood is elevated. Extreme hyperkalemia is a medical emergency due to the risk of potentially fatal abnormal heart rhythms. This can be modeled by tuning the intracellular potassium concetration in the ionic model. A typical ECG of a patient with Hyperkalemia shows a peaked T wave. With a validated normal healthy heart model the underlying reasons of Hyperkalemia can be studied.

6.4 Pacemaker lead placement and timing

Multiple studies have demonstrated beneficial acute and long-term haemodynamic effects of biventricular (BiV) pacing in patients with chronic heart failure and ventricular dyssynchrony. However, clinical outcome of BiV pacing can be influenced by multiple factors and optimal lead positioning is one of the most important. Berberian at al. [BCQ06] optimized cardiac output using response surface methodology to determine the optimal epicardial lead position and timing. In another work, Dekker et al. [DPD04] conclude that the pressure-volume loops over time offer guidance for placement of epicardial leads. No BiV lead placement optimization has been performed on a fully coupled numerical model. A validated coupled electrophysiology and mechanics model can be used for optimizing BiV lead placement.

6.5 GPU Implementation of cardiac electromechanics

The numerical solution even with the preferential lumping scheme is, computationally demanding because of the fine temporal and spatial sampling required. The demand for real-time high definition 3D graphics has made the new graphic pro-

cessing units (GPUs) a highly parallel, multithreaded, many-core processor with tremendous computational horsepower. Some of the recent publications [XQY04] show the pair of dual GPUs, (4 GPUs) was 1.6X faster than 8 nodes (32 CPUs). However these resort to using finite different routines which is not well suited for mechanics. Future work can focus on implementing a GPU based finite element/meshfree frame work which will provide significant computational speedup.

6.6 Cardiac arrhythmia Modeling

An arrhythmia is a problem with the rate or rhythm of the heartbeat. During an arrhythmia, the heart can beat too fast, too slow, or with an irregular rhythm. Most arrhythmias are harmless, but some can be serious or even life threatening. During an arrhythmia, the heart may not be able to pump enough blood to the body. Lack of blood flow can damage the brain, heart, and other organs. A problem with any part of the electrical process can cause an arrhythmia. For example, in atrial fibrillation, a common type of arrhythmia, electrical signals travel through the atria in a fast and disorganized way. This causes the atria to quiver instead of contract.

The S1-S2 protocol that was used in Chapter 3 can be used to create arrhythmia in a numerical model. The time at which S2 stimulus is applied is very critical. Too early a stimulus gets extinguished immediately and too late a stimulus acts similar to a S1 i.e it does not create scroll wave break up. There is a vulnerable window in which application of the S2 stimulus create scroll waves. Simulations can be performed to identify this vulnerable window. The effect of heart geometry can also be studied with these simulations. DTMRI images of a failure rabbit heart can be used for this. Also an ionic model which represents the failure heart should be used. Hence a 2x2 matrix of runs with normal heart, failure heart and normal cell model and failure cell model can be performed. From these the

vulnerable window can be potentially computed.

6.7 Cardiac electromechanics

With preliminary understanding from the simplified ellipsoid heart model future work can concentrate on

(a) Building a complete unified finite-element model for fully coupled simulation of cardiac electrophysiology and mechanics. The electrophysiology mode developed should include the advanced nonlinear cell models of the UCLA group with anisotropic conduction.

(b) The contraction mechanical model should consist of the most realistic nonlinear anisotropic stress- strain law, and active contractile deformation consistent with physiological Ca binding and cross-bridge kinetics. Using the built framework the electrophysiology and mechanical model canl be coupled on a single finite element mesh.

(c) The heart ejection fraction finally determines heart failure since it is a direct measure of the heart capacity of pumping blood. The correct simulation of this highly important diagnosing factor represents however a computational challenge because, in reality, a 20% reduction in fiber length corresponds to 60% ejection fraction in an healthy heart. Based on the preliminary results the influence of various parameters of getting the right ejection fraction such as inclusion of different active material model in addition to a passive material model, form of the active part of deformation gradient can be studied.

(d) The correct characterization of the heart material tissue is crucial to obtain a realistic computational model and therefore also to compute the heart ejection fraction. The material properties of the heart tissue are also directly related to the health of the heart tissue and may be used to diagnose illness in real

patients. Future work can aim at obtaining uniform and non-uniform material properties of the heart tissues using experimental MRI and DTMRI data and advanced parameter identification techniques.

References

[ADL83] MASOOD AKHTAR, STEPHEN DENKER, MICHAEL H LEHMANN, and REHAN MAHMUD. "Macro-Reentry Within the His Purkinje System." *Pacing and Clinical Electrophysiology*, **6**(5):1010–1028, 1983.

[AFP06] Vincent Arsigny, Pierre Fillard, Xavier Pennec, and Nicholas Ayache. "Log-Euclidean metrics for fast and simple calculus on diffusion tensors." *Magnetic resonance in medicine*, **56**(2):411–421, 2006.

[AIL11] Andrew Atkinson, Shin Inada, Jue Li, James O Tellez, Joseph Yanni, Rakan Sleiman, Eman Abd Allah, Robert H Anderson, Henggui Zhang, Mark R Boyett, et al. "Anatomical and molecular mapping of the left and right ventricular His–Purkinje conduction networks." *Journal of molecular and cellular cardiology*, **51**(5):689–701, 2011.

[ATP06] T.M. Austin, M.L. Trew, and A.J. Pullan. "Solving the cardiac bidomain equations for discontinuous conductivities." *Biomedical Engineering, IEEE Transactions on*, **53**(7):1265–1272, 2006.

[BBP08] MO. Bernabeu, MJ. Bishop, J. Pitt-Francis, DJ. Gavaghan, V. Grau, and B. Rodriguez. "High Performance Computer Simulations for the Study of Biological Functionin 3D Heart Models Incorporating Fibre Orientation and Realistic Geometry atPara-Cellular Resolution." *Computers in Cardiology*, **35**:721–724, 2008.

[BBP09] M.O. Bernabeu, R. Bordas, P. Pathmanathan, J. Pitt-Francis, J. Cooper, A. Garny, D.J. Gavaghan, B. Rodriguez, J.A. Southern, and J.P. Whiteley. "Chaste: Incorporating a Novel Multiscale Spatial and Temporal Algorithm into a Large Scale Open Source Library." *Phil Trans Roy Soc (A)*, **367**(1895):1907–1930, May 2009.

[BCF10] Muriel Boulakia, Serge Cazeau, Miguel A Fernández, Jean-Frédéric Gerbeau, and Nejib Zemzemi. "Mathematical modeling of electrocardiograms: a numerical study." *Annals of biomedical engineering*, **38**(3):1071–1097, 2010.

[BCQ06] G. Berberian, S.E. Cabreriza, T.A. Quinn, C.A. Garofalo, and H.M. Spotnitz. "Left ventricular pacing site-timing optimization during biventricular pacing using a multi-electrode patch." *The Annals of thoracic surgery*, **82**(6):2292–2294, 2006.

[BFG07] Muriel Boulakia, Miguel A Fernández, Jean-Frédéric Gerbeau, and Nejib Zemzemi. "Towards the numerical simulation of electrocardio-

grams." In *Functional Imaging and Modeling of the Heart*, pp. 240–249. Springer, 2007.

[BGL11] R. Bordas, K. Gillow, Q. Lou, IR Efimov, D. Gavaghan, P. Kohl, V. Grau, and B. Rodriguez. "Rabbit-specific ventricular model of cardiac electrophysiological function including specialized conduction system." *Progress in Biophysics and Molecular Biology*, 2011.

[BL07] Mark W Barnett and Philip M Larkman. "The action potential." *Practical neurology*, **7**(3):192–197, 2007.

[BMS08] G. Buckberg, A. Mahajan, S. Saleh, J.I.E. Hoffman, and C. Coghlan. "Structure and function relationships of the helical ventricular myocardial band." *The Journal of Thoracic and Cardiovascular Surgery*, **136**(3):578–589, 2008.

[CHP07] JS Chen, W. Hu, MA Puso, Y. Wu, and X. Zhang. "Strain smoothing for stabilization and regularization of Galerkin meshfree methods." *Meshfree methods for partial differential equations III*, pp. 57–75, 2007.

[CJ89] KS Channer and JV Jones. "The contribution of atrial systole to mitral diastolic blood flow increases during exercise in humans." *The Journal of Physiology*, **411**(1):53–61, 1989.

[COH12] Leroy L Cooper, Katja E Odening, Min-Sig Hwang, Leonard Chaves, Lorraine Schofield, Chantel A Taylor, Anthony S Gemignani, Gary F Mitchell, John R Forder, Bum-Rak Choi, et al. "Electromechanical and structural alterations in the aging rabbit heart and aorta." *American Journal of Physiology-Heart and Circulatory Physiology*, **302**(8):H1625–H1635, 2012.

[CPW96] J.S. Chen, C. Pan, C.T. Wu, and W.K. Liu. "Reproducing kernel particle methods for large deformation analysis of non-linear structures." *Computer Methods in Applied Mechanics and Engineering*, **139**(1):195–227, 1996.

[DPD04] A. Dekker, B. Phelps, B. Dijkman, T. van Der Nagel, FH Van Der Veen, GG Geskes, and JG Maessen. "Epicardial left ventricular lead placement for cardiac resynchronization therapy: optimal pace site selection with pressure-volume loops." *The Journal of thoracic and cardiovascular surgery*, **127**(6):1641–1647, 2004.

[DY83] LINDA L Demer and FC Yin. "Passive biaxial mechanical properties of isolated canine myocardium." *The Journal of physiology*, **339**(1):615–630, 1983.

[ELM91] Debra S Echt, Philip R Liebson, L Brent Mitchell, Robert W Peters, Dulce Obias-Manno, Allan H Barker, Daniel Arensberg, Andrea Baker, Lawrence Friedman, H Leon Greene, et al. "Mortality and morbidity in patients receiving encainide, flecainide, or placebo: the Cardiac Arrhythmia Suppression Trial." *New England Journal of Medicine*, **324**(12):781–788, 1991.

[ENP11] A. Evangelista, P. Nardinocchi, PE Puddu, L. Teresi, C. Torromeo, and V. Varano. "Torsion of the human left ventricle: Experimental analysis and computational modeling." *Progress in Biophysics and Molecular Biology*, 2011.

[FG91] D Fedida and WR Giles. "Regional variations in action potentials and transient outward current in myocytes isolated from rabbit left ventricle." *The Journal of physiology*, **442**(1):191–209, 1991.

[GAS07] Tao Guo, Xun Ai, Thomas R Shannon, Steven M Pogwizd, and Donald M Bers. "Intra–Sarcoplasmic Reticulum Free [Ca2+] and Buffering in Arrhythmogenic Failing Rabbit Heart." *Circulation research*, **101**(8):802–810, 2007.

[GCA10] H. Geyer, G. Caracciolo, H. Abe, S. Wilansky, S. Carerj, F. Gentile, H.J. Nesser, B. Khandheria, J. Narula, and P.P. Sengupta. "Assessment of myocardial mechanics using speckle tracking echocardiography: fundamentals and clinical applications." *Journal of the American Society of Echocardiography*, **23**(4):351–369, 2010.

[GG09] A. Grosberg and M. Gharib. "Computational models of heart pumping efficiencies based on contraction waves in spiral elastic bands." *Journal of theoretical biology*, **257**(3):359–370, 2009.

[Gil03] Robert F Gilmour. "A novel approach to identifying antiarrhythmic drug targets." *Drug discovery today*, **8**(4):162–167, 2003.

[GK09] S. Goktepe and E. Kuhl. "Computational modeling of cardiac electrophysiology: A novel finite element approach." *IJNME*, **79**:156–178, 2009.

[GK10] S. Göktepe and E. Kuhl. "Electromechanics of the heart: a unified approach to the strongly coupled excitation–contraction problem." *Computational Mechanics*, **45**(2):227–243, 2010.

[GWK10] S. Göktepe, J. Wong, and E. Kuhl. "Atrial and ventricular fibrillation: computational simulation of spiral waves in cardiac tissue." *Archive of Applied Mechanics*, **80**(5):569–580, 2010.

[GWK12] Jin Kyu Gahm, Nicholas Wisniewski, Gordon Kindlmann, Geoffrey L Kung, William S Klug, Alan Garfinkel, and Daniel B Ennis. "Linear invariant tensor interpolation applied to cardiac diffusion tensor MRI." In *Medical Image Computing and Computer-Assisted Intervention–MICCAI 2012*, pp. 494–501. Springer, 2012.

[HBH05] Michael A. Heroux, Roscoe A. Bartlett, Vicki E. Howle, Robert J. Hoekstra, Jonathan J. Hu, Tamara G. Kolda, Richard B. Lehoucq, Kevin R. Long, Roger P. Pawlowski, Eric T. Phipps, Andrew G. Salinger, Heidi K. Thornquist, Ray S. Tuminaro, James M. Willenbring, Alan Williams, and Kendall S. Stanley. "An overview of the Trilinos project." *ACM Trans. Math. Softw.*, **31**(3):397–423, 2005.

[HCE05] T. Helle-Valle, J. Crosby, T. Edvardsen, E. Lyseggen, B.H. Amundsen, H.J. Smith, B.D. Rosen, J.A.C. Lima, H. Torp, H. Ihlen, et al. "New noninvasive method for assessment of left ventricular rotation speckle tracking echocardiography." *Circulation*, **112**(20):3149–3156, 2005.

[Hil38] AV Hill. "The heat of shortening and the dynamic constants of muscle." *Proceedings of the Royal Society of London. Series B, Biological Sciences*, **126**(843):136–195, 1938.

[HK12] Daniel E Hurtado and Ellen Kuhl. "Computational modelling of electrocardiograms: repolarisation and T-wave polarity in the human heart." *Computer methods in biomechanics and biomedical engineering*, (ahead-of-print):1–11, 2012.

[HMT98] PJ Hunter, AD McCulloch, and H. Ter Keurs. "Modelling the mechanical properties of cardiac muscle." *Progress in biophysics and molecular biology*, **69**(2-3):289–331, 1998.

[HO09] Gerhard A Holzapfel and Ray W Ogden. "Constitutive modelling of passive myocardium: a structurally based framework for material characterization." *Philosophical Transactions of the Royal Society A: Mathematical, Physical and Engineering Sciences*, **367**(1902):3445–3475, 2009.

[HRL09] Thomas Helle-Valle, Espen W Remme, Erik Lyseggen, Eirik Pettersen, Trond Vartdal, Anders Opdahl, Hans-Jørgen Smith, Nael F Osman, Halfdan Ihlen, Thor Edvardsen, et al. "Clinical assessment of left ventricular rotation and strain: a novel approach for quantification of function in infarcted myocardium and its border zones." *American Journal of Physiology-Heart and Circulatory Physiology*, **297**(1):H257–H267, 2009.

[IAY08] Takashi Ijiri, T Ashmhara, Takeshi Yamaguchi, Kenshi Takayama, Takeo Igarashi, Tatsuo Shimada, Tsunetoyo Namba, Ryo Haraguchi, and Kazuo Nakazawa. "A procedural method for modeling the purkinje fibers of the heart." *Journal of Physiological Sciences*, **58**(7):401, 2008.

[IW04] Salim F Idriss and Patrick D Wolf. "Transmural action potential repolarization heterogeneity develops postnatally in the rabbit." *Journal of cardiovascular electrophysiology*, **15**(7):795–801, 2004.

[KEN07] Gordon Kindlmann, Raul San Jose Estepar, Marc Niethammer, Steven Haker, and Carl-Fredrik Westin. "Geodesic-loxodromes for diffusion tensor interpolation and difference measurement." In *Medical Image Computing and Computer-Assisted Intervention–MICCAI 2007*, pp. 1–9. Springer, 2007.

[KHG97] P.J. Kilner, M.Y. Henein, and D.G. Gibson. "Our tortuous heart in dynamic modean echocardiographic study of mitral flow and movement in exercising subjects." *Heart and vessels*, **12**(3):103–110, 1997.

[KKS09] J.P. Keener, J. Keener, and J. Sneyd. *Mathematical physiology: Cellular physiology*. Springer Verlag, 2nd edition, 2009.

[KNI11] Geoffrey L Kung, Tom C Nguyen, Aki Itoh, Stefan Skare, Neil B Ingels, D Craig Miller, and Daniel B Ennis. "The presence of two local myocardial sheet populations confirmed by diffusion tensor MRI and histological validation." *Journal of Magnetic Resonance Imaging*, **34**(5):1080–1091, 2011.

[KZR09] Odening K.E, Z.O., Choi B. R, Cooper L.L, Chaves L, Schofield L, and Koren G. "Aging Slows Conduction in Rabbit His-Purkinje-System and Ventricles and Increases Arrhythmogeneity." In *30th Annual Scientific Sessions of the Heart Rhythm Society*, 2009.

[Lab82] MJ Lab. "Contraction-excitation feedback in myocardium. Physiological basis and clinical relevance." *Circ Res*, **50**:757–766, 1982.

[LGT03] Glenn Terje Lines, Per Grottum, and Aslak Tveito. "Modeling the electrical activity of the heart: a bidomain model of the ventricles embedded in a torso." *Computing and Visualization in Science*, **5**(4):195–213, 2003.

[LR94] CH. Luo and Y Rudy. "A dynamic model of the cardiac ventricular action potential. I. Simulations of ionic currents and concentration changes." *Circ. Res.*, **74**:1071–1096, 1994.

[MG80] Andrew Ronald Mitchell and David Francis Griffiths. "The finite difference method in partial differential equations(Book)." *Chichester, Sussex, England and New York, Wiley-Interscience, 1980. 281 p*, 1980.

[MGL07] Rajkumar Mantravadi, Bethann Gabris, Tong Liu, Bum-Rak Choi, William C de Groat, G André Ng, and Guy Salama. "Autonomic nerve stimulation reverses ventricular repolarization sequence in rabbit hearts." *Circulation research*, **100**(7):e72–e80, 2007.

[MSS08] A. Mahajan, Y. Shiferaw, D. Sato, A. Baher, R. Olcese, L.H. Xie, M.J. Yang, P.S. Chen, J.G. Restrepo, A. Karma, et al. "A rabbit ventricular action potential model replicating cardiac dynamics at rapid heart rates." *Biophysical journal*, **94**(2):392–410, 2008.

[NG09] A. Nasiraei-Moghaddam and M. Gharib. "Evidence for the existence of a functional helical myocardial band." *American Journal of Physiology-Heart and Circulatory Physiology*, **296**(1):H127–H131, 2009.

[NH00] MP Nash and PJ Hunter. "Computational mechanics of the heart." *Journal of elasticity*, **61**(1):113–141, 2000.

[NKB11] S.A. Niederer, E. Kerfoot, A.P. Benson, M.O. Bernabeu, O. Bernus, C. Bradley, E.M. Cherry, R. Clayton, F.H. Fenton, A. Garny, et al. "Verification of cardiac tissue electrophysiology simulators using an N-version benchmark." *Philosophical Transactions of the Royal Society A: Mathematical, Physical and Engineering Sciences*, **369**(1954):4331–4351, 2011.

[NT07] P. Nardinocchi and L. Teresi. "On the active response of soft living tissues." *Journal of Elasticity*, **88**(1):27–39, 2007.

[OKB10] Katja E Odening, Malcolm Kirk, Michael Brunner, Ohad Ziv, Peem Lorvidhaya, Gong Xin Liu, Lorraine Schofield, Leonard Chaves, Xuwen Peng, Manfred Zehender, et al. "Electrophysiological studies of transgenic long QT type 1 and type 2 rabbits reveal genotype-specific differences in ventricular refractoriness and His conduction." *American Journal of Physiology-Heart and Circulatory Physiology*, **299**(3):H643–H655, 2010.

[PBB10] P. Pathmanathan, M.O. Bernabeu, R. Bordas, J. Cooper, A. Garny, J.M. Pitt-Francis, J.P. Whiteley, and D.J. Gavaghan. "A numerical guide to the solution of the bidomain equations of cardiac electrophysiology." *Progress in biophysics and molecular biology*, **102**(2):136–155, 2010.

[PBN12] P. Pathmanathan, MO Bernabeu, SA Niederer, DJ Gavaghan, and D. Kay. "Computational modelling of cardiac electrophysiology: explanation of the variability of results from different numerical solvers." *International Journal for Numerical Methods in Biomedical Engineering*, 2012.

[PDV09] Mark Potse, Bruno Dubé, and Alain Vinet. "Cardiac anisotropy in boundary-element models for the electrocardiogram." *Medical & biological engineering & computing*, **47**(7):719–729, 2009.

[PH97] Alexander V Panfilov and Arun V Holden. *Computational biology of the heart*. John Wiley & Sons, 1997.

[PKA09] A.J. Prassl, F. Kickinger, H. Ahammer, V. Grau, J.E. Schneider, E. Hofer, E.J. Vigmond, N.A. Trayanova, and G. Plank. "Automatically generated, anatomically accurate meshes for cardiac electrophysiology problems." *Biomedical Engineering, IEEE Transactions on*, **56**(5):1318–1330, 2009.

[PMS11] P. Pathmanathan, G.R. Mirams, J. Southern, and J.P. Whiteley. "The significant effect of the choice of ionic current integration method in cardiac electro-physiological simulations." *International Journal for Numerical Methods in Biomedical Engineering*, **27**(11), 2011.

[PSL95] Pierre Pelce, Jiong Sun, and Cor Langeveld. "A simple model for excitation-contraction coupling in the heart." *Chaos Solitons and Fractals*, **5**:383–391, 1995.

[QG99] Z Qu and A. Garfinkel. "An advanced algorithm for solving partial differential equation in cardiac conduction." *IEEE Trans Biomed Eng.*, **46**:1166–1168, 1999.

[RZ05] Michael Rubart, Douglas P Zipes, et al. "Mechanisms of sudden cardiac death." *Journal of Clinical Investigation*, **115**(9):2305–2315, 2005.

[Sal69] E.A. Sallin. "Fiber orientation and ejection fraction in the human left ventricle." *Biophysical journal*, **9**(7):954–964, 1969.

[SCC12] Maxime Sermesant, Radomir Chabiniok, Phani Chinchapatnam, Tommaso Mansi, Florence Billet, Philippe Moireau, Jean-Marc Peyrat, K Wong, Jatin Relan, Kawal Rhode, et al. "Patient-specific electromechanical models of the heart for the prediction of pacing acute effects in CRT: a preliminary clinical validation." *Medical image analysis*, **16**(1):201–215, 2012.

[SFW08] S.M. Shaw, D.J. Fox, and S.G. Williams. "The development of left ventricular torsion and its clinical relevance." *International journal of cardiology*, **130**(3):319–325, 2008.

[SHW98] David F Scollan, Alex Holmes, Raimond Winslow, and John Forder. "Histological validation of myocardial microstructure obtained from diffusion tensor magnetic resonance imaging." *American Journal of Physiology-Heart and Circulatory Physiology*, **275**(6):H2308–H2318, 1998.

[SLC06] J. Sundnes, GT. Lines, X. Cai, BF. Nielsen, KA. Mardal, and A. Tveito. *Computing the Electrical Activity in the Heart*. Springer-Verlag, 2006.

[SLT01] J. Sundnes, GT. Lines, and A. Tveito. "Efficient solution of ordinary differential equations modeling electrical activity in cardiac cells." *Mathematical Biosciences*, **172**:55–72, 2001.

[SML] W Schroeder, K Martin, and B Lorensen. "The Visualization Toolkit An Object-Oriented Approach To 3D Graphics 3rd Edition, 2004, Kitware Inc." Technical report, ISBN-1-930934-12-2.

[SPB03] Thomas R Shannon, Steven M Pogwizd, and Donald M Bers. "Elevated sarcoplasmic reticulum Ca2+ leak in intact ventricular myocytes from rabbits in heart failure." *Circulation research*, **93**(7):592–594, 2003.

[SPC08] Maxime Sermesant, Jean-Marc Peyrat, Phani Chinchapatnam, Florence Billet, Tommaso Mansi, Kawal Rhode, Hervé Delingette, Reza Razavi, and Nicholas Ayache. "Toward patient-specific myocardial models of the heart." *Heart Failure Clinics*, **4**(3):289–301, 2008.

[SVU55] BORYS SURAWICZ, ROBERT G VAN HORNE, JOHN R URBACH, and SAMUEL BELLET. "QS-and QR-pattern in leads V3 and V4 in absence of myocardial infarction: electrocardiographic and vectorcardiographic study." *Circulation*, **12**(3):391–405, 1955.

[SWB05] Thomas R Shannon, Fei Wang, and Donald M Bers. "Regulation of cardiac sarcoplasmic reticulum Ca release by luminal [Ca] and altered gating assessed with a mathematical model." *Biophysical journal*, **89**(6):4096–4110, 2005.

[SWO12] J. Sundnes, S. Wall, H. Osnes, T. Thorvaldsen, and AD McCulloch. "Improved discretisation and linearisation of active tension in strongly coupled cardiac electro-mechanics simulations." *Computer Methods in Biomechanics and Biomedical Engineering*, 2012.

[TCG11] Natalia A Trayanova, Jason Constantino, and Viatcheslav Gurev. "Electromechanical models of the ventricles." *American Journal of Physiology-Heart and Circulatory Physiology*, **301**(2):H279–H286, 2011.

[TK04] J.A. Trangenstein and C. Kim. "Operator splitting and adaptive mesh refinement for the Luo–Rudy I model." *Journal of Computational Physics*, **196**(2):645–679, 2004.

[TMK11] Dennnis R Trumble, Walter E McGregor, RC Kerckhoffs, Lewis K Waldman, et al. "Cardiac assist with a twist: apical torsion as a means to improve failing heart function." *Journal of biomechanical engineering*, **133**(10):101003, 2011.

[TP06] K.H.W.J. ten Tusscher and A.V. Panfilov. "Alternans and spiral breakup in a human ventricular tissue model." *American Journal of Physiology-Heart and Circulatory Physiology*, **291**(3):H1088–H1100, 2006.

[TP08] KHWJ Ten Tusscher and AV Panfilov. "Modelling of the ventricular conduction system." *Progress in biophysics and molecular biology*, **96**(1):152–170, 2008.

[TZG96] Gabriel Taubin, Tong Zhang, and Gene Golub. *Optimal surface smoothing as filter design*. Springer, 1996.

[ULM02] T.P. Usyk, I.J. LeGrice, and A.D. McCulloch. "Computational model of three-dimensional cardiac electromechanics." *Computing and visualization in science*, **4**(4):249–257, 2002.

[UMM00] TP Usyk, R Mazhari, and AD McCulloch. "Effect of laminar orthotropic myofiber architecture on regional stress and strain in the canine left ventricle." *Journal of elasticity and the physical science of solids*, **61**(1-3):143–164, 2000.

[VAP10] Fijoy Vadakkumpadan, Hermenegild Arevalo, Anton J Prassl, Junjie Chen, Ferdinand Kickinger, Peter Kohl, Gernot Plank, and Natalia Trayanova. "Image-based models of cardiac structure in health and disease." *Wiley Interdisciplinary Reviews: Systems Biology and Medicine*, **2**(4):489–506, 2010.

[VAT02] E.J. Vigmond, F. Aguel, and N.A. Trayanova. "Computational techniques for solving the bidomain equations in three dimensions." *Biomedical Engineering, IEEE Transactions on*, **49**(11):1260–1269, 2002.

[VAT12] F Vadakkumpadan, H Arevalo, NA Trayanova, et al. "Patient-specific modeling of the heart: estimation of ventricular fiber orientations." *Journal of visualized experiments: JoVE*, (71), 2012.

[VRT09] F. Vadakkumpadan, L.J. Rantner, B. Tice, P. Boyle, A.J. Prassl, E. Vigmond, Plank G., and N. Trayanova. "Image-based models of

cardiac structure with applications in arrhythmia and defibrillation studies." *Journal of Electrocardiology*, **42**:157.e1–157.e10, 2009.

[Whi06] Jonathan P. Whiteley. "An Efficient Numerical Technique for the Solution of the Monodomian and Bidomain Equations." *IEEE Transactions on Biomedical Engineering*, **53**(11):2139–2147, 2006.

[Whi07] JP. Whiteley. "Physiology Driven Adaptivity for the Numerical Solution of the Bidomain Equations." *Annals of Biomedical Engineering*, **35**:1510–1520, 2007.

[WKD89] P Wach, R Killmann, F Dienstl, and Ch Eichtinger. "A computer model of human ventricular myocardium for simulation of ECG, MCG, and activation sequence including reentry rhythms." *Basic research in cardiology*, **84**(4):404–413, 1989.

[WMG96] Jeffrey A Weiss, Bradley N Maker, and Sanjay Govindjee. "Finite element implementation of incompressible, transversely isotropic hyperelasticity." *Computer methods in applied mechanics and engineering*, **135**(1):107–128, 1996.

[XQY04] F. Xie, Z. Qu, J. Yang, A. Baher, J.N. Weiss, A. Garfinkel, et al. "A simulation study of the effects of cardiac anatomy in ventricular fibrillation." *Journal of Clinical Investigation*, **113**(5):686–693, 2004.

[YDZ05] Anil V Yadav, Mithilesh K Das, and Douglas P Zipes. "Selection of patients for ICDs:where are we in 2005?." *ACC Current Journal Review*, **14**(6):33–37, 2005.

[ZCG01] Zhi-Jie Zheng, Janet B Croft, Wayne H Giles, and George A Mensah. "Sudden cardiac death in the United States, 1989 to 1998." *Circulation*, **104**(18):2158–2163, 2001.

[ZK79] Michael J Zema and Paul Kligfield. "Electrocardiographic poor R wave progression I: Correlation with the Frank vectorcardiogram." *Journal of Electrocardiology*, **12**(1):3–10, 1979.

[ZK82] Michael J Zema and Paul Kligfield. "ECG poor R-wave progression: review and synthesis." *Archives of internal medicine*, **142**(6):1145, 1982.

[ZSB09] V. Zimmerman, R. Sebastian, BH Bijnens, and AF Frangi. "Modeling the purkinje conduction system with a non deterministic rule based iterative method." In *Computers in Cardiology, 2009*, pp. 461–464. IEEE, 2009.

[ZW98] Douglas P Zipes and Hein JJ Wellens. "Sudden cardiac death." *Circulation*, **98**(21):2334–2351, 1998.